# Optical Manipulation and Sensing with Silicon Photonics

HARVARD UNIVERSITY
Graduate School of Arts and Sciences

DISSERTATION ACCEPTANCE CERTIFICATE

The undersigned, appointed by the

School of Engineering and Applied Sciences

have examined a dissertation entitled

"Optical manipulation and sensing with silicon photonics"

presented by Shiyun Lin

candidate for the degree of Doctor of Philosophy and hereby certify that it is worthy of acceptance.

*Signature* _____

*Typed name*: Prof. F. Capasso

*Signature* _____

*Typed name*: Prof. E. Hu

*Signature* _____

*Typed name*: Prof. V. Manoharan

*Signature* _____

*Typed name*: Prof. K. Crozier

*Date November 20, 2012*

# Optical manipulation and sensing with silicon photonics

A dissertation

by

Shiyun Lin

to

The School of Engineering and Applied Sciences

in partial fulfillment of the requirement

for the degree of

Doctor of Philosophy

in the subject of

Engineering Sciences

Harvard University

Cambridge, Massachusetts

January, 2013

Thesis Advisor

**Professor Kenneth B. Crozier**

Author

**Shiyun Lin**

# Optical Manipulation and Sensing with Silicon Photonics

## Abstract

Optical trapping enables the non-contact manipulation of micro and nanoparticles with extremely high precision. Recent research on integrated optical trapping using the evanescent fields of photonic devices has opened up new opportunities for the manipulation of nano- and microparticles in lab-on-a-chip devices. Considerable interest has emerged for the use of optical microcavities as "sensors-on-a-chip", due to the possibility for the label-free detection of nanoparticles and molecules with high sensitivity. This dissertation focuses on the demonstration of an on-chip optical manipulation system with multiple functionalities, including trapping, buffering, sorting, and sensing. We demonstrate the optically trapping of polystyrene particles with diameters from 110 nm to 5.6 μm using silicon microrings and photonic crystal cavities. By integrating multiple microrings with different resonant wavelengths, we show that tuning the laser wavelength to the resonance wavelengths of different rings enables trapped particles to be transferred back and forth between the rings in a controllable manner. We term this functionality "buffering". We furthermore demonstrate an integrated microparticle passive sorting system based on the near-field optical forces exerted by a 3-dB optical power splitter that consists of a

slot waveguide and a conventional channel waveguide. In related work, we demonstrate an ultra-compact polarization splitter design leveraging the giant birefringence of silicon-on-insulator slot waveguides to achieve a high extinction ratio over the entire C band.

We demonstrate trapping-assisted particle sensing, using the shift in the microcavity resonance induced by the trapped particle. We show that this permits the sensing of proteins *via* a binding assay approach, in which the presence of green fluorescent protein causes the particles to bind. By detecting the size distribution of particles clusters using the microcavity, we quantitatively detect the GFP concentration. In a complementary approach, we demonstrate a reusable and reconfigurable surface-enhanced Raman scattering (SERS) sensing platform. We use a photonic crystal cavity to trap silver nanoparticles in a controllable manner, and measure SERS from molecules on their surfaces. We anticipate that the on-chip sensing approaches we introduce could lead to various applications in nanotechnology and the environmental and life sciences.

# Table of content

# List of Publications

## Journal papers

- S. Lin, W. Zhu, Y. Jin and K. B. Crozier, "Surface enhanced Raman scattering with Ag nanoparticles optically trapped by a photonic crystal cavity," Submitted.
- S. Lin and K. B. Crozier, "Trapping-assisted sensing of particles and proteins using on-chip optical microcavities," Submitted.
- S. Lin and K. B. Crozier, "An integrated microparticle sorting system based on near-field optical forces and a structural perturbation," Optics Express **20**, 3367 (2012).
- S. Lin, and K. B. Crozier, "Planar silicon microrings as wavelength-multiplexed optical traps for storing and sensing particles," Lab on a chip **11**, 4047-51 (2011).
- S. Lin, J. Hu, and K. Crozier, "Ultracompact, broadband slot waveguide polarization splitter," Applied Physics Letters **98**, 151101 (2011).
- S. Lin, E. Schonbrun, and K. Crozier, "Optical Manipulation with Planar Silicon Microring Resonators," Nano letters **10**, 2408-2411 (2010).
- J. Hu, S. Lin, L. C. Kimerling, and K. Crozier, "Optical trapping of dielectric nanoparticles in resonant cavities," Physical Review A **82**, 053819 (2010).
- S. Lin, J. Hu, L. C. Kimerling, and K. Crozier, "Design of nanoslotted photonic crystal waveguide cavities for single nanoparticle trapping and detection," Optics Letters **34**, 3451–3453 (2009)

## Conference presentations

- K. Crozier and S. Lin “Photonic Nanostructures for Sensing and Other Applications,” Frontier in Optics 2012, Rochester, NY (2012).
- S. Lin and K. Crozier “Microparticle Trapping and Sensing with an Integrated Silicon Microdonut,” CLEO: Applications and Technology, San Jose, CA (2012).
- S. Lin, and K. Crozier, “Microparticle sorting using a slot waveguide splitter,” SPIE Photonics West 2011, San Francisco, CA (2011).
- S. Lin, and K. Crozier, "Optical Trapping Using Planar Silicon Micro-ring Resonators," Frontier in Optics 2010, San Jose, CA (2010).
- J. Hu, S. Lin, L. Kimerling, and K. Crozier, "Optical trapping of nanoparticles in resonant cavities: optical tweezers with single particle selectivity," Frontier in Optics 2010, San Jose, CA (2010).
- S. Lin, and K. B. Crozier, "Optical Trapping with Real-Time Feedback Using Planar Silicon Micro-Ring Resonators," Conference on Laser and Electro-Optics/Quantum Electronics and Laser Science Conference 2010, San Jose, CA (2010).
- S. Lin, J. Hu, L. Kimerling, and K. Crozier, "Design of Nanoslotted Photonic Crystal Waveguide Cavities for Single Nanoparticle Trapping," Conference on Laser and Electro-Optics/International Quantum Electronics Conference (CLEO/IQEC) 2009, Baltimore, MD (2009).

# List of contributions of thesis

1. We experimentally demonstrate optical tapping using microring resonators. Once trapped on a microring, a particle can be confined in an optical potential with a depth of 25 $k_BT$ over the entire microring's circumference.
2. We demonstrate the ability to store particles on a particular location on a chip, and then transport them to another position as desired using optical forces. We term this functionality "buffering". By changing the wavelength of the laser input to the chip, particles can be switched from one microring to the other, traveling between them on the waveguide.
3. We design and numerically simulate a novel optical trapping device that combines a photonic crystal waveguide cavity with a nanoslot structure. We also experimentally demonstrate the trapping of polystyrene particle with diameters from 110 nm to 2 μm, and silver nanoparticles with diameters of 80 nm.
4. We demonstrate a novel approach to particle sorting that makes use of a 3-dB optical splitter whose outputs comprise a channel waveguide and a slot waveguide. We experimentally prove that this device enables the sorting of particles with diameters of 2 μm and 320 nm using a laser power that is 1-2 orders of magnitude smaller than used in previous optical force-based particle sorting methods.
5. We demonstrate trapping and sensing of nanoparticles with diameters from 110 nm to 2 μm using photonic crystal cavities. Our device is reusable and capable of monitoring the trapping of particles in situ using a probe laser that measures the shift in cavity resonance wavelength.

6. We demonstrate a trapping-assisted sensing technique that enables the detection of proteins using a binding assay. We detect protein concentrations down to 10 nm using a platform that is reusable and reproducible.
7. We demonstrate a controllable and reusable SERS platform in which Ag nanoparticles are optically trapped by an on-chip photonic crystal cavity. In this way, we demonstrate a controllable SERS hotspot that can be continually replenished.
8. We demonstrate an ultracompact polarization splitter design leveraging the giant birefringence of silicon-on-insulator slot waveguide and achieve a high extinction ratio over the entire C-band.

# List of Movies

**Movie 2-1** Particle trapping using a microring with a radius of 5 μm. Three particles are delivered along the bus waveguide to a 5 μm microring, where they are then trapped at a power of 9 mW. The particles have a diameter of 1.1 μm. All the movies in this thesis are recorded and played at 60 frames per second (fps).

**Movie 2-2** Particle trapping using a microring with a radius of 10 μm. Two particles are trapped on the 10 μm ring and circulate around it. The particles have a diameter of 1.1 μm. The guided power for the trapping is estimated to be 4.5 mW.

**Movie 2-3** Trapping of particles diameters of 5.6 μm. A particle with diameter of 5.6 μm is trapped on a microring resonator with radius of 5 μm. The guided power in the waveguide is estimated to be 9 mW.

**Movie 3-1** Switching trapped particles between the bus waveguide and the microring resonator. Particles with diameter of 1.1 μm are trapped on a microring with radius of 10 μm, and the trapping power is 4.5 mW. After manually tuning the incident wavelength to be off-resonance, the trapped particles are switched from the microring cavity back to the bus waveguide.

**Movie 3-2** One-way particle buffer chain. A particle with diameter of 1.1 μm is delivered from the smaller to the larger ring by tuning the incident wavelength from 1557.9 nm to 1561.2 nm, which correspond to the resonance wavelengths of the 5 μm and 10 μm microrings, respectively. The guided trapping power is 5 mW.

**Movie 3-3** Two-way particle buffer chain. A particle with a radius of 1.1 μm is switched back

and forth between the two microrings by tuning the laser wavelength between 1554.5 nm and 1554 nm, which correspond to the resonances of the bottom and top microrings, respectively. The guided trapping power is 5 mW.

**Movie 4-1** Trapping of a polystyrene particle with diameter of 320 nm using a 1D photonic crystal cavity. Both a TE mode (2.5 mW) and a TM mode (2.5 mW) are launched to the waveguide to trap the particle on the waveguide and deliver it to the 1D photonic crystal cavity. The particle is pulled from the waveguide to the cavity due to the high field intensity of TE mode in the cavity. The particle is switched back to the waveguide by manual adjustment of the light input to the chip at $t$ = 6 s to make it completely TM mode.

**Movie 5-1** Particle sorting by a 3 dB TM mode splitter. Polystyrene particles with diameters of 320 nm and 2 μm are sent to microfluidic channel. The bright spots are fluorescent emission from the larger particles, while the dimmer spots represent the smaller particles. The particles are first trapped by the waveguide and delivered to the sorting device composed of a channel waveguide and a slot waveguide, where a directional coupler is formed. The total guided power in the incident waveguide is 20 mW. All the larger particles are delivered along the channel waveguide, while the smaller particles are switched to the slot waveguide by the sorting device.

**Movie 6-1** Real-time monitoring of particle trapping using our homemade two-laser system. This shows the recording of a typical experiment, in which polystyrene particles with diameters of 2 μm are trapped and sensed, with the process monitored by measuring the cavity resonance wavelength shift *in situ*. The left side shows the movie obtained with the fluorescent microscope. The right side is the measurement interface, with the scan settings on the top and two data charts

on the bottom. The left chart shows the transmission spectrum, and is updated after each scan. The peak finding function of the Labview software upon which this platform is based is used to determine the resonance wavelength from each transmission spectrum, with the result plotted as a function of time as the right chart. Three jumps of the resonance wavelength can be seen. These correspond to the events in which the three particles, visible in the microscope image of the left panel, were trapped. The results shown in this movie verify that our system enables monitoring of particle trapping in real time.

**Movie 8-1** Ag nanoparticle trapping using a 1D photonic crystal cavity. An Ag nanoparticle is trapped on the waveguide and delivered to the 1D photonic crystal cavity. The input to the waveguide is chosen so that a combination of a TE mode (50% power) and a TM mode (50% power) is excited. The total guided power is 9 mW.

# Acknowledgements

I would firstly like to thank my advisor Prof. Kenneth Crozier for his guidance and support in my four and a half years of Ph.D. study. Ken has always been there to give insightful advice and point me in the right directions for my research. I have learned a lot from him about how to become a good researcher. In addition to the guidance, he also gives me the freedom to explore a variety of topics and always gives me full support. Thank you so much for all your help, guidance and support.

I would like to thank my research committee: Prof. Federico Capasso, Prof. Evelyn Hu, and Prof. Vinothan Manoharan. They are the true leaders and pioneers in their respective research fields. I feel so lucky to have opportunities to learn from them.

I would like to thank my labmates in the Nanophotonics Lab at Harvard. I want to express my special thanks to Mr. Wenqi Zhu for helping me build the Raman measurement setup. He has been the greatest roommate as well. I would like to thank Mr. Dongxing Wang, Dr. Kai Wang for insightful discussions. I also want to thank Dr. Yizhuo Chu for helping me with experiments and with job hunting, and Dr. Ethan Schonbrun for helping me finish my first paper at Harvard. I would also like to thank all the following individuals for their help: Mr. Yuhang Jin, Mr. Antony Orth, Dr. Tal Ellenbogen, Dr. Kwanyong Seo, Dr. Yaping Dan, Mr. Hyunsung Park, Mr. Peter Duane, Dr. Turgut Tut, Dr. Paul Steinvurzel, Dr. Mohamad Banaee, Dr. Eng Huat Khoo, Dr.

Winnie Ye, and Dr. Tian Yang.

I want to thank my collaborators at MIT. Professor Juejun Hu is the most wonderful and dedicated collaborator I have ever met. His passion and vision always give me courage. Prof. Lionel Kimerling is a leader in the field of silicon photonics. I feel so privileged to learn from him. Prof. Kazumi Wada was my advisor during my Masters program at the University of Tokyo. He guided me to the world of photonics. Learning from his passion, wisdom and vision helped me prepare well for studying at Harvard, and I'm sure it will help me in the future. He has been a good mentor to me in both my academic and personal life.

I also want to thank my family and friends for their support and companion on this journey. I am grateful to my parents, who have always respected my decisions and have always done whatever they could to help and support me. Finally, I would like to thank my wife, Yuan Cheng. Your companionship and support make the whole journey more enjoyable.

*Dedicated to*

*My wife and my parents*

# Chapter 1 Introduction

## 1.1 Overview

Integrated photonics, especially devices based on the silicon platform, has been a hot research field in both academia and industry, mainly owing to its great potential for optical communication applications[1], [2]. High performance silicon photonic devices have been demonstrated using silicon-on-insulator (SOI) substrates, including optical filters[3], modulators[4–6], photodetectors[7], [8], and lasers[9–11]. Optical resonators play critical roles in most of these devices. When the optical field is at the resonance frequency, it constructively interferes and builds up in the cavity. A high field enhancement is achieved in the resonator, *i.e.* the circulating field is much larger than the incident field. This is advantageous for applications such as nonlinear optics[12] and optical trapping[13]. Light circulating in the cavity interacts multiple times with objects inside or near the cavity before escaping from it. This enhanced light-matter interaction makes optical resonators perfect a candidate for sensing applications[14–18].

Since their introduction in 1986, optical tweezers have become an important tool in the biological sciences[19]. Recently, there has been considerable interest in realizing microfabricated optical tweezer devices for lab-on-a-chip applications. Kawata and coworkers demonstrated the optical trapping of dielectric and metallic particles on dielectric waveguides

[20]. Since then, a number of near field optical trapping techniques using plasmonic or photonic structures have been reported[21–26]. In this dissertation, we use the high field intensity in integrated optical microcavities to enhance the optical forces on micro- and nanoparticles. In addition to the trapping of small objects, various on-chip manipulation functionalities including trapping, delivery, sorting, and buffering are demonstrated.

In recent times, considerable interest has emerged for the use of optical microcavities as "sensors-on-a-chip", due to the possibility of label-free high sensitivity detection of nanoparticles and molecules[27], [28]. However, the sensing of molecules is almost exclusively performed *via* their binding to a functionalized device surface[29]. This means that the devices are seldom re-usable, that their functionalization needs to be decided before use, and that they face the diffusion bottleneck. To solve these problems, we introduce two different trapping-assisted sensing techniques; the first is based on refractometry, while the second is based on surface-enhanced Raman spectroscopy. In both cases, optical forces are used to load the particles onto the optical cavity. The trapped particles become self-aligned with the field maximum of the cavity, which improves reproducibility of the sensing process.

The structure of the dissertation is as follows: In Chapter 1, we review the background and fundamentals of microcavities, optical forces and optical sensing. In Chapters 2-5, we describe work carried out on optical trapping and manipulation. In Chapters 6-8, we describe our work on trapping-assisted sensing, including a particle trapping and sensing system, a protein sensing

assay, and a surface-enhanced Raman spectroscopy platform. In Chapter 9, we introduce our work on a compact polarization splitter for future optical communication chips. Chapter 10 summarizes the thesis and discusses future work.

## 1.2 Fundamentals of optical cavities

Optical cavities are optical resonators, and confine and store light at certain resonance wavelengths that satisfy the following condition:

$$\frac{\lambda_r}{n_{eff}} \cdot N = L \tag{1.1}$$

where $\lambda_r$ is called the resonance wavelength, $L$ is the path length for one round trip of light in the cavity, $n_{eff}$ is the effective index of the cavity, and $N$ is an integer corresponding to the resonance mode order. For simplicity, we assume that any phase changes associated with reflections from the end mirrors of the cavity are incorporated into the path length $L$.

The frequency spacing $\nu_{FSR}$ between adjacent resonator modes is called free spectral range (FSR), and can be calculated from Eq. (1.1) as:

$$\nu_{FSR} = \frac{c}{L \cdot n_{eff}} \tag{1.2}$$

Assuming that the complex amplitude of the optical wave that initially enters the microcavity is $U_0$, its complex amplitude after one round-trip can be expressed as

$$U_1 = r \cdot \exp(-j\varphi) \cdot U_0 \tag{1.3}$$

where $\varphi$ is the phase shift calculated by $\varphi = k \cdot L$, where $k$ is the wave vector, and $r$ is attenuation factor given by $r = \exp(-\alpha \cdot L/2)$, where $\alpha$ is the effective overall distributed loss coefficient. As mentioned above, it is assumed that phase shifts from cavity mirrors et.c. are included in $\varphi$. Similarly, the amplitude after two round trips is $U_2 = r \cdot \exp(-j\varphi) \cdot U_1 = (r \cdot \exp(-j\varphi))^2 \cdot U_0$. With an infinite number of waves taken into account, therefore, the amplitude in the cavity is therefore given as follows:

$$\begin{aligned} U &= U_0 + U_1 + U_2 + \cdots \\ &= U_0 + U_0 \cdot (r \cdot \exp(-j\varphi)) + U_0 \cdot (r \cdot \exp(-j\varphi))^2 + \cdots \\ &= U_0/(1 - r \cdot \exp(-j\varphi)) \end{aligned} \tag{1.4}$$

The intensity in the cavity is calculated by

$$\begin{aligned} I &= |U|^2 = |U_0|^2/|1 - r \cdot \exp(-j\varphi)|^2 \\ &= \frac{I_{max}}{1+\left(\frac{2F}{\pi}\right)^2 sin^2(\varphi/2)} \end{aligned} \tag{1.5}$$

where $I_{max} = \frac{|U_0|^2}{(1-r)^2} = \frac{I_0}{(1-r)^2}$, and

$$F = \frac{\pi \cdot \sqrt{r}}{1-r} = \frac{\pi \cdot \exp(-\alpha L/4)}{1-\exp(-\alpha L/2)} \tag{1.6}$$

is an important parameter known as the finesse of the cavity. If the loss is small, *i.e.* $\alpha L \ll 1$, then $\exp\left(-\frac{\alpha L}{4}\right) \approx 1$, and $\exp\left(-\frac{\alpha L}{2}\right) \approx 1 - \frac{\alpha L}{2}$. Therefore, we have

$$F = \frac{2\pi}{\alpha L} \tag{1.7}$$

The intensity is a periodic function of $\varphi$, with sharp peaks centered at the value of $\varphi = 2\pi N$. When the *F* is very large, the peaks have a full-width-at-half-maximum (FWHM) of $\Delta\varphi_{FWHM} = 2\pi/F$. Using Eq. (1.2), we have

$$\Delta\varphi_{FWHM} = \Delta k \cdot L = \frac{2\pi \cdot \Delta\nu_{FWHM} \cdot n_{eff} \cdot L}{c} = \frac{2\pi \cdot \Delta\nu_{FWHM}}{\nu_{FSR}} \tag{1.8}$$

In terms of frequency, therefore, the peaks have a full-width-at-half-maximum of

$$\Delta\nu_{FWHM} = \frac{\nu_{FSR}}{F} = \frac{\alpha c}{2\pi \cdot n_{eff}} \tag{1.9}$$

The quality factor ($Q$) is one of the most important parameters representing how long the light is confined in a cavity, and can be expressed as:

$$Q = 2\pi \cdot \frac{Energy\ stored\ in\ the\ cavity}{Energy\ dissipated\ per\ cycle} \tag{1.10}$$

The energy in the cavity is lost at a fractional rate of $c\alpha/n_{eff}$ per unit time, which corresponds to $\frac{c\alpha}{\nu \cdot n_{eff}}$ per cycle. Therefore, using Eq. (1.9) the $Q$ can be expressed as:

$$Q = 2\pi \cdot \frac{\nu \cdot n_{eff}}{c\alpha} = \frac{\nu}{\Delta\nu_{FWHM}} = \frac{\lambda}{\Delta\lambda_{FWHM}} \tag{1.11}$$

where $\Delta\lambda_{FWHM}$ is the full-width-at-half-maximum (FWHM) of the transmission spectrum in terms of wavelength. The photon lifetime, also termed the resonator lifetime, is given by:

$$\tau = \frac{n_{eff}}{c\alpha} \tag{1.12}$$

Therefore, the Q is proportional to the photon lifetime, according to:

$$Q = 2\pi \cdot \nu \cdot \tau \tag{1.13}$$

Here, the energy dissipation includes all forms by which energy may be lost from the cavity, including material loss, scattering, modal radiation, and output (*e.g.* transmission through a cavity mirror).

The mode volume is another important cavity parameter, and is given by:

$$\mathrm{V}_m = \frac{\int \varepsilon \cdot |E|^2 dv}{|\varepsilon \cdot E_{max}|^2} \tag{1.14}$$

where the $E$ denotes the electric field and $E_{max}$ is the maximum value of the field. The integration is done over the cavity and surrounding regions. The mode volume indicates how tightly light is confined to the cavity.

The value of the electric field enhancement can be found using energy conservation considerations. Here, we consider a cavity coupled to a bus waveguide. The incident power flux is $P_0$ and the transmission coefficient is $T$. The energy flux coupled into the cavity is $\mathrm{P}_0 \cdot (1 - T)$. According to energy conservation principles, the energy dissipation rate in the cavity should equal the power flux entering the cavity, *i.e.*

$$\mathrm{P} \cdot \alpha \cdot \mathrm{L} = \mathrm{P}_0 \cdot (1 - T) \tag{1.15}$$

where the $P$ denotes the power circulating in the cavity. The field intensity enhancement in the cavity can be therefore found as:

$$G = \frac{P}{P_0} = \frac{1}{\alpha \cdot L} \cdot (1 - T) = \frac{c \cdot A_{eff} \cdot (1-T)}{\omega \cdot n_{eff}} \cdot \frac{Q}{V_m} \tag{1.16}$$

where $\mathrm{A}_{eff} = \frac{V_m}{L}$ is the effective mode size. It remains constant when changing the cavity length for the Fabry-Perot cavities or microrings. A cavity with high $Q$ and small mode volume provides a large field enhancement and therefore is a promising candidate for optical trapping.

From Eq. (1.16), it can be seen that the transmission coefficient $T$ at the resonance frequency is critical for a high field enhancement. The transmission intensity is zero for the critical coupling case, which is achieved when the internal loss in the cavity is equal to the coupling loss to the bus waveguide. The relationship between the transmission coefficient, the coupling coefficient,

and the internal cavity loss can be found using the coupling matrix formalism[30]. To achieve critical coupling, it is common to optimize the coupling coefficient by controlling the gap between the waveguide and the cavity.

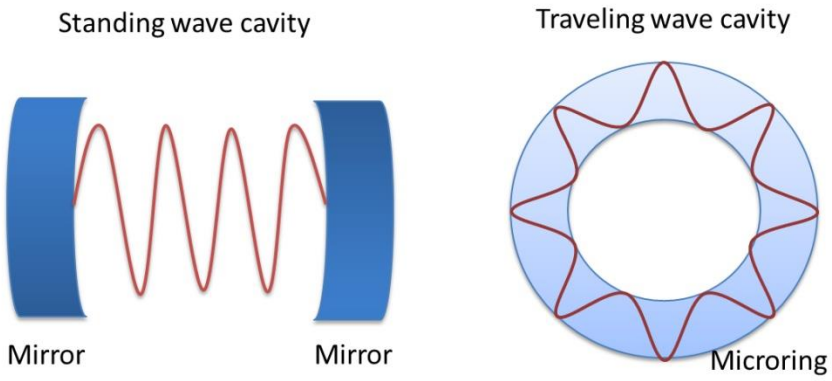


**Figure 1-1 Schematic diagrams of standing wave and traveling wave cavities**

As shown in Fig. 1-1, there are two main cavity classes. A standing wave cavity, such as the Fabry-Perot cavity shown on the left side of Fig. 1-1, has mirrors on both ends. Light is reflected back and forth between the mirrors. Photonic crystals cavities can be considered as standing wave cavities, with the end mirrors consisting of the periodic holes or pillars of the photonic crystal region. A traveling wave cavity, such as the microring shown on the right side of Fig. 1-1, has a non-zero wave vector in the propagation direction. High *Qs* have been achieved for both traveling wave and standing wave cavities based on silicon. However, the mode volumes for traveling wave cavities such as microrings are usually larger than those of standing wave cavities such as photonic crystal cavities. As traveling wave cavities are reduced in size, bending loss starts to become appreciable. This prevents them from simultaneously achieving high quality

factors and small mode volumes. On the other hand, standing wave resonators such as photonic crystal cavities can achieve extremely small mode volumes while maintaining high quality factors.

## 1.3 Introduction to optical forces

Optical trapping enables the non-contact manipulation of micro and nanoparticles with extremely high precision[31]. Traditionally, optical forces have been exerted on particles in solution using laser beams focused by high numerical aperture (NA) lenses[32–34]. In addition to localizing a particle to a single spot, high NA lenses can project other patterns such as lines[35], rings[36], [37], or periodic interference patterns[38], to exert optical forces on objects over larger areas. A major limitation of this technique however, is that when a laser beam is spread over a larger area, the optical force is reduced in proportion to the decreased intensity.

### *1.3.1 Fundamentals of optical force*

Optical forces originate from the momentum exchange between optical fields and objects. Optical forces due to radiation pressure have been known for more than a century[39]. In 1986, Ashkin *et al* showed that one could trap a tiny particle in three dimensions using a laser focused by an objective lens[19], a method now known as optical tweezers. Since then, optical tweezers have found a broad range of scientific applications, especially in the life sciences[40].

The dipole approximation is helpful in providing physical interpretation to the origin of optical forces. When an object is smaller than the wavelength, it can be approximated by a dipole, whose polarizability in an electrostatic field is given by:

$$\alpha_0 = 4\pi\varepsilon_e r^3 \cdot \frac{\varepsilon_p - \varepsilon_e}{\varepsilon_p + 2\varepsilon_e} \tag{1.17}$$

where $r$ is the radius of the particle, $\varepsilon_p$ is the dielectric constant of the particle, and $\varepsilon_e$ is the dielectric constant of the surrounding medium. Taking radiation damping into account, the polarizability becomes:

$$\alpha = \alpha' + \alpha'' i = 4\pi\varepsilon_e \cdot \frac{A}{1 - \frac{2}{3} i k^3 A} \tag{1.18}$$

$$\text{where } A = \frac{\alpha_0}{4\pi\varepsilon_e},\ k = \frac{2\pi}{\lambda} \tag{1.19}$$

The dipole moment induced under an external field is

$$\vec{P}(r,t) = Re\{\alpha \cdot \vec{E}(r) e^{-i\omega t}\} \tag{1.20}$$

The optical force exerted on the induced dipole can be found from the Lorentz force equation as:

$$\vec{F}(r,t) = (\vec{P}(r,t) \cdot \nabla)\vec{E}(r,t) + \frac{\partial \vec{P}(r,t)}{\partial t} \times \vec{B}(r,t) \tag{1.21}$$

Where $\vec{E}(r,t)$ and $\vec{B}(r,t)$ are the electric and magnetic field, respectively. In a time-harmonic field, the time averaged force is given by:

$$\langle \vec{F}(r,t) \rangle = \frac{1}{2} Re\left\{ \left(\vec{P}(r) \cdot \nabla\right)\vec{E}^*(r) + i\omega \cdot \vec{P}(r) \times \vec{B}^*(r) \right\} \tag{1.22}$$

Using the Maxwell equation (Faraday's law) and vector dot product identity:

$$\left(\vec{E}(r) \cdot \nabla\right)\vec{E}^*(r) = \begin{bmatrix} \vec{E}(r) \cdot \frac{\partial \vec{E}^*(r)}{\partial x} \\ \vec{E}(r) \cdot \frac{\partial \vec{E}^*(r)}{\partial y} \\ \vec{E}(r) \cdot \frac{\partial \vec{E}^*(r)}{\partial z} \end{bmatrix} + \vec{E}(r) \times \left(\nabla \times \vec{E}^*(r)\right) \tag{1.23}$$

the force can be further expressed as[41]

$$\langle \vec{F}(r,t) \rangle = \frac{\alpha'}{4} \nabla \left|\vec{E}(r)\right|^2 - \frac{\alpha''}{2} \mathrm{Im}\left\{ \begin{bmatrix} \vec{E}(r) \cdot \frac{\partial \vec{E}^*(r)}{\partial x} \\ \vec{E}(r) \cdot \frac{\partial \vec{E}^*(r)}{\partial y} \\ \vec{E}(r) \cdot \frac{\partial \vec{E}^*(r)}{\partial z} \end{bmatrix} \right\} \tag{1.24}$$

The first term is proportional to the field gradient, and therefore corresponds to the gradient force.

The second term is related to the energy flux of the field and is termed the scattering force. For a small dielectric particle with a polarizability given in Eq. (1.18), the gradient optical force is given by:

$$\vec{F}_{gradient} \approx \pi \varepsilon_e r^3 \cdot \frac{\varepsilon_p - \varepsilon_e}{\varepsilon_p + 2\varepsilon_e} \nabla \left|\vec{E}\right|^2 \tag{1.25}$$

Similarly, the scattering force exerted on the particle by a plane wave field with intensity of $I_0$ propagating in the direction of $\vec{s}$ is:

$$\vec{F}_{scattering} \approx \frac{128\,\pi^5 r^6}{3\lambda^4 c} \cdot \left(\frac{\varepsilon_p - \varepsilon_e}{\varepsilon_p + 2\varepsilon_e}\right)^2 I_0 \vec{s} \tag{1.26}$$

In order to trap an object in three dimensions, the gradient force in the light propagation direction needs to be large enough to compensate the scattering force, which is always points away from the light source. Therefore, a tightly focused laser beam is required. The gradient force is proportional to the cube of the particle radius. As particle size decreases, the gradient force decreases rapidly. This explains why the trapping of particles smaller than 100 nm is difficult for traditional optical tweezers. A large optical power is required for trapping small objects such as viruses.

While the dipole approximation provides useful physical insight, it is no longer accurate for particles with sizes comparable to, or larger than, the wavelength. Instead, the Maxwell stress tensor method can be used to calculate the optical force rigorously[42], [43]. From the Lorentz force equation and the Maxwell equations, the time averaged optical force density can be expressed as:

$$\bar{f}(\bar{r}) = \frac{1}{2} Re\{\nabla \cdot \bar{\bar{T}}(\bar{r})\} \tag{1.27}$$

The Maxwell stress tensor is

$$\bar{\bar{T}}(\bar{r}) = \frac{1}{2}(\bar{D} \cdot \bar{E}^* + \bar{B}^* \cdot \bar{H})\bar{I} - \bar{D}\bar{E}^* - \bar{B}^*\bar{H} \tag{1.28}$$

where $\bar{E}$, $\bar{D}$, $\bar{H}$, and $\bar{B}$ are the electric field, electric flux density, magnetic field, and magnetic flux density, respectively.

By integrating over a volume *V* enclosed by a surface *S* and applying the divergence theorem, the total force on the materials enclosed by *S* can be calculated by

$$\bar{F} = -\frac{1}{2} Re\{\oiint dS(\hat{n} \cdot \bar{\bar{T}}(\bar{r})\} \tag{1.29}$$

where $\hat{n}$ is the outward normal to the surface *S*.

The force calculation of an object is described as follows: First, the electromagnetic fields are found, for example numerically using the finite-difference time-domain (FDTD) method. The total force exerted on the object is then calculated by integrating the Maxwell stress tensor over a surface surrounding it. All the simulated optical forces in this dissertation are calculated in this way, unless specifically indicated otherwise.

### *1.3.2 Evanescent field optical trapping*

Total internal reflection results in evanescent fields that decay exponentially with distance from a surface. At visible wavelengths, a typical decay length is around 100 nm. For example, a plane wave (λ = 633 nm) incident on an air-glass interface at 60 degrees give a decay length of 121 nm. The evanescent fields have wave vectors that are purely imaginary in the direction perpendicular

to the surface. The dipole approximation, therefore, predicts that the scattering force perpendicular to the surface, which would push the object outward, is zero. The dipole approximation furthermore predicts that the rapidly decaying evanescent field exerts a large gradient force that pulls the object toward the surface.

Dielectric optical waveguides, *e.g.* silicon, are often used to deliver optical power on a chip. In the same manner as occurs in optical fibers, the optical field is mainly confined in the waveguide core, while the field outside the core is evanescent, and rapidly decays with distance from the core. Waveguide-based near field trapping has proven to be an alternative to free-space optical tweezers that trap particles with the focal spots generated by lenses. Kawata and coworkers demonstrated the optical trapping and propulsion of both metallic and dielectric particles at the surface of a glass optical waveguide[20]. A number of waveguide trapping experiments have been subsequently reported using different materials[21], [44–48]. In addition to the gradient force, light propagating along the waveguide exerts a scattering force on the object. This pushes the object along the light propagation direction just like its free space counterpart in traditional optical tweezers. Waveguide trapping therefore provides the means to deliver particles to different locations on a chip, for which various applications have been suggested[49].

As noted above, the optical force exerted on an object decreases rapidly with its size. This has in part motivated the use of cavities, such as photonic crystals[24], [50–53] and microspheres[16], since these can increase the optical force *via* the high field intensities that they produce. In

addition to the force enhancement, cavities could also provide new functionalities to the waveguide based optical trapping platform, like switching[54], sorting[37], [47] and sensing[29], [55]. Cavities, however, also bring challenges, as their narrow bandwidths make the system frequency sensitive. Slot waveguides present another means for force enhancement and nanoparticle trapping [56]. Compared to a waveguide trapping configuration, resonant cavity trapping offer two primary advantages: 1) the high field confinement in a cavity leads to strong optical force enhancement, 2) cavity perturbation induced by the trapped object could serve as a highly sensitive probe for analyzing its physical properties such size, refractive index, and absorption. Unlike free space optical trapping geometries, optical waves propagating through waveguide devices stay highly confined over larger distances, and consequently are capable of delivering larger optical forces over larger areas.

### 1.4 Cavity sensing

The sensing of molecules such as proteins is a basic operation in the life sciences. Traditional bulk molecule sensing approaches such as Western Blot [57] usually require relatively large samples and require the target molecules to be separated and purified, which increases complexity and cost. This has motivated the development of integrated lab-on-a-chip microanalysis systems, due to their low reagent consumption and small footprint. They present the opportunity for low cost and portable diagnosis systems[58], [59]. Optical biosensors have much potential for these types of systems, as they permit biological samples to be sensed in a non-invasive manner.

Microcavity-based sensors can possess ultrahigh sensitivity[14], [29], [60], [61]. Light is reflected back and forth, and builds up in the cavity when it is in phase and interferes constructively with itself. How long the light can be confined in the cavity before dissipating is proportional to the quality factor (*Q*) of the cavity. The light traveling in the cavity can interact with the objects in the vicinity of the cavity many times before dissipating. This enhances light-matter interaction and induces a larger sensing signal.

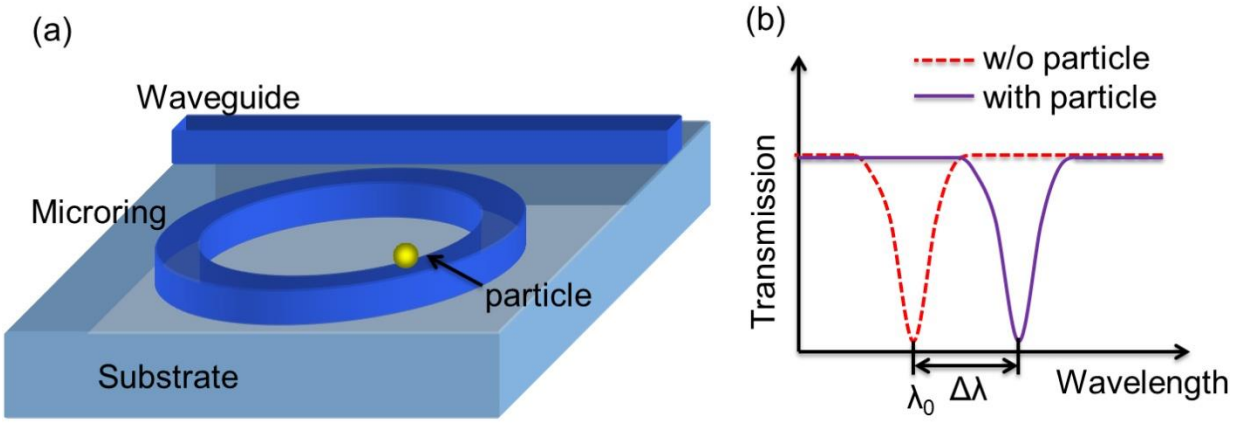


**Figure 1-2 (a) Schematic diagram of microring sensing, (b) transmission spectra of the cavity with a high Q can provide a high sensitivity due to its sharp resonance peak.**

The most common cavity sensing approach is based on refractive index. When an analyte (*e.g.* particle in Figure 1-2) comes close to the surface of the cavity, it introduces perturbation to the cavity mode due to its refractive index differing from that of the background medium (usually water). This can be thought of as altering the effective index of cladding and therefore the optical path length of the cavity. Figure 1-2 shows a schematic diagram of a particle being sensed by a microring cavity. The incident light is coupled into the microring from a bus waveguide. The

transmission spectrum is measured by scanning the wavelength of the incident laser, as shown in Figure 1-2(b). The resonance wavelength ($\lambda_0$) of the cavity can be determined from the transmission spectrum measured without the particle on the surface. As discussed above, when the particle comes into the vicinity of the microring surface, it introduces a perturbation to the resonance mode. For particles much smaller than the wavelength of the light, we can use dipole approximation to calculate the perturbation induced by the nanoparticle. The first order perturbation theory gives the fractional change of the resonance frequency as[62]

$$\frac{\Delta\omega}{\omega_0} \cong \frac{-\alpha_p \cdot |E_p|^2}{2\int \varepsilon_0 |E|^2 dV} \tag{1.30}$$

where $\alpha_p$ is the real part of the polarizability of the particle calculated by Eq. (1.18). The term $E_p$ is the electric field at the location of the particle. $\varepsilon_0$ is the dielectric constant of the surrounding medium. The magnitude of the resonance shift therefore provides information on the polarizability of the trapped particle, which is in turn related to its size and dielectric constant. From Eq. (1.30), it is clear that increasing the electric field at the position of the particle presents a means for enhancing the resonance shift.

By functionalizing the cavity surface, specificity on the molecules to be sensed can be obtained[15], [29]. Before the measurement, the surface of the cavity is coated with antibodies or receptors that interact with the target molecules in a specific manner. When the sample is introduced to the sensor, the target molecules gradually bind to the receptors on the surface of the cavity, and cause a resonance shift. Remarkable results have been recently obtained[29], [61], [63], [64], showing the highly sensitive detection of analytes *via* the resonance shifts that result

when they bind to the surfaces of optical microcavities. Several groups have reported high sensitivity biosensing using optical microcavities such as microrings, photonic crystal cavities, microspheres, and microtoroids[27], [61]. Ultrahigh Q cavities, such microspheres and microtroids, have been proven to enable provide extremely low detection limits.

### 1.5 On-chip particle micromanipulation and sensing

In this dissertation, we first describe the development of photonic chips that employ silicon waveguides, polarization splitters, microring resonators and photonic crystal resonators for the optical manipulation of micro- and nanoparticles. These provide the functionalities of trapping, delivery, buffering and sorting. We demonstrate that the large field enhancement provided by the microring and photonic crystal resonators enables the trapping of particles with the optical gradient force. The gradient force that arises from the evanescent fields also pulls particles onto the surfaces of the silicon waveguides, where they are then pushed in the propagation direction by the scattering force. We demonstrate that this enables their delivery to different locations on the chip. The microcavities also provide a great amount of control to the manipulation process, since they only trap particles when on resonance. We demonstrate that by tuning the wavelength of the laser coupled to the chip, the particles can be switched between the cavity and the bus waveguide. This allows the function we term “buffering”, where a particle can be trapped and stored on a microcavity resonator. We demonstrate that, by tuning the wavelength of the laser appropriately, particles can be transferred back and forth between the resonators. We also demonstrate the sorting of particles using a directional coupler-based power splitter. Particles are

pulled onto a channel waveguide by the gradient force, and then propelled along it by the scattering force and delivered to the splitter. The smaller particles exit the splitter along a slot waveguide, while the larger particles exit the splitter along a channel waveguide. We note that these functions can be readily integrated onto a single chip.

In the second part of the dissertation, we demonstrate three sensing modalities with our platform. These comprise the sensing of particles, the sensing of proteins *via* a binding assay, and the sensing of molecules *via* spectroscopy. We summarize our results in each of these in the paragraphs that follow.

The particles are sensed *via* the perturbation they provide to the microcavity due to the fact that their refractive index differs from the background medium (water). Particles have been previously sensed with microcavities using this perturbation, but we employ optical trapping as a means to controllably load and release the particles to be sensed. This has the advantage of breaking the diffusion limit that sometimes hampers sensing speed. Rather than waiting for particles to diffuse into the vicinity of the microcavity, the particles are actively drawn to it by optical forces. We furthermore use optical forces, rather than physical adsorption, to keep the particles in-place during the sensing process. This allows them to be released after they are sensed and new particles sensed, which would not be possible were physical adsorption used. The sensing reproducibility is also enhanced since the particles are self-aligned with the field maxima. We demonstrate the trapping and sensing of particles with a WGM microdonut cavity

and with a nanobeam photonic crystal cavity. In summary, the novelty of our particle-sensing technique is four-fold: (1) Optical trapping makes possible to load and release the analyte in a controllable manner, enabling a reusable and continuously-operating platform; (2) Optical forces help capture the analyte and break the mass transport limitation; (3) The optically trapped target analyte self-aligns with the field maximum, optimizing the light-matter interaction and increasing the stability of the sensing process; (4) That the device is waveguide-coupled and planar makes it possible to readily integrate multiple functionalities on a chip.

We demonstrate a new binding assay for protein sensing using our on-chip optical manipulation system. Instead of directly monitoring the resonance shift induced by molecules binding to a cavity, we measure the size distributions of clusters of antibody-coated particles bound by the molecules. We demonstrate that this enables protein concentration to be monitored in a quantitative fashion.

We demonstrate the sensing of molecules with surface enhanced Raman scattering (SERS). Broadly speaking, there are two competing approaches being pursued for the realization of structures for high performance SERS. The first method comprises forming gold or silver nanoparticles (or other nanostructures) on substrates, *e.g.* glass or silicon. The second method comprises gold or silver nanoparticles that are formed in solution *via* colloidal chemistry techniques. The former method has the advantage that very high performance SERS can be achieved, *e.g.* using high resolution lithography to produce nanoparticles in arrangements that

are favorable for field enhancement. Because of the control that lithography permits, the structures are also highly reproducible. The main disadvantage, however, is that of the high fabrication cost. The devices are furthermore one-time use only. The second method has the advantage that high quality particles can be produced in large quantities at low cost. For high performance, the salt-induced aggregation of particles is employed to generate clusters that produce high values of field enhancement. This has the disadvantages, however, that it is a process over which there is little control, and that the SERS performance can differ widely from one cluster to another. In response to these challenges, we demonstrate a platform for trapping-assisted SERS. A photonic crystal cavity is used to trap the silver nanoparticles. We monitor the trapping process by measuring the shift in cavity resonance wavelength with the trapping of each additional nanoparticle. We simultaneously measure SERS signals from the molecules on the silver nanoparticles, and observe a strong increase in these signals with the trapping of each additional nanoparticle. Our device employs optical forces to create nanoparticle clusters, and the associated SERS hotspots, in a controllable manner. Our method therefore combines the reproducibility and control of the first class of SERS substrates discussed above (those based on solid substrates) with the low cost of the second class of substrates (those based on colloidal nanoparticles). Furthermore, after the SERS spectrum has been measured, the nanoparticles can be released and new nanoparticles trapped and SERS spectra again measured. In this way, a SERS device with a “continually replenishable” sensing surface is achieved.

# Chapter 2 Optical trapping with microring resonators

Among the structures employed in photonic chips, the microring resonator coupled to a single bus waveguide is one of the most investigated, due to its multifunctional nature and simplicity. A variety of applications have been demonstrated, including optical modulators[65], filters[3], and sensors[15]. The high field enhancement and its planar nature make the microring a promising candidate for on-chip optical trapping and manipulation as well. In this chapter, we describe our work on the optical trapping of polystyrene particles with microring resonators. We experimentally demonstrate the trapping of polystyrene beads with diameter from 200 nm to 5.6 μm using microring resonators on a silicon chip and analyze the trapping performance and optical force enhancement.

## 2.1 Introduction to optical trapping with microrings/microdonuts

Whispering-gallery mode cavities such as microrings and microdisks have been reported with quality factors as high as $10^6$[66], [67]. The simplicity of their design and fabrication make them a good candidate for the demonstration of cavity trapping. In addition to the gradient force that permits the trapping of objects on the surface of the cavity, the scattering force due to the traveling wave nature of the whispering-gallery mode enables the trapped objects to be pushed and circulate along the light path. This could lead to novel applications such as viscosity

measurement. This could also provide a micromotor functionality, for example moving a catalytic agent to accelerate a chemical reaction.

Figure 2-1(a) shows the schematic diagram of our planar micro-ring cavity trapping system. The trapping laser is coupled to the microring through the bus waveguide. A typical field distribution ($H_x$: $x$-component of magnetic field) on an $x-z$ plane cross section is shown in Figure 2-1(b). This field distribution is found using FDTD simulations. The rapid decay of the optical field with distance from the surface results in a gradient force that pulls the particles toward the microring.

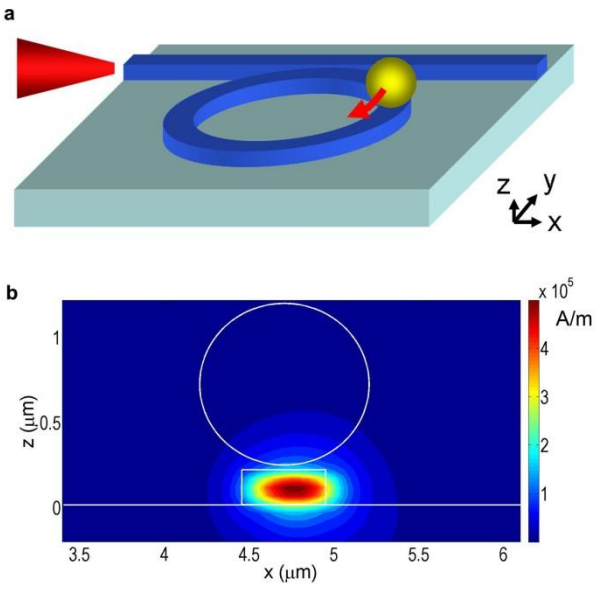


**Figure 2-1. (a) Schematic diagram of planar micro-ring cavity trapping system; (b) cross section of the instantaneous field distribution ($H_x$: $x$-component of magnetic field) of the whispering-gallery mode of the micro-ring by 3D-FDTD simulation with a 1 W input power in the waveguide. The outer edge of the micro-ring is at x ≈ 5μm.**

## 2.2 Design considerations for microring trapping

As we discuss below, the transverse magnetic field (TM) mode has favorable properties for optical manipulation. In Figure 2-2, we consider a channel waveguide whose width (500 nm) is larger than its height (220 nm). The waveguide is assumed to be formed on a silicon-on-insulator (SOI) wafer with a buried silicon dioxide (box) layer of 3 μm. It can be seen that the TM mode is less confined and has larger evanescent field on top of the core region than the TE mode does. In the dipole approximation, the optical force exerted on a particle is proportional to the field intensity. One would therefore expect that the TM mode would exert a larger force. This is confirmed by calculations we perform with the Maxwell stress tensor method. We calculate the force on a polystyrene particle (radius 1 μm) 30 nm above the waveguide, and find that the force is five times larger for the TM mode than for the TE mode. The total mode power is the same in both cases. It is for this reason that we choose to employ the TM mode for our waveguide and microring trapping demonstrations.

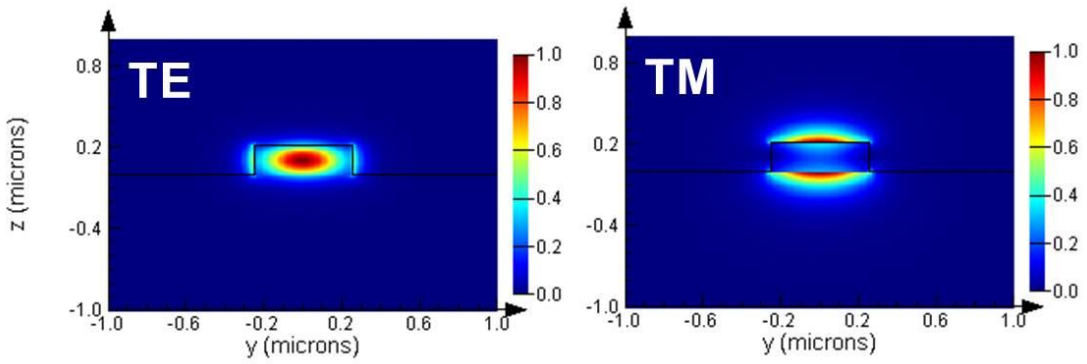


**Figure 2-2 Electric field intensity of the TE and TM mode for a silicon channel waveguide with a width of 500 nm, and a thickness of 220 nm.**

To enhance the optical force, a microring design with a high quality factor ($Q$) and small mode volume ($V$) is desirable, considering, as noted in Eq. (1.16), that the cavity field enhancement is proportional to $Q/V$. Reducing the microring radius reduces the mode volume. When the microring radius is smaller than 5 μm, however, the bending loss dominates, and causes a significant decrease of the quality factor. With these considerations in mind, we perform trapping experiments with microrings with radii of 5 μm and 10 μm.

Scattering due to the sidewall roughness is the main source of loss for microrings with radii larger than 5 μm. As discussed in the methods section, this motivates us to optimize the fabrication processes. This furthermore motivates us to employ a microdonut design later (Chapter 6), in which the width of the ring is increased from 500 nm to 1 μm, thereby suppressing scattering loss on the inner sidewall. The microdonut design has the advantage over microdisks that higher order whispering-gallery modes are suppressed. This significantly simplifies the analysis of the experimental results, making it easier to identify the modes responsible for the optical trapping.

## 2.3 Experiment design

### *2.3.1 Device fabrication*

Micro-rings with radii of 5 and 10 μm and widths of 500 nm are fabricated on silicon-on-insulator (SOI) wafer with a 220 nm top Si layer using electron beam lithography and

reactive ion etching. Figure 2-3 shows a schematic diagram of the fabrication process and a photograph of the fabricated device. The fabrication process begins with cleaving the SOI wafers into chips Each chip is then coated with polymethylmethacrylate (PMMA) resist followed by a prebake at 180 ℃ for 10 minutes, and the patterns are exposed using electron beam lithography with an acceleration voltage of 100 kV (Elionix ELS-7000). After developing the chip in methyl isobutyl ketone (MIBK) for 90 seconds, the patterns are transferred to the top Si layer by dry etching using $SF_6$ and $C_4F_8$ gases with a forward power of 800 W (STS MPX/LPX ICP RIE).

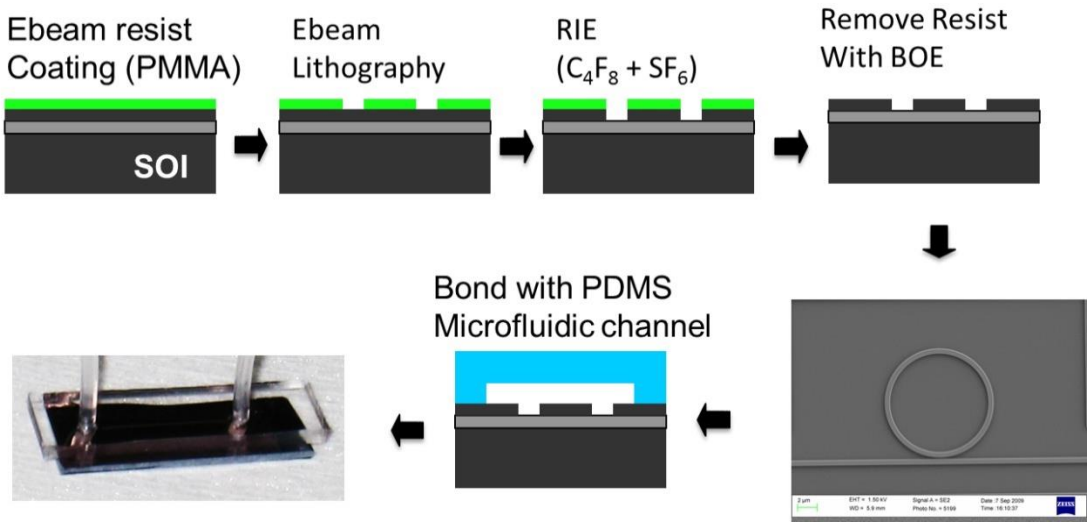


**Figure 2.3 Fabrication process of optical manipulation device that integrates silicon microcavity resonators and waveguides with PDMS microfluidic channels.**

Light is coupled into and out of the resonator with a bus waveguide with a width of 500 nm. The ring-bus gap is 150 nm. A PDMS microfluidic channel with a height of 50 μm and a width of 200 μm is bonded on top of the resonator structure. The surfaces of both silicon chip and PDMS are activated by oxygen plasma treatment for 20 seconds with a power of 60 W. Tubes are

connected to the inlet and outlet of the microfluidic channel, through which the particle are injected to the microfluidic channel with a syringe. These particles are fluorescent polystyrene and are mixed with deionized water.

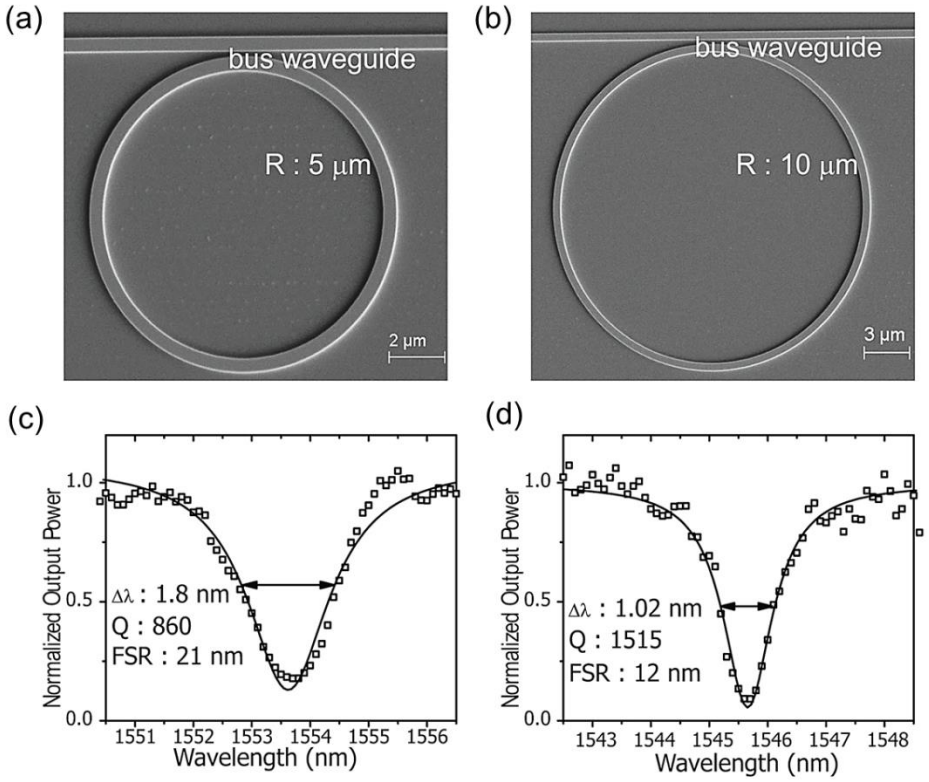


**Figure 2-4 SEM images of micro-rings with radii of (a) 5μm and (b) 10 μm. Transmission spectra of rings with radii of (c) 5 and (d) 10 μm, respectively. Black squares are measured output powers. Lines are the Lorentzian fits to the measured data. Free spectral range (FSR) and the full width of the half maximum of the resonance peak (Δλ) are also shown in (c) and (d).**

Figure 2-4(a) and (b) show scanning electron microscope (SEM) images of fabricated silicon microrings with radii of 5 and 10 μm, respectively. From the transmission spectra of micro-rings

in Figure 2-4(c) and (d), the quality factor ($Q$) of the 10 μm micro-ring is measured to be 1515, which is larger than that of the 5 μm micro-ring ($Q$ = 860) due to the smaller bending loss. The free spectral ranges (FSRs) are measured to be 12 and 21 nm for 5 μm and 10 μm microrings, respectively. The intensity enhancement *G* in the microrings can be calculated by Eq. (1.7). An intensity enhancement of 1.76 for the 10 μm micro-ring is achieved, compared to a 1.50 intensity enhancement for the 5μm micro-ring. The intensity enhancement leads to larger optical forces with the micro-rings than with straight waveguides.

### *2.3.2 Measurement setup*

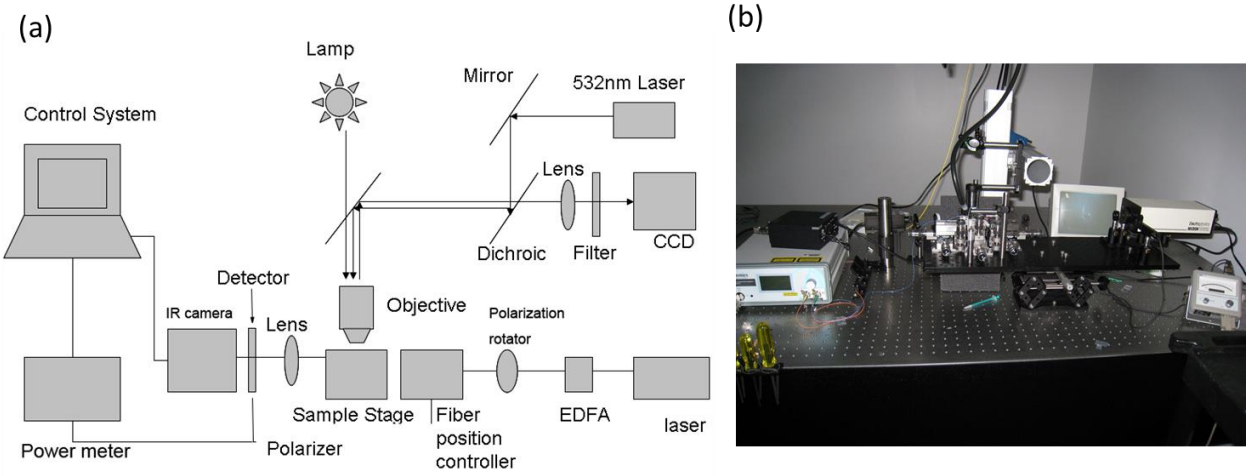


**Figure 2-5 (a) Schematic diagram of the measurement setup, (b) photo of the homemade measurement setup.**

Figure 2-5(a) shows a schematic diagram of the measurement setup that combines a fiber coupled waveguide characterization system with a fluorescent imaging system above the device. The output of a tunable laser (HP8168, near λ=1550 nm) is amplified by a high power C-band

erbium-doped fiber amplifier (EDFA) and launched into the waveguide to excite TM modes. A lens-tipped fiber with a focal spot size of 3 μm is used to couple light into the waveguide, and a coupling loss of approximately 10 dB is achieved. The output from the bus waveguide is focused onto a germanium photodetector to measure the transmitted power. A fluorescence microscope is used to monitor the trapping process. Fluorescence from the polystyrene particles is excited with a green laser (λ=532 nm, P=0.75 mW). The fluorescent emission is imaged by a microscope objective (Nikon, NA 0.55, 50X) onto a charge coupled device (CCD) camera, with a longpass filter used to suppress the green excitation laser. Figure 2-5(b) shows a photograph of the system.

## 2.4 Experimental results

We experimentally measure the particle velocity as a function of coupling power and compare the results to numerical simulations. In addition, we measure the shape and depth of the two dimensional optical potential over the ring by tracking a particle's position over several revolutions with a high speed camera.

### *2.4.1 Force enhancement and wavelength dependence*

We observe the trapping of 1.1 μm diameter polystyrene particles that revolve around the microring at a few hertz and are stable for several minutes. Depending on the particle concentration and flow conditions, single or multiple particles are trapped. Supplementary Movie 2-1 shows three particles being delivered along the bus waveguide to a 5 μm microring, where

they are then trapped at a power of 5 mW. A movie is recorded by a CCD camera at 60 frames per second. Each trapped particle moves around the microring with approximately constant velocity that is dependent on the power coupled into the bus waveguide and the finesse of the microring resonator.

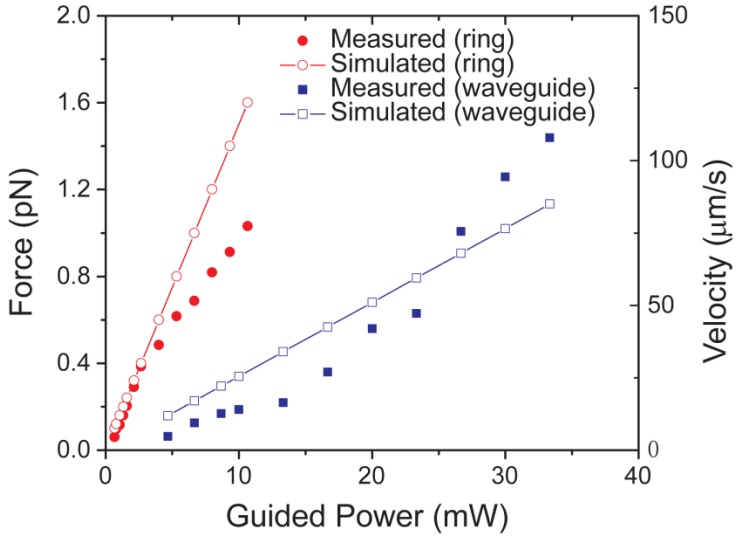


**Figure 2-6 Measured velocity (right axis) and optical force (left axis) on circling particles plotted as a function of input power for straight waveguide and micro-ring (r = 5 μm) trapping. The squares and circles correspond to measured data on resonators, and straight waveguides, respectively, and the lines with open symbols correspond to simulation results.**

In Figure 2-6, the measured and simulated power dependence of the optical force along the light propagation direction is shown for a straight waveguide and the 5 μm radius micro-ring resonator. The longitudinal force is found from the measured particle velocity using the Stokes' drag formula[68]:

$$F = 6\pi \cdot r \cdot \eta \cdot v \tag{2.1}$$

where $r$ is the particle radius and $v$ is the measured particle velocity. The longitudinal force found in this way is shown on the left-hand axis of Figure 2-6. We assume no significant temperature change during the measurement, and the room temperature dynamic viscosity of water ($\eta$ = $8.9\times10^{-4}$ Pa·s) is used in the calculation. The simulated force is calculated using a Maxwell stress tensor formalism using the electric and magnetic fields found from FDTD simulations. The Debye length of the solution is $21 \pm 9$ nm. Previous near-field optical trapping studies reported particle-cavity gaps slightly larger than the Debye length [50]. While we do not know the precise gap between the particle and the waveguide surface, for the calculation we assume a gap of 30 nm. Both the microring and waveguide measurements show an approximately linear increase of optical force with guided power, and are close to the values predicted by simulations. Possible sources of error include temperature variations, transient flows in the channel, and increased drag due to the proximity of the silicon-water interface. The minimum guided power required for stable trapping on the waveguide is 4.7 mW, which is comparable to other reported results of trapping on waveguides. However, particles can be trapped and propelled along the micro-ring resonator with a guided power as low as 0.67 mW. At the same guided power level, the measured velocity of particles on a micro-ring is 5-8 times larger than that on a waveguide.

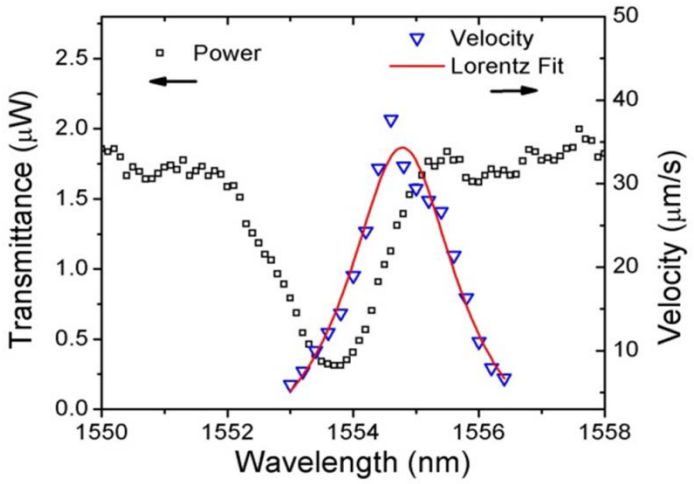


**Figure 2-7 Transmission spectrum of the micro-ring resonator near a TM resonance mode, and the circling velocity of polystyrene beads, as a function of wavelength. The blue triangles are experimentally measured data and the red trace is a Lorentzian fit.**

Because of the resonant nature of the micro-ring, the optical force depends on the incident wavelength. Figure 2-7 shows the average velocity as a function of excitation wavelength of eight trapped beads that are simultaneously circulating the 5 μm micro-ring. A guided power of 3 mW in the bus waveguide is used. For comparison, the spectrum of an unloaded ring is also plotted (black squares). The velocity of the eight particles peaks at a wavelength that is red-shifted by 1 nm compared to the unloaded micro-ring resonance. This red-shift of resonance is due to optical perturbation to the microcavity that results from the trapped polystyrene beads.

### *2.4.2 Force measurement in longitudinal direction*

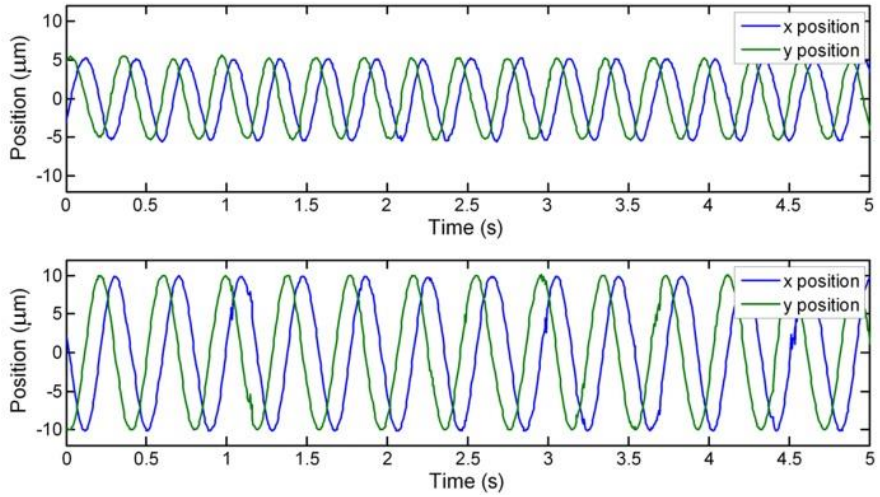


**Figure 2-8 Tracked positions of single particles trapped on micro-rings with radii of (a) 5 μm and (b) 10 μm.**

In addition to a large longitudinal force along the circumference of the ring, the particle also experiences a large transverse force across the radial direction. This force keeps the particle stably trapped, enabling it to circulate for several minutes, limited only by the stability of the flow conditions in the microfluidic channel. Supplementary Movie 2-2 shows two particles trapped on the 10 μm ring. Figure 2-8 shows the $x$ and $y$ positions of a particle trapped on 5 μm and 10 μm micro-ring resonators. These results are found by tracking the centroid of the trapped particle from a video taken at 200 frames per second. The powers coupled into the bus waveguide are 9 mW and 4.5 mW for the 5 μm and 10 μm microrings, respectively. As can be seen in Figure 2-7, the trajectories of the bead are periodic with frequencies of 3.4 and 2.5 Hz for the 5 μm and 10 μm micro-ring, respectively, corresponding to velocities of 110 +/- 10 μm/s and

160 +/- 5 μm/s. Bend loss reduces the field enhancement in the micro-ring at regions further away from the bus waveguide, resulting in a lower bead velocity in these regions.

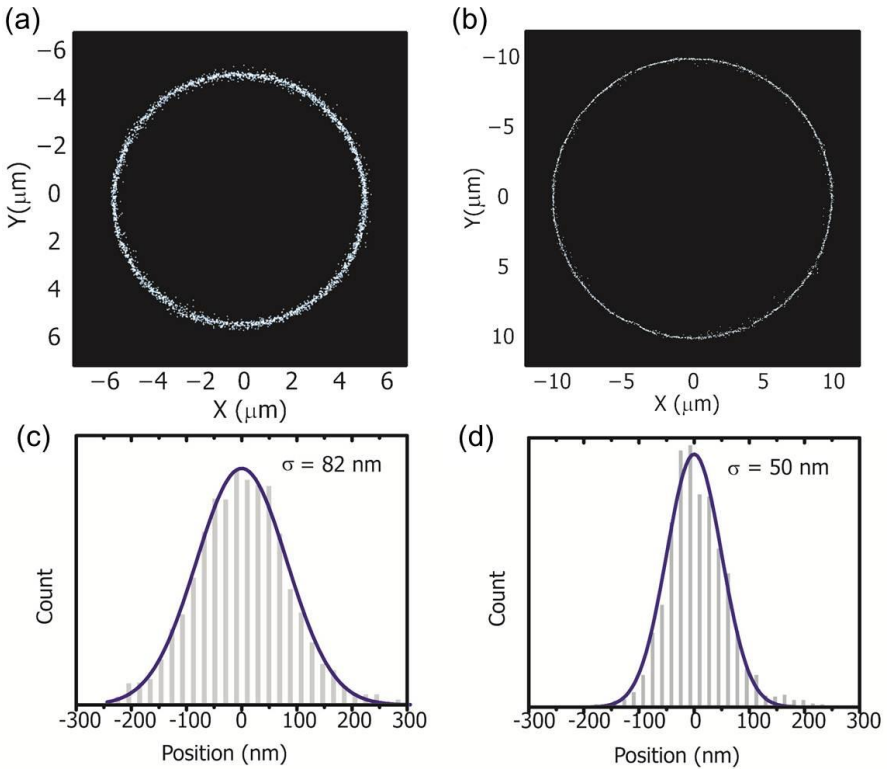


**Figure 2-9 Two dimensional histograms of trapped particle positions over the (a) 5 μm and (b) 10 μm microrings. One dimensional histograms of particle position along the radial direction for the (c) 5 μm and (d)10 μm microrings. Light is coupled to the ring from a bus waveguide above the ring, where the guided mode travels from right to left. Data is plotted as a function of *r*, the radial direction.**

By observing the particle position through several revolutions, the trapping potential can be mapped out. Figure 2-9 shows two dimensional histograms of particle position for the 5 μm and 10 μm microrings. The illumination power is the same as that used in Figure 2-8. The histograms

comprise 15 seconds of data, corresponding to approximately 51 and 38 revolutions, respectively. The bus waveguide runs along the top of the ring, and the guided mode propagates from right to left. Using the equipartition theorem, the radial trap stiffness can be calculated from the measured thermal motion shown in the histograms. The radial trap stiffness is found by calculating the standard deviation σ of the difference between the particle position and the center of micro-ring throughout the entire circumference of the micro-ring. The measured σ are 82 nm and 50 nm for the 5 μm and the 10 μm micro-ring, respectively. From these particle distributions, the radial trap stiffnesses are found to be 0.62 pN/μm for the 5 μm ring and 1.66 pN/μm for the 10 μm ring. As can also be seen in Figure 2-9(a) and (b), the 10 μm micro-ring localizes the particle more stiffly than the 5 μm micro-ring. In addition to the slightly larger finesse and field enhancement, the increase in relative force of the 10 μm micro-ring is likely also due to better coupling efficiency in this device. Both rings, however, stiffly confine the trapped particle over their entire circumferences, which have lengths of 31 and 62 μm. From simulations, we find that the maximum force exerted on a trapped particle on a micro-ring occurs when the bead is approximately $w/2$ away from the trap center, where $w$ is the width the waveguide. At $w/2$ from the trap center, the product of trap stiffness with extension $k \times w/2$ is 0.16 pN for the 5 μm micro-ring at a power of 9 mW, corresponding to a potential depth of $9.3\, k_B T$. Similarly, a potential depth of $25\, k_B T$ is achieved for the 10 μm micro-ring at a power of 4.5 mW. Here, the potential depth is calculated by $U = k \times (w/2)$, assuming a Gaussian potential well. This expression gives the potential depth of a Gaussian potential well, where $k$ is the trap stiffness at the center and $w/2$ is the position at which the gradient maximum force occurs. This is a

reasonable assumption as the potential associated with gradient force and the intensity are proportional in the dipolar limit. Three dimensional FDTD simulations confirm that the intensity on the top of the ring follows a Gaussian distribution.

We have successfully trapped polystyrene particles with diameters from 200 nm to 5.6 μm using microring resonators with radii of 5 μm. Supplementary movie 2-3 shows a 5.6 μm particle that is trapped and circulates around the microring. To further improve the optical force for smaller particles, microcavities with higher quality factors and/or smaller mode volumes would be needed. Photonic crystal cavities are a promising candidate, as discussed in Chapter 4.

**2.5 Summary**

In summary, we have experimentally demonstrated optical trapping of dielectric particles on Si micro-ring resonators. The particles are stably propelled around the ring circumference with velocities as high as 180 μm/s for several minutes. We measure a 5-8 times enhancement of the optical force for a micro-ring of radius of 5 μm, compared to a straight waveguide. In addition, the power required for stable trapping is reduced to be as low as 0.67 mW. A $25\ k_BT$ potential depth is measured from a particle position histogram for the 10 μm micro-ring.

# Chapter 3 Particle buffering with double-ring structures

In this chapter, we demonstrate devices with the ability to store particles and deliver them to other locations on the chip. We term this functionality “buffering”, and achieve it by integrating multiple microrings with different resonant wavelengths with one waveguide. In the previous chapter, we demonstrate that particles can be delivered along a waveguide and trapped on microrings with enhanced optical force. Here, we demonstrate that tuning the laser wavelength to the resonance wavelengths of different rings enables trapped particles to be transferred back and forth between the rings. The techniques we describe here could form the basis for small footprint systems in which objects are moved between multiple locations on a chip, at each of which different operations are performed and the objects’ properties sensed.

## 3.1 Introduction to particle buffering

The precise manipulation of micrometer size objects is advantageous for lab-on-a-chip devices, for applications such as the handling of single cells[37], flow cytometry [69] and self-assembly [70]. The transport of microparticles in microfluidic devices can be achieved using approaches such as pressure driven flow and traveling wave dielectrophoresis. However, using these techniques, the manipulation of a single particle in a precisely controllable manner is difficult. Using optically-induced dielectrophoresis, Chiou *et al* demonstrated the dynamic manipulations

of microparticles down to the single particle level [71]. However, the requirement that the experiments be performed in low conductivity buffer, and the difficulty with which small particles are manipulated, limit its applications. Lee *et al* also demonstrated a single cell transportation technique based on magnetic forces [72]. This approach is only suitable, however, for particles with a magnetic moment, meaning that, as the authors described, additional sample preparation steps are needed.

The use of optical forces to manipulate nanoparticles and biological materials has attracted attention recently due to their ability to operate on the single particle level, the possibility of reconfiguring the trapping potential, and their non-invasive nature. Integrated optical manipulation has several advantages over free space optical tweezers as discussed in Chapter 1. The use of integrated photonic devices such as microrings offers the possibility for optical manipulation with multiple traps operating in parallel, in a system with a far smaller footprint than traditional optical tweezers based on microscopes.

Despite progress in the field of integrated optical manipulation chips, in which photonic tweezer structures are integrated with waveguides, the ability to store a single particle at different locations on the chip, and to move it between these positions, has not, to the best of our knowledge, been demonstrated. Here, we demonstrate this functionality. We demonstrate two particle buffer chain designs in which two microrings are integrated on the same waveguide. We show that tuning the laser wavelength to the resonance wavelengths of different rings enables

trapped particles to be transferred back and forth between the rings.

### 3.2 Design and fabrication

Each particle buffer chain consists of two microrings with different resonance frequencies. In the first design, termed a one-way particle buffer chain, two microrings, separated by several tens of μm, are integrated with a bus waveguide. By changing the wavelength of the laser input to the chip, particles can be switched from the first ring to the second, traveling between them on the waveguide. In the second design, the two microrings are located on opposite sides of the bus waveguide, about the same position along it. This enables trapped objects to be switched back and forth between the rings by modifying the laser wavelength. We term this device a two-way particle buffer chain.

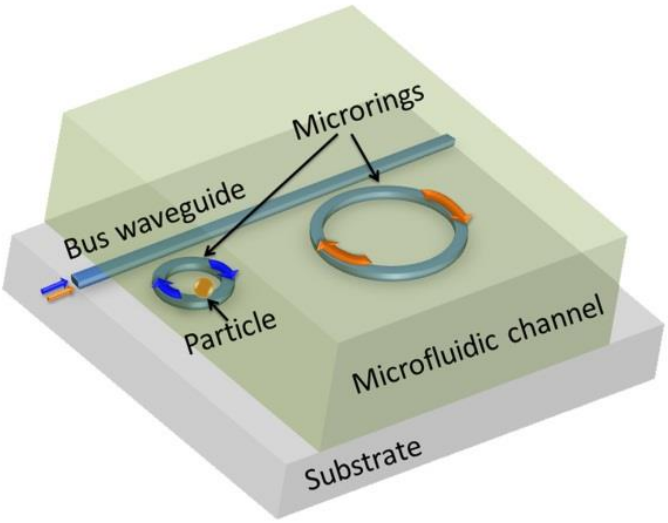


**Figure 3-1 Schematic diagram of one way particle buffer chain, consisting of two microrings coupled to a bus waveguide**

Figure 3-1 shows the schematic diagram of the one-way particle buffer chain, comprising two microrings integrated with a waveguide. Microrings are fabricated in the top silicon layer (220 nm thick) of a silicon-on-insulator (SOI) wafer. The fabrication process is described in section 2.3.1. A PDMS chip containing microfluidic channels (50 μm high, 200 μm wide) is bonded to the chip containing the Si microrings, and chip is placed in an experimental set-up for optical manipulation demonstrations. The measurement setup is the same as that used for the microring trapping experiments described in section 2.3.2. Fluorescent polystyrene particles with diameters of 1.1 μm are delivered to the trapping region through the microfluidic channel.

## 3.3 Experimental results

### *3.3.1 Particle switching between the waveguide and microring*

We first demonstrate that the particle can be switched between the bus waveguide and microring by tuning the wavelength of the trapping laser. The microring only traps particles when it is on resonance, which requires the incident wavelength of the trapping laser to match the resonance wavelength of the microring. In that case, the enhanced optical field on the mirroring pulls the particles from the waveguide to the microring. If the microring is off resonance, however, the optical field propagates along the bus waveguide without coupling to the microring. Particles trapped on the microring can therefore be switched back to the bus waveguide by tuning the laser wavelength away from the resonance frequency of the microring. We use a single ring (radius 5

μm) with a guided power of 5 mW to demonstrate this switching process. The microring trapping experiment discussed earlier in this thesis shows that this power is sufficient to propel particles along a straight waveguide. The entry of particles from the waveguide to the microring and the release of the trapped particles to the waveguide are achieved by shifting the incident wavelength onto, and away from, the resonant frequency, respectively. This process is demonstrated in Supplementary Movie 3-1. This demonstration suggests that microrings can effectively serve as buffers for the storage of microparticles or biological materials such as cells. This motivates us to integrate several rings on a waveguide, as we describe below.

### *3.3.2 One-way particle buffering demonstration*

The one-way particle buffer chain (Figure 3-2(a)) consists of two microrings, with radii of 5 μm and 10μm, integrated with a bus waveguide. The microrings have widths of 500 nm. The design value for the gap between microrings and bus waveguide is 150 nm. The bus waveguide has the same width (500 nm) as the microrings. The transmission spectrum in Figure 3-2(b) shows resonances at 1557.9 nm and 1561.2 nm that correspond to the microrings with radii of 5, and 10 μm, respectively. The relatively modest Q (~800) of the microrings has the favorable attribute of preventing trapping from being lost due to particle-induced resonance shift. The insets on the bottom of Figure 3-2(b) are CCD images of the particle buffer chain when the input laser is tuned to the resonance wavelengths of the smaller (left image) and larger (right image) rings. It can be seen that particles are only trapped on the on-resonance ring. The trapped particles are indicated

with white arrows, and the positions of the rings and waveguide are indicated by yellow lines. When the laser wavelength is tuned away from the center of the resonance peak, less power is coupled into the resonator, and the velocities of the trapped particles decrease. When the laser wavelength is shifted further from the resonant wavelength of the ring, the field intensity in the ring resonator becomes smaller than that in the waveguide. Particles that are in the coupling region when this occurs are therefore released to the bus waveguide. The released particles are propelled along the waveguide. If the laser wavelength matches the resonant wavelength of the second ring (1561.2 nm), then the particles are trapped by it. Supplementary Movie 3-2 shows that a trapped particle is delivered from the smaller to the larger ring by tuning the incident wavelength from 1557.9 nm to 1561.2 nm. We anticipate that this precise position control capability could lead to various applications. For example, it could enable the response of an individual cell to different solvents to be studied. This could be achieved by having the first microring located in a channel containing a particular solvent, and the second microring located in a channel containing a second solvent. A cell could be trapped on the first ring, and then on the second, in a controllable manner.

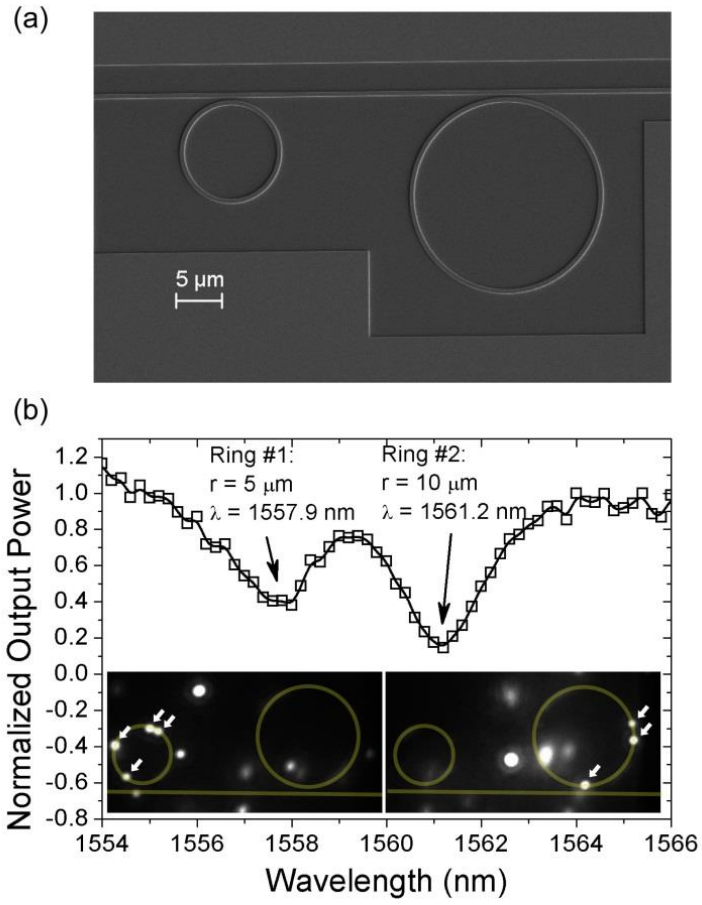


**Figure 3-2 (a) SEM image of the double-ring structure, (b) transmission spectrum of a particle buffer chain comprised of two microrings with radii of 5 and 10 μm. Dips at 1557.9 nm and 1561.2 nm correspond to the resonance frequencies of small and large microrings, respectively. Lower right inset: CCD image of particles trapped on small microring at a laser wavelength of 1557.9 nm; Lower left inset: CCD image of particles trapped on large microring at a laser wavelength of 1561.2 nm. Yellow lines label the positions of micro rings and bus waveguides. The white arrows indicate the trapped particles.**

### *3.3.3 Two-way particle buffering demonstration*

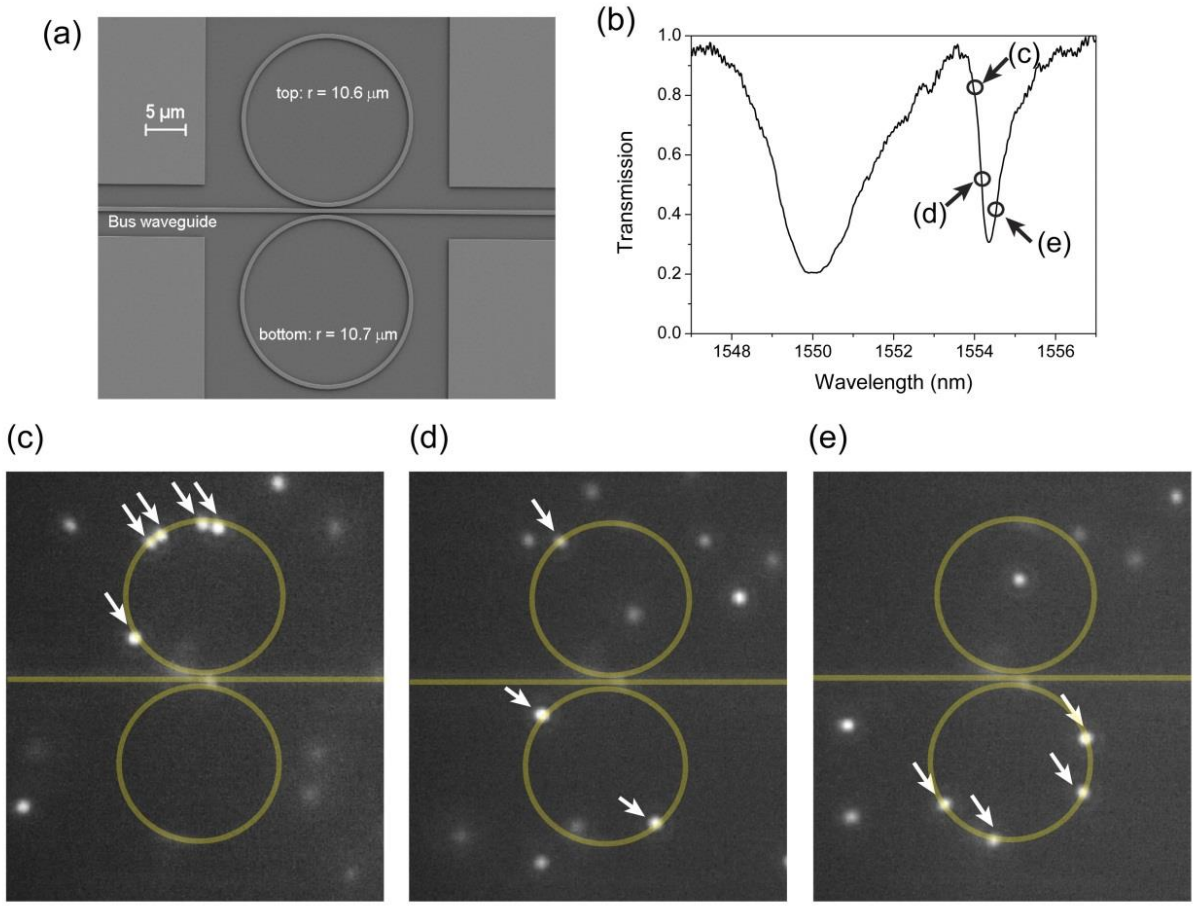


**Figure 3-3 (a) SEM image of the two way particle buffer chain. (b) Transmission spectrum of the microrings with radii of 10.6 and 10.7 μm. Dip at 1550.0 nm corresponds to mode with majority of field confined in top microring, and dip at 1554.4 nm corresponds to a hybrid mode. (c-e) CCD image of particles trapped on different microrings at different laser wavelengths, whose values are indicated in panel (b). Yellow lines depict the positions of microrings and bus waveguides. White arrows indicate the trapped particles.**

The particle buffer based on previous design can only deliver particles in one direction, unless

the propagation direction of the light in the waveguide is changed. This means that particles cannot be switched back and forth between microrings, unless the light direction is changed. To switch trapped particles back and forth without needing to do this, we use the structure shown in Figure 3-3(a). This device, which we term a two-way particle buffer chain, consists of microrings fabricated on opposite sides of the bus waveguide. The top (bottom) microring has a radius of 10.6 (10.7) μm. The gaps between bus waveguide and microrings are 100 nm.

Different from the one-way particle buffer case, the two cavities can couple with each other to form hybrid modes, whose field distributions are sensitive to the wavelength. Figure 3-3(b) shows the measured transmission spectrum. The broader peak at 1550 nm corresponds to the resonance mode with the majority of its field confined in the top microring. A hybrid mode with a sharp dip around 1554.4 nm can be seen. FDTD simulations show that the field distributions of this hybrid mode changes dramatically as the laser wavelength is varied about the resonance. As the wavelength is tuned from 1554 nm to 1554.5 nm, the field intensity in the bottom microring becomes increasingly large compared to the top microring. Particles are preferentially trapped on the microring with the higher field intensity, which can be controlled by tuning the incident wavelength. This is demonstrated in Figure 3-3(c-e). In Figure 3-3(c), the laser wavelength is 1554 nm, and particles are trapped on the top microring only. In Figure 3-3(d), the laser wavelength is 1554.15 nm, and particles are trapped on both rings. Lastly, in Figure 3-3(e), the wavelength is 1554.5 nm, and particles are trapped only on the bottom ring. In Supplementary Movie 3-3, we demonstrate that we can switch a particle back and forth between the two

microrings by tuning the laser wavelength between 1554.5 nm and 1554 nm. In the Movie, the particle circulates twice around the corresponding microring in each step of the trapping process. The particle is released to the bus waveguide by setting the laser wavelength to be 1555.5 nm.

### 3.4 Summary

We experimentally demonstrate two switchable particle buffer chains for on-chip particle trapping and. With the ability to quantitatively store particles on a microring, deliver them from one location on the chip to another, and switch them between rings, the demonstrated particle buffer chains could be used as building blocks in the construction of larger systems with additional functionalities. The one-way and two-way buffer chains we demonstrate present the interesting possibility of a “micro production line”, where objects are transported between different locations on a microfluidic chip, at each of which modification or characterization is performed. The planar nature of the microring resonators potentially enables on-chip integration with other lab-on-a–chip components, and permits the all-optical delivery, storage and routing of microparticles, nanoparticles or biological materials such as cells.

# Chapter 4 Optical trapping with photonic crystal cavities

Whispering-gallery mode cavities such microrings have relatively large mode volumes, which prevent them from achieving high field enhancement, unless their quality ($Q$) factors are very high. Planar silicon cavities, however, have relatively modest $Q$ factors compared to their stand-alone counterparts such as microspheres and microtoroid cavities. The latter, however, are usually coupled to with tapered optical fibers mounted on high precision piezoelectric translation stages, making them less suitable for large-scale lab-on-a-chip integration. Photonic crystal cavities have much smaller mode volumes that microrings, and comparable Qs are achievable by carefully engineering the effective refractive index near the cavity. Moreover, unlike mirorings, photonic crystal cavities are standing wave resonators, meaning that the particle is trapped about a fixed position, rather than circulating with the propagating wave. In this chapter, we present our results on the design of a high $Q$ factor one dimensional (1D) photonic crystal cavity with a nanoslot in the center. Both the cavity resonance and nanoslot contribute to a dramatically larger optical force. We experimentally demonstrate the optical trapping of polystyrene and silver particles using 1D photonic crystal cavities.

## 4.1 Design and simulation of 1D photonic crystal cavity for trapping

We design, then numerically verify, a novel nanoslotted waveguide photonic crystal (PhC) cavity for near-field trapping. Resonant enhancement of the optical fields effectively reduces the input

power required for stable trapping. Further, introduction of a nanoslot structure to the PhC cavity takes advantage of the large electric field discontinuities at the dielectric boundaries, resulting in significant field concentration and enhancement[56], [73], [74]. We show that such a cavity-based trapping device is capable of single nanoparticle trapping, and that the nanoslot cavity device setting is also ideal for single nanoparticle detection, given the strong cavity-enhancement effect and the ultra-small interrogation volume.

### *4.1.1 Device design*

The proposed waveguide PhC structure consists of a 1D hole array in a silicon-on-insulator (SOI) photonic wire waveguide, as shown in Figure 4-1. The refractive indices of the silicon and silicon dioxide are taken as 3.46 and 1.45, respectively. The hole array period $a$ is 420 nm and the radius of the holes is 100 nm. A PhC cavity with a length of $d = 930\,nm$ is formed between two linear hole arrays. A 3rd-order resonant mode confined in the cavity, near a wavelength of 1.55 μm, exhibits an enhanced field intensity which peaks in the center of the cavity.

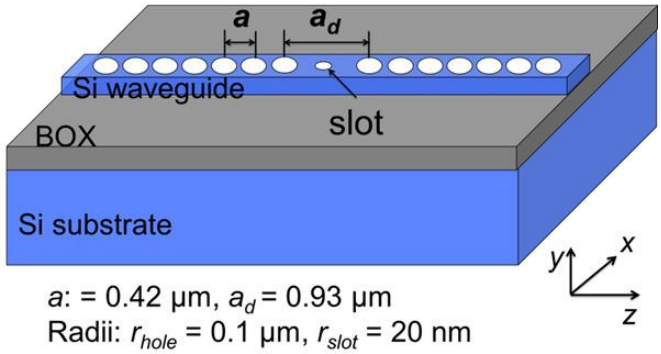


**Figure 4-1 Schematic illustration of a nanoslot waveguide photonic crystal cavity.**

Tapered boundary regions with locally varied hole spacing are used to reduce the impedance mismatch between the Bloch mode and the waveguide mode. The refractive index of the Bloch mode can be calculated from $n = \lambda/2a$, and is 1.84 for our design. The refractive index of the waveguide mode is found to be 2.26 using numerical simulations with a mode solver. In our simulations, each tapered region consists of four holes with radii of 96, 92, 88, and 84 nm. The spacing between the holes is also adjusted locally to maintain a constant $r/a$ ratio in the tapered regions. Compared to a conventional PhC cavity design with an abrupt disruption of the periodicity, such a tapered cavity design minimizes out-of-plane radiative loss of the cavity mode and improves the cavity $Q$-factor from 130 to 1850 (Figure 4-3)[75].

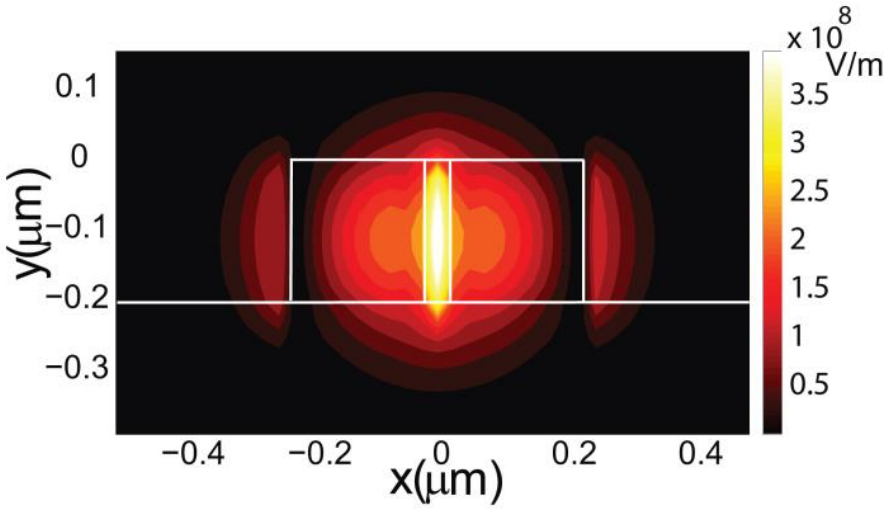


**Figure 4-2 $E_x$ field distribution in the plane $z = 0$, showing strong field confinement in the nanoslot**

To further increase the field enhancement, beyond that provided by resonant cavity enhancement,

we incorporate a nanoslot structure to leverage the large field discontinuities at high-index-contrast dielectric boundaries[74]. In our simulation, a nanoslot is formed by introducing a 20 nm radius hole in the center of the cavity, as schematically illustrated in Figure 4-1. Figure 4-2 plots the $E_x$ field component on an $x-y$ plane cross section through the nanoslot. It is clear that the nanoslot contributes to high optical field localization. Based on the strong degree of field confinement and enhancement, this design presents exciting opportunities for the trapping and detection of single nanoparticles with sizes down to a few tens of nanometers. As we discuss further in the experimental section, however, measurements we carry out with devices incorporating nanoslots indicate the possible presence of thermal convection effects. It appears that the enhanced fields from the nanoslot lead to water being heating. This suggests that the nanoslot design will be most favorable when used at wavelengths for which water absorption is lower than at λ=1550 nm.

### *4.1.2 Simulation of the optical forces*

We perform 3D FDTD simulations to determine the field distribution in this structure when the nanoparticle position is varied. The power input to the waveguide is taken as 5 mW. Numerical simulations predict that 18 percent of the incident power is transmitted through the device. A polystyrene particle (refractive index n = 1.59) with a radius of 10 nm is used in the simulations. It is assumed that the medium above the device is water (n = 1.33). The gradient force along the $y$ axis is calculated by integrating the Maxwell stress tensor over the particle surface.

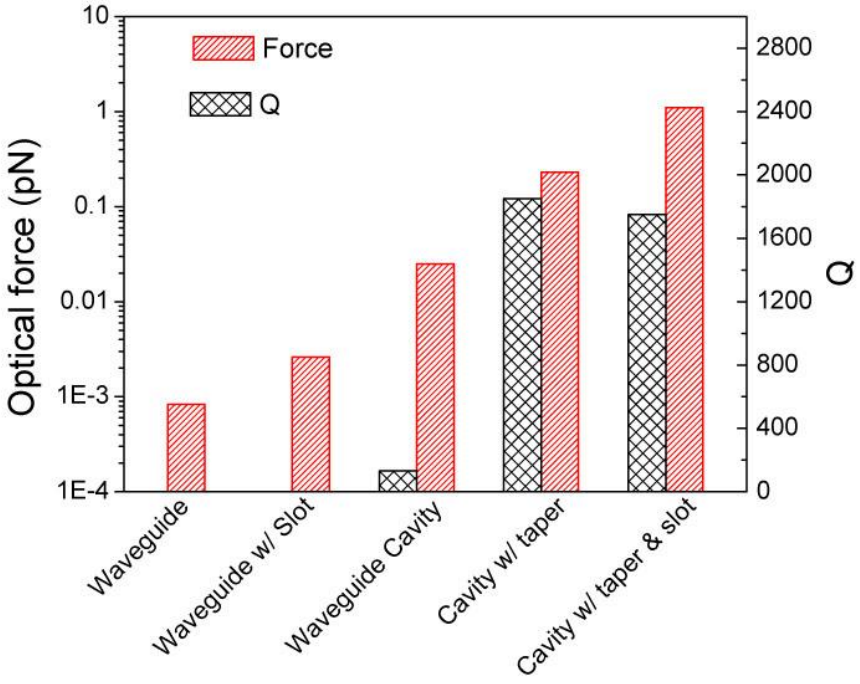


**Figure 4-3 Cavity Q-factor and corresponding optical gradient force along y-axis in a waveguide, a waveguide PhC cavity, a waveguide PhC cavity with a taper only, and a waveguide PhC cavity with both a taper and a nanoslot.**

From Figure 4-3, it can be seen that introducing a nanoslot into the waveguide enhances the gradient force by ~3 times. The optical gradient force for the PhC cavity structure is ~30 times larger than that of the waveguide-only device. A further nine-fold enhancement of trapping force is obtained by incorporating the tapered structure due to the increased cavity $Q$-factor. The introduction of the nanoslot also leads to a further five-fold enhancement of the trapping force by confining the high field intensity in the nanoslot. The decrease of the $Q$-factor from 1850 to 1750 arises from the cavity mode experiencing increased scattering loss due to the nanoslot. In these simulations, the particle is located on the surface of the waveguide at the entrance to the

nanoslot. This position is also employed for the simulations not incorporating the nanoslot or cavity. At this position, the field gradient and optical force have their maximal values. The particle position is denoted “above slot” in the inset of Figure 4-5.

### *4.1.3 Simulation of trapping potential well*

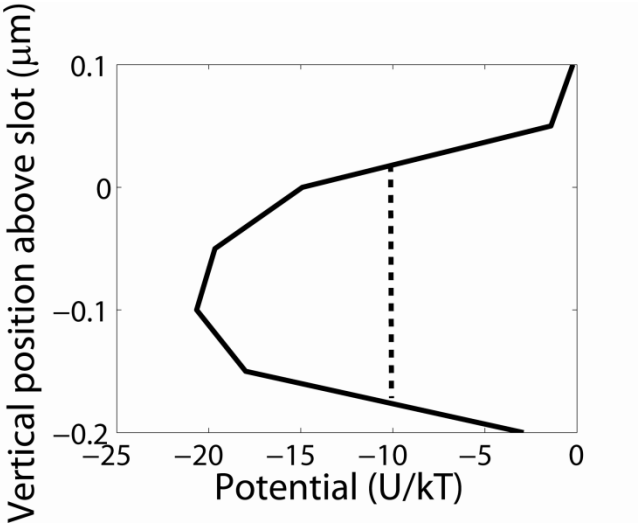


**Figure 4-4 Trapping potential well along y-axis normalized to kT. The broken line indicates a criterion of stable trapping (trapping potential > 10 kT). The potential is calculated by integrating the work done by the optical force on a nanoparticle with a refractive index of 1.59 and a radius of 10 nm.**

The gradient forces for a particle at different positions in the nanoslot are also simulated using

the Maxwell stress tensor approach. Figure 4-4 shows the potential profile along the $y$ direction, calculated by integrating the trapping force along the $y$-axis. Here the zero potential is defined as when the particle is at an infinite distance from the nanoslot. In practice, the zero potential point is taken as 2 μm from the waveguide surface, since the exponential decay of the fields in the $y$ direction means that there is negligible error in assuming this. The dramatic enhancement of optical force leads to a trapping potential $> 10k_BT$ even for particles with radii down to 10 nm (comparable to that of a single protein), which should allow the stable trapping of a single macromolecule inside the nanoslot cavity despite the presence of Brownian motion. Optical damage to the trapped molecule is estimated from the field intensity obtained from the simulation. The field intensity at the center of the nanoslot is 2.4 TJ/(m$^2$·s), found using

$$I = c \cdot \frac{\varepsilon|\vec{E}|^2 + \mu|\vec{H}|^2}{2} \tag{4.1}$$

A dose of 7.2 TJ/m$^2$ is required for detectable damage in DNA according to a previous study [76]. This allows us to estimate that DNA could be trapped in the center of the device for about 3 seconds before optical damage becomes significant. In addition, if we take into account the Brownian motion of the trapped molecule, the molecule effectually samples the field distribution inside the nanoslot, resulting in reduced optical damage compared to the estimation based on the peak field value in the slot center.

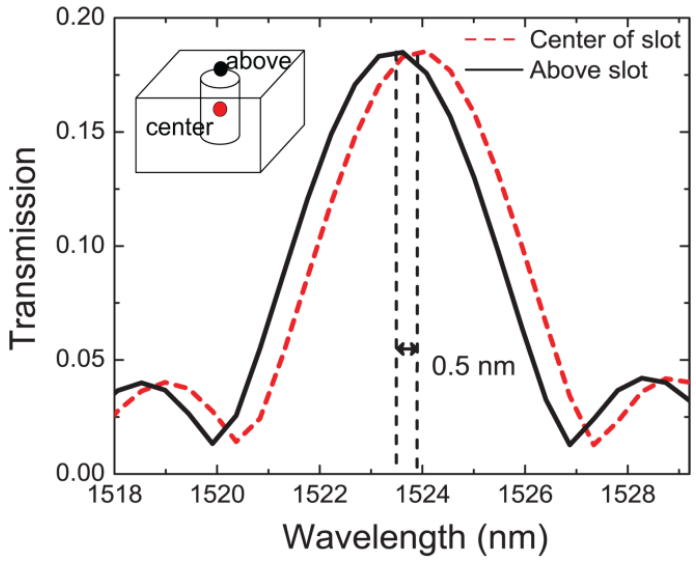


**Figure 4-5 Transmission spectra with a nanoparticle centered above the nanoslot. The high field concentration inside the nanoslot leads to the large 0.5 nm resonance spectral shift.**

We also quantitatively evaluate the field perturbation and the resulting resonant modification due to trapping of a single particle/molecule inside the nanoslot cavity for *in-situ* single particle detection [55]. Our results indicate that the optical trapping cavity also serves as a highly sensitive particle detection device suitable for rapid manipulation and analysis of particles/molecules. The resonance peak shifts 0.5 nm after trapping of a single nanoparticle in the center of slot, as shown in Figure 4-5. The majority of the optical mode energy is confined to a small region, meaning that even a small modification of the refractive index profile inside the cavity can lead to a large change of the cavity resonance frequency.

### *4.1.4 Simulation of in-plane optical forces*

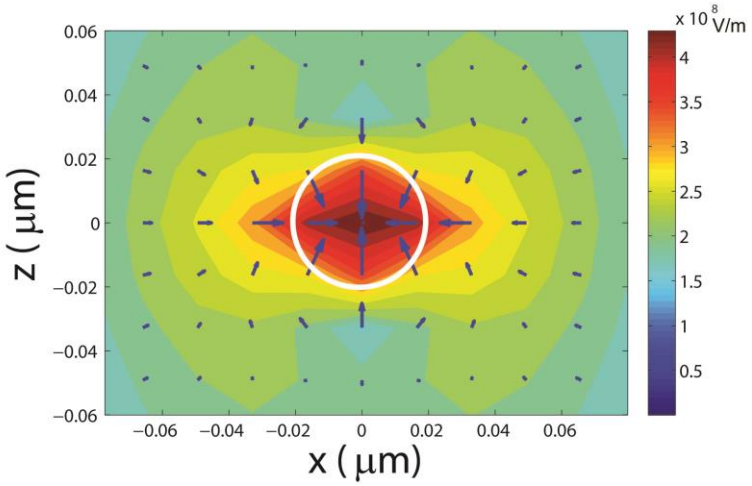


**Figure 4-6 Gradient force and $Ex$ field distribution in the plane on the top surface of the waveguide. The color represents the amplitude of $E_x$ field, assuming an incident mode from the waveguide with a power of 1 W. The blue arrows show the amplitude and direction of the gradient force for each particle position. The forces are calculated by the dipole approximation discussed in Chapter 1.**

The proposed device can be readily fabricated using conventional CMOS compatible technologies. Nanoparticle optical manipulation has recently been demonstrated in slot waveguides with similar dimensions [56]. The development of advanced fine-line lithography technologies has enabled the fabrication of these nanostructures as well as low loss optical waveguides. A microfluidic channel could be fabricated over the waveguide for nanoparticle transport to the device. The gradient force decays rapidly with distance from the nanoslot due to the exponential field decay. This would result in only the particles close to the waveguide surface being trapped by the nanoslot. Figure 4-6 shows the electric field ($E_x$ component) and gradient

force distribution on the surface of the waveguide near the nanoslot. The high degree of confinement of the cavity mode is evident, with maximal field intensity achieved inside and around the nanoslot. Gradient forces, shown as arrows, are calculated using the dipole approximation [77]. In the vicinity of the nanoslot, the gradient force points to the nanoslot center. This would help drag particles to the nanoslot. By integrating the gradient force with distance, we find a $7\ k_B T$ potential depth in the lateral direction ($x - z$ plane). This would help trap particles in the center of nanoslot and suppress the interactions between trapped particles and the side walls.

In summary, we have designed a waveguide photonic crystal cavity structure for nanoparticle manipulation and detection. Numerical simulations indicate that the device is capable of trapping nanoparticles with radii down to 10 nm with a low input power of 5 mW. Tapered boundary regions and a nanoslot contribute to strong light confinement in a subwavelength spot (~ 40 nm in our simulation). The high field intensity in the nanoslot enhances the optical force ~1300 times compared to a conventional channel waveguide. Importantly, the cavity trapping device also offers an ideal setting for characterization of the trapped particle/molecule using cavity-enhanced optical techniques. We foresee that this novel device can potentially become a versatile platform technology for single molecule, virus, or nanoparticle manipulation, detection and other “lab-on-a-chip” applications.

## 4.2 Experimental demonstration

In this section, we experimentally demonstrate the trapping of particles with the photonic crystal cavity. Results are presented on the trapping of polystyrene particles with diameters of 110 nm and silver nanoparticles with diameters of 80 nm.

### *4.2.1 Device fabrication*

The 1D photonic crystal cavities are fabricated on a silicon on insulator (SOI) wafer with a 220 nm top silicon layer and a 3 μm thick buried oxide. We choose hydrogen silsesquioxane (HSQ) e-beam resist, rather than the PMMA that is used for fabricating the microrings, as it has even higher resolution. The HSQ is coated on the wafer and pre-baked for 5 minutes at 180 ℃. The patterns are exposed using electron beam lithography with an acceleration voltage of 100 kV (Elionix ELS-7000). After developing the chip using 25% tetramethylammonium hydroxide (TMAH) for 1 minute, the patterns are transferred to the top Si layer by dry etching using hydrogen bromide (HBr). The remaining HSQ e-beam resist is removed by dipping the sample into a 7:1 buffered oxide etchant (BOE) solution for 20 sec. The etching rate of HSQ in the BOE solution is much higher than that of the buried oxide, meaning that the undercut of the waveguide is minimal. A PDMS chip containing microfluidic channels (50 μm high, 100 μm wide) is bonded to the SOI chip.

Our device consists of a photonic crystal cavity coupled to a bus waveguide (Figure 4-7 [17],

[54]). The bus waveguide could be used to trap the particles and deliver them to the photonic crystal cavity, reducing the time between photonic crystal trapping events. The photonic crystal cavity is fabricated on a waveguide section and the incident light is coupled to it from a bus waveguide parallel to it with the same dimensions. The coupling coefficient can be tuned to achieve critical coupling by adjusting the distance between the photonic crystal and the bus waveguide. Our experiments reveal that a 200 nm gap represents an optimal value for coupling.

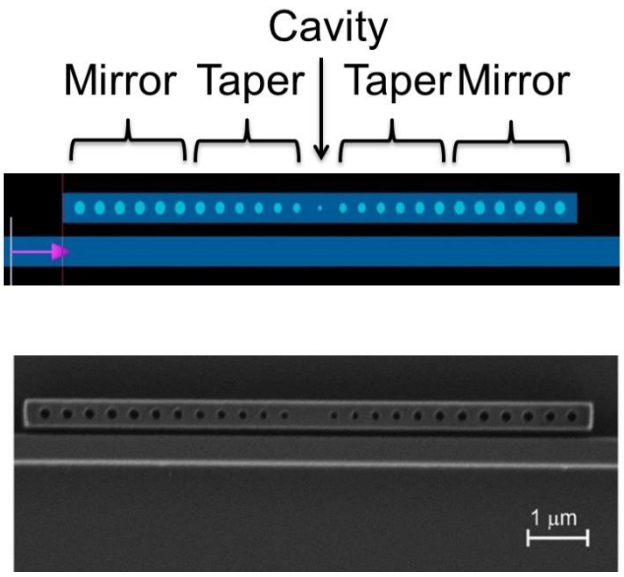


**Figure 4-7 Top: Design of the waveguide coupled 1D photonic crystal cavity with taper regions and a nanoslot in the center; Bottom: SEM image of the photonic crystal cavity fabricated. The nanoslot is not incorporated in the fabricated device shown in the bottom image.**

We measured the transmission spectra of devices both with and without a nanoslot. There is no significant Q deterioration observed after incorporating the nanoslot; this is also consistent with the simulation results in section 4.1.4. Figure 4-8(a) shows a transmission spectrum of a 1D

photonic crystal cavity with taper sections and a nanoslot in the center. The $Q$ is measured to be 2000 by fitting the transmission spectrum with a Lorentzian function, matching the predictions of simulations. Another advantage of the waveguide-coupled approach is that it permits multiple cavities to be integrated onto on the same waveguide, since the off-resonance cavities would not affect the light propagating along the bus waveguide. Figure 4-8(b) shows a transmission spectrum of a structure with three photonic crystal cavities coupled with the same waveguide. We design the cavity lengths to different slightly from one another, so that the resonance wavelengths are separated by ~10 nm. This would permit the particle buffering method demonstrated with microrings in Chapter 3, in which particles are trapped and released by caivities by appropriate tuning of the laser wavelength.

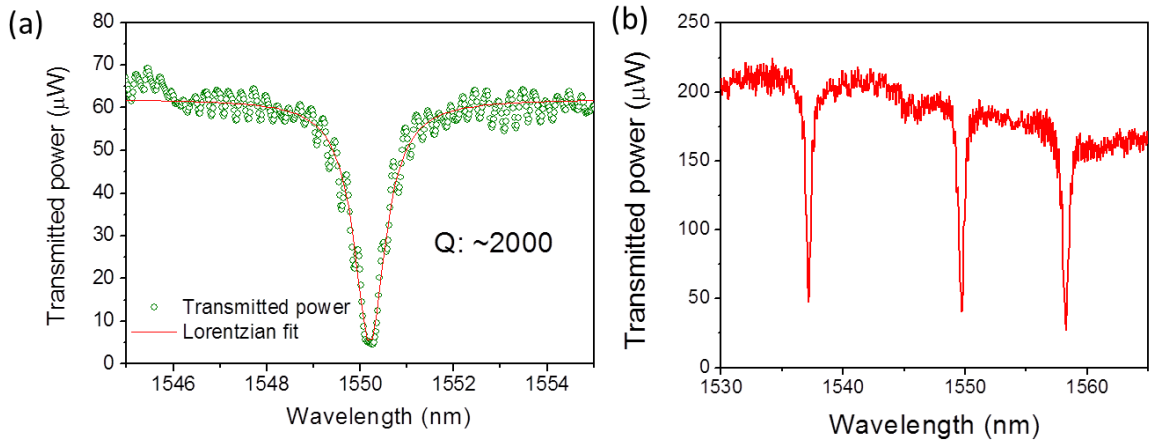


**Figure 4-8 (a) Transmission spectrum of a 1D photonic crystal cavity with tapered sections and a nanoslot in the center. (b) Transmission spectrum of device with multiple photonic crystal cavities coupled to the same waveguide. Etch cavity has a slightly different length. All the measurements are performed using a TE mode.**

### *4.2.2 Optical trapping demonstration*

The photonic crystal cavities are designed to be excited by TE mode light in the input waveguide. The input to the chip is chosen to excite TE (50% power) and TM (50% power) modes in the waveguide. This mixture of mode types has favorable properties. The TM mode portion of the trapping light helps pull the particles onto the waveguide and propel them along it, since the TM mode generates a larger optical force. The TE mode couples to the photonic crystal microcavity, enabling particles to be trapped by it (Figure 4-9). The bus waveguide works as a particle collector providing a large collecting area, and the particles are delivered along the waveguide to the cavity. Since the optical field intensity in the cavity is much higher than that of the bus waveguide, the particles in the coupling region are pulled to the cavity. In addition to enabling rapid trapping, the hybrid mode trapping approach also makes it possible to switch the trapped particle back to the waveguide by tuning the polarization of the trapping laser to be purely TM mode.

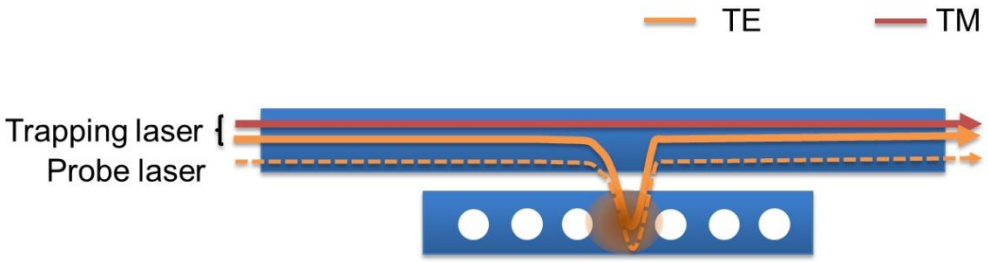


**Figure 4-9 Schematic diagram of the hybrid mode trapping using 1D photonic crystal cavity. The trapping laser input is chosen to excite TE (50%) and TM (50%) modes in the waveguide.**

Using this approach, we trap polystyrene particles with diameters from 110 nm to 2 μm. We

furthermore trap silver nanoparticles. Supplementary movie 4-1 shows polystyrene particles with diameters of 320 nm being trapped by the waveguide and propelled along it to the photonic crystal cavity, where they are then trapped by it. To reduce the light absorption by the water and prevent convection due to heating, a 1D photonic crystal cavity without the nanoslot is used in this measurement. As discussed previously, the nanoslot design presents the possibility for very high performance optical trapping, but is likely to be most effective at wavelengths for which the optical absorption by water is lower than it is at λ=1550 nm. A combination of TE (2.5 mW) and TM (2.5 mW) modes is employed at the beginning of the movie, to enable the particle to be trapped by the waveguide and propelled along it to the 1D photonic crystal cavity. The particle is pulled to the cavity by the high field intensity of TE mode in the cavity. The trapped particle is switched back to the bus waveguide after setting the laser input to the device so that the mode in the waveguide is purely TM at $t$ = 6 s. We also show that the same device can trap silver nanoparticles with diameter of 80 nm. The particle induced resonance shift can be used to monitor and detect the trapped particles in real-time. More details on this point are included in Chapter6.

### 4.3 Summary

Due to their small mode volumes, photonic crystal cavities provide high field enhancement and large optical forces. The standing wave nature of the resonances of photonic crystal cavities enables particles to be trapped about fixed positions, rather than continually circulating as they

do with microrings. We have designed a 1D photonic crystal cavity with high performance for trapping by integrating taper sections and a nanoslot in the center of the cavity. The simulation results show that the designed structure could provide a 1300 times gradient force enhancement compared to a normal straight waveguide. We experimentally demonstrate optical trapping using a 1D photonic crystal cavity. Using a combination of TE and TM modes, we trap nanoparticles on the input waveguide and deliver them to the cavity. We successfully trap polystyrene particles with diameters from 110 nm to 2 μm, and silver particles with diameters of 80 nm. Further enhancement of the optical force for smaller particles should be possible by optimizing the design.

# Chapter 5 Passive particle sorting

Particle sorting plays an important role in medical diagnosis and the environmental sciences. In this chapter, we demonstrate an integrated particle sorting device based on the near-field optical forces exerted by a 3-dB optical power splitter that consists of a slot waveguide and a conventional channel waveguide. A mixture of 320 nm and 2 μm polystyrene particles brought into the splitter are sorted so that they exit along the slot waveguide and channel waveguide, respectively. Electromagnetic simulations and precise position tracking experiments are carried out to investigate the sorting mechanism. This label-free passive particle sorting device requires low guided power (20 mW in these experiments), and provides a new technique for sorting sub-micron particles.

## 5.1 Introduction to particle sorting

Conventional large-scale sorting systems such as fluorescence-activated cell sorters (FACS) [78] have been developed and commercially available for decades. Alternative microfluidic-based lab-on-a-chip approaches have also attracted much attention due to their small sample and reagent consumption, high efficiency and low cost [79]. More importantly, multiple functionalities such as sample preparation, chemical analysis, bio-analysis or other assays of the sorted populations can be integrated on the same chip.

Various microfluidic based sorting devices have been demonstrated using the electrokinetic mobilization of fluid [79], dielectrophoretic forces [80], and hydrodynamic flow control [81]. However, these techniques can suffer from problems that include electrophoretic damage due to high voltages, the requirement for the buffer having particular attributes, and the need for fluorescent labeling for active sorting to function. A passive particle sorting based on intrinsic properties such as size and refractive index could be useful in many applications due to the simplicity of the system and sample preparation.

Optical forces have been used for particle manipulation due to their non-invasive and non-contaminating nature. Our group has investigated optical manipulations on various platforms including diffractive optics, plasmonics, and Si photonics [13], [82], [83]. Several optical force based particle sorting devices by other groups have been reported [47], [69], [84]. Particles with different sizes, shapes and refractive indexes experience different optical forces and can be separated into output channels based on their intrinsic properties without fluorescent labeling [37], [85]. However, a displacement of several microns is often needed to deliver particles into different microfluidic outlets. This requires a large incident power for optical force to push or drag the particles for such a long distance, which is especially difficult for sub-micron particles.

Here, we demonstrate a passive sorting system using the near-field optical forces exerted by a waveguide-based optical splitter. Because waveguides are employed, the light input to the device can interact with the particles over a long distance, as the mode maintains its profile and does not

spread as it would for a laser beam in free space. The trapped particles can therefore be delivered over long distances with relatively low power consumption. More importantly, particles are sorted into different waveguides, rather than into different microfluidic channels. A displacement on the order of $\lambda/2$ is therefore needed, one or two order of magnitude smaller than previous microfluidic based sorting devices, which sort particles into different outlet channels [85], [86]. Therefore, a lower power is required to switch the particles, which opens up new opportunities for sorting sub-micron particles. The planar nature of the system makes it possible to implement massive parallel processing and integrate other pre- or post-sorting functionalities into the system.

## 5.2 Device design and fabrication

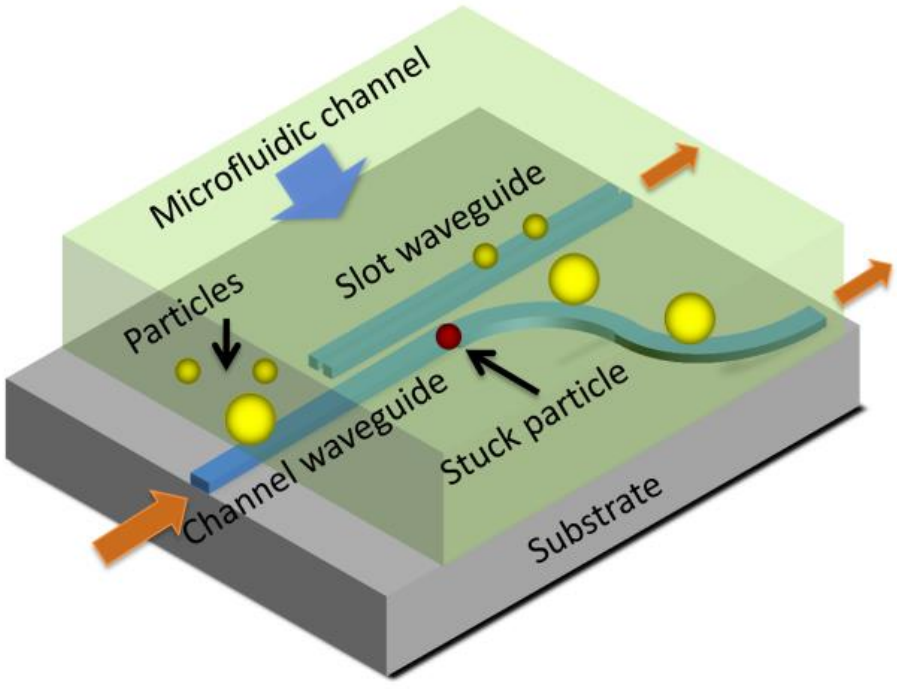


**Figure 5-1 Schematic diagram of proposed microparticle sorting device**

Figure 5-1 shows the schematic diagram of our sorting system. The sorting is performed using a 3-dB optical splitter consisting of a channel waveguide (CWG) and a slot waveguide (SWG). We have reported a compact polarization splitter using a similar structure [87]. The transverse magnetic (TM) mode incident from the CWG is split equally into the two splitter outlets. The splitter is embedded in a PDMS microfluidic channel oriented perpendicular to the waveguides. Fluorescent polystyrene particles are delivered to the device through the microfluidic channel and trapped by the gradient force associated with the evanescent field of the waveguides when they come into their vicinities. The trapped particles are pushed along the waveguide by the scattering force and delivered to the coupling region. There, the smaller particles are switched to the SWG with the help of an obstacle (a stuck particle), while the larger particles remain on the CWG. As discussed in Section 5.4, this is due to the different potential wells experienced by the large and small particles. The stuck particle in red plays a critical role for transferring the small particles. Further details are discussed in section 5.4.

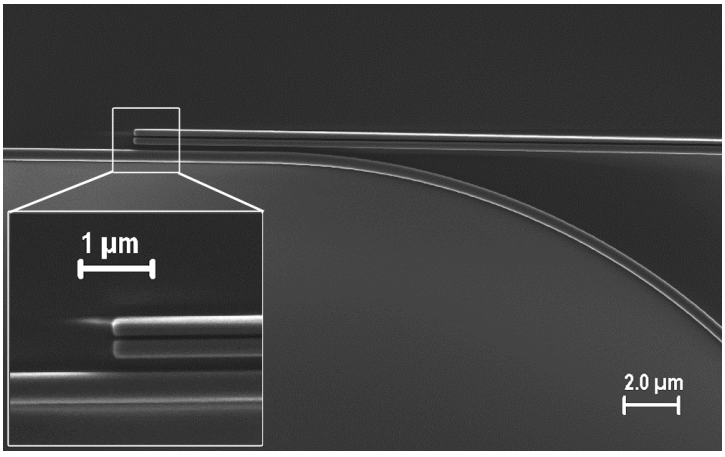


**Figure 5-2 SEM image of the 3-dB splitter; the inset shows an enlarged image of the coupling region.**

The device is fabricated on a silicon on insulator (SOI) wafer with a 220 nm top silicon layer and a 3 μm thick buried oxide. The fabrication process is described in section 4.2. Figure 5-2 shows a scanning electron microscope top view image of the fabricated device comprising a CWG and an SWG. The inset shows a magnified image of the coupling region. The CWG has a width of 420 nm. The SWG is 450 nm wide and has a 50 nm nanoslot in its center. The coupling coefficient depends on the size of the gap and the length of the coupling region. We choose a gap of 200 nm and a coupling length of 4.6 μm to achieve a 3 dB splitting of the TM mode. Fiber couplers consisting of silicon inverse tapers embedded in 2 x 2 μm SU8 waveguides are employed at both ends of the waveguides to improve the coupling with the lensed fiber that delivers the laser input and to reduce the Fabry-Perot effect by lowering the reflection from the device output. The chip is placed in an experimental set-up for sorting demonstrations. The output of a tunable laser (HP8168, near $\lambda$ = 1550 nm) is amplified by a high power C-band erbium-doped fiber amplifier (EDFA) and launched into the waveguide to excite TM modes. The output from the device is collected by a lens onto a photodetector. A homebuilt upright fluorescence microscope equipped with a CCD camera is used to monitor the particle sorting process.

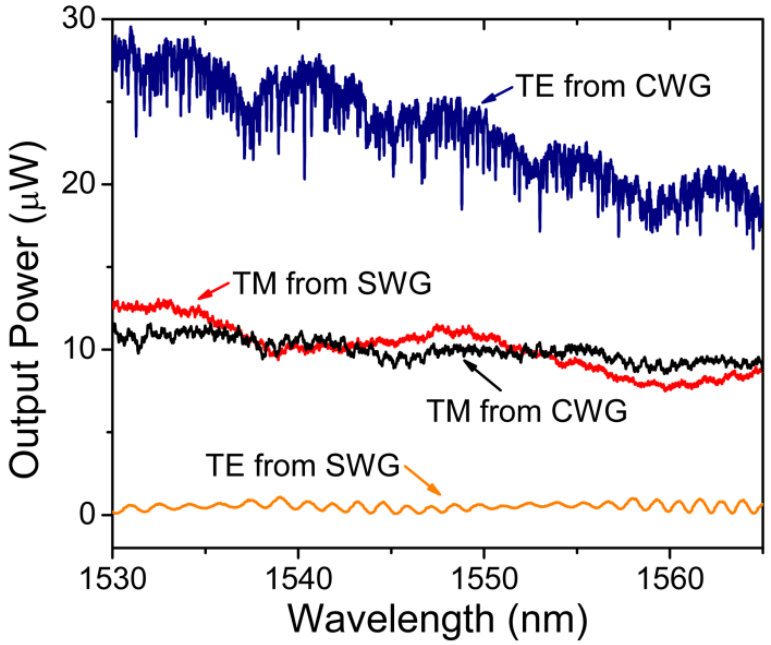


**Figure 5-3 Output power (μW) vs wavelength (nm) from SWG and CWG when input to device is TE mode (orange and blue curves) and when it is TM mode (red and black curves).**

Figure 5-3 shows the transmission spectra of the device from both outputs of the splitter using the fiber end-fire technique. Our design gives a $3 \pm 0.2$ dB splitting of the TM mode across the entire C-band from 1530-1565 nm. A wavelength of 1550 nm is used in our sorting demonstration. Figure 5-3 shows that, at this wavelength, the power coupled into the SWG is 7% higher than the power remaining in the CWG.

### 5.3 Particle sorting measurement

We experimentally demonstrate the passive sorting of particles with diameters of 320 nm and 2

μm using the optical splitter. Particles are mixed together in de-ionized (DI) water and injected into the microfluidic channel using a syringe. The behavior of particles encountering the splitter is captured by the fluorescence microscope and included as the Supplemental Movie 5-1. Figure 5-4 shows selected frames taken from this movie. Both the large and small particles are observed to be pulled onto the CWG by the optical gradient force and propelled to the coupling region by the scattering force. A long section of the CWG before the splitter is situated inside the microfluidic channel, which increases the probability that it captures particles. Over the course of the movie, all of the smaller particles that are trapped by the CWG are switched to the SWG by the splitter, while all of the larger particles remain on the CWG. The smaller particles are switched to the SWG after bouncing off an obstacle particle (320 nm diameter) stuck on the CWG in the coupling region (indicated in the second frame of Figure 5-4). The stuck particle provides a perturbation that allows small particles to be ejected from the CWG potential well and be trapped in the SWG potential well. The sorting mechanism is further discussed in Section 5.4. All particles are correctly sorted during the observation period of more than 10 minutes. A sorting rate of ~30 particles/min is observed, which can be improved by increasing the density and speed of trapped particles on the waveguide. Parallel processing by integrating multiple channels could further boost the sorting rate.

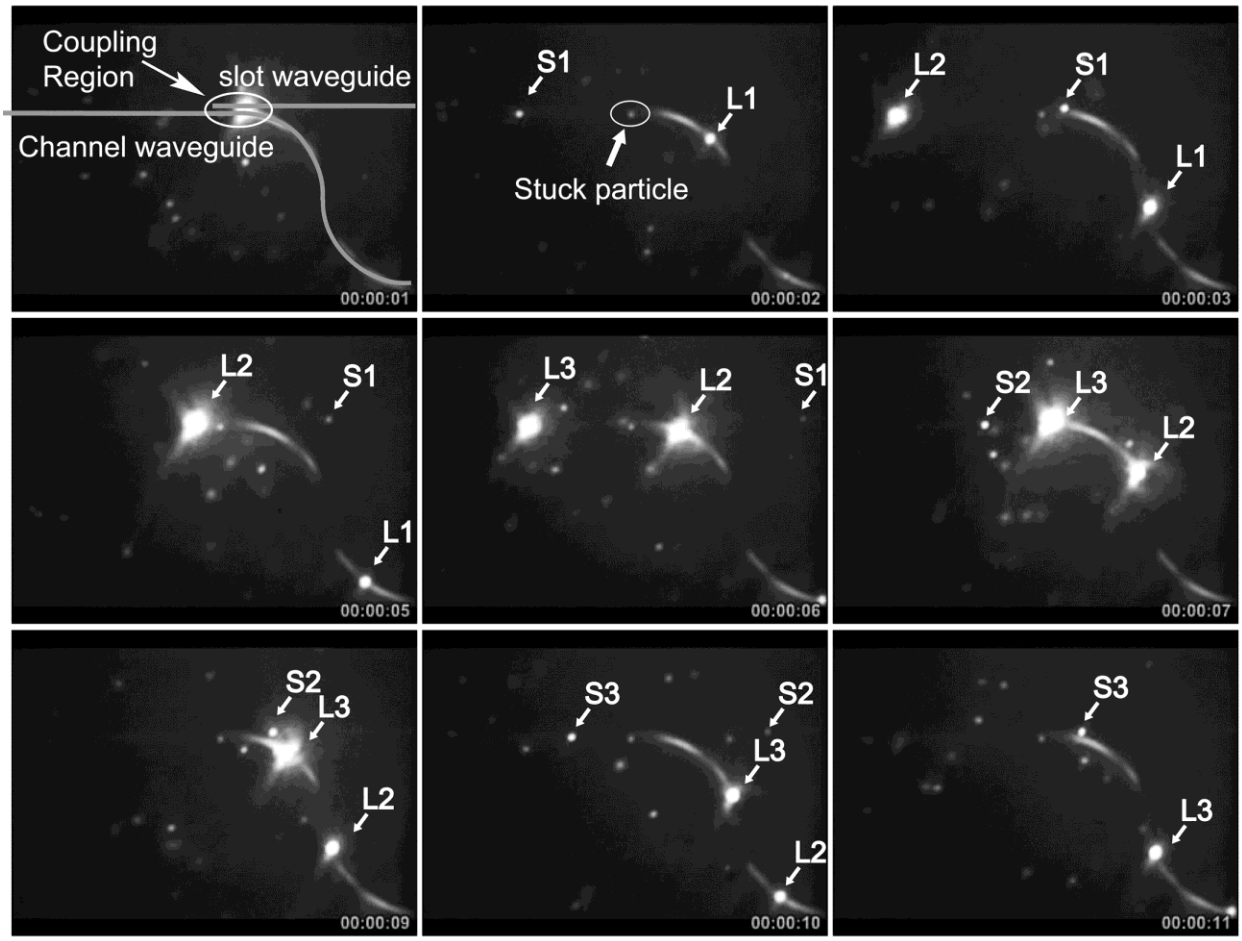


**Figure 5-4 CCD image of the sorting with a guided power of 20 mW. The waveguides are indicated by the gray lines in the first frame. The trapped particles are marked by white arrows with the indicators S and L for the 320 nm and 2 μm particles, respectively. The obstacle particle is marked in the second frame.**

The guided power in the channel waveguide incident to the device is estimated to be 20 mW. This is one to two orders-of-magnitude smaller than the optical powers used in some previous optical sorting approaches [37], [69], [85], [86]. The laser power is roughly ten times larger than the guided power due to coupling losses. It has been shown, however, that such losses can be

reduced considerably [88]. It should therefore be possible for the approach we introduce to employ both laser and guided powers that are far smaller than previous methods.

### 5.4 Mechanism of the sorting phenomenon

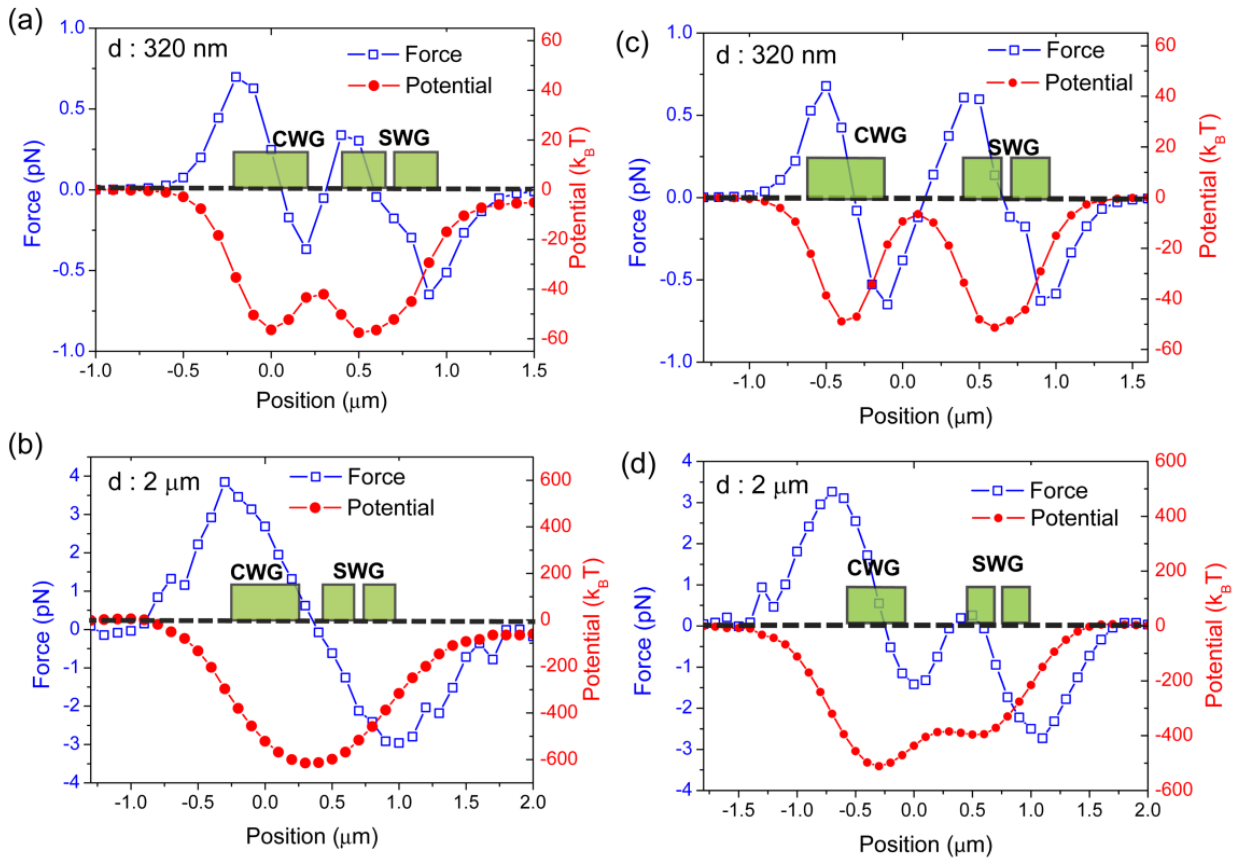


**Figure 5-5. In-plane gradient forces (Fy) and potential depth plotted as a function of particle position for (a) 320 nm and (b) 2 μm particles at start of bending region. Similarly, Fy and potential depth are plotted for (c) 320 nm and (d) 2 μm particles at distance of 7 μm from start of bending region. Optical forces are calculated by Maxwell stress tensor method using fields found from 3D FDTD simulations. To indicate the positions of the waveguides, the cross sections of the CWG and SWG are shown in (a)-(d). The guided power in the incident waveguide is taken as 20 mW.**

To investigate the mechanism by which particles can be switched, we simulate the gradient force along the $y$-direction ($F_y$) as a function of particle position, also along the $y$-direction. We do not know the precise value of the gap between the particles and the waveguide surface, but make the same approximation as that of previous work [83], and take it to be 30 nm, slightly larger than the Debye length. The particles are situated at the start of the bending region of the CWG. We assume a total guided power of 20 mW in the incident waveguide. Trapping potentials are calculated by integrating force with distance along the $y$-axis. We take the potential at 2 μm from the center of the structure to be zero. Calculation results are plotted in Figure 5-5(a) and (b) for 320 nm and 2 μm particles, respectively. Figure 5-5(a) shows that a double-well distribution with two minima, each around the waveguide centers, occurs for the smaller particles (320 nm diameter). On the other hand, as shown in Figure 5-5(b), there is only one minimum located at roughly the midpoint of the two waveguides for the larger particles (2 μm diameter). We believe that the dramatic differences between the potential vs distance curves play an important role of the sorting. For example, if the stuck bead causes one of the 320 nm particles to be displaced by some means to a $y$-position greater than ~250 nm (see Figure 5-5(a)), it will become trapped on the SWG. On the other hand, it is entirely possible that the stuck bead has no effect on the delivery route of 2 μm particles because only one potential minimum exists for them. In the bending region, the distance between CWG and SWG increases. This modifies the potential wells. We simulate the gradient force and the potential depth along the $y$-direction when particles are located 7 μm after the start of the bending region as in Figure 5-5(c) and (d). The

further splitting of two potential wells for 320 nm particles prevents the particles jumping back to the CWG. From Figure 5-5(d), it can be seen that the potential well experienced by 2 μm particles splits as the gap between the waveguides enlarges. The CWG exerts a larger force on the particles than the SWG, and provide a deeper potential well (Figure 5-5(d)). The 2 μm particles fall into the deeper well and follow the CWG when it departs from the SWG.

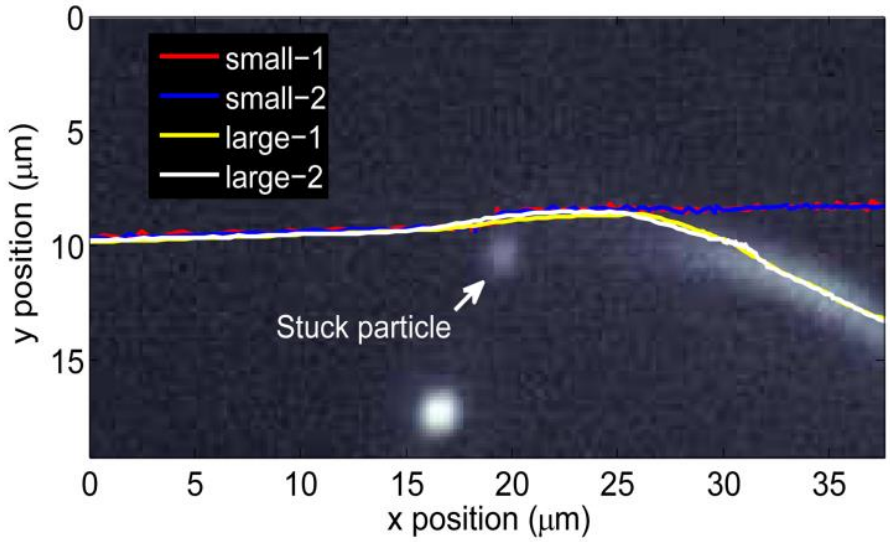


**Figure 5-6. Traces of two small and two large particles passing through the coupling region. The positions are tracked using center of mass analysis of each frame of the Supplemental Movie. The stuck particle is indicated by an arrow.**

To confirm this mechanism, we analyze the trajectories of particles that traverse the coupling region and encounter the stuck bead. The analysis is performed on the Supplemental Movie 5-1, by finding the center-of-mass of the particles in each movie frame. The results are presented in Figure 5-6 for two small and two large particles. The trajectories of these particles are shown as colored lines overlaid on one frame of movie. The stuck particle is indicated by a white arrow.

The traces of small particles show that they move from the CWG to the SWG at around the position of the stuck bead. After that, these particles are move along the SWG, and do not return to the CWG. This behavior is consistent with the double potential well discussed previously. For larger particles, the traces shift to positions between two waveguides near the stuck particle, which is also consistent with the potential distribution in Figure 5-5(b). These particles follow the CWG as the two waveguides split at a position of ~7 μm to the right of the stuck particle, which is again consistent the deeper potential well on the CWG simulated in Figure 5-5(d). The results of the particle tracking analysis are therefore consistent with the particle sorting phenomenon suggested by the analysis of simulations.

As this is a first generation device, there are still many ways of improving the performance. The size of the gap between the CWG and SWG determines the upper limit on the size of the particles experiencing a double well potential. Therefore, engineering the gap size can be used to control the size threshold of the sorting process. Particles with a smaller size than this threshold could be separated from larger particles. A multilevel sorting system providing a higher size resolution could be achieved by cascading several sorting units with different size thresholds. Switching of the smaller particles requires the perturbing obstacle within the coupling region, which comprises a stuck particle in our demonstration. However, more robust alternatives could be applied; for example, Si nanoparticles fabricated by e-beam lithography and etching, or even features formed in resist by photo- or electron-beam lithography. The planar nature of this waveguide based sorting device could enable it to be integrated with other waveguide-based

optofluidic devices to provide pre- or post-sorting functionalities such as buffering and sensing.

### 5.5 Summary

We demonstrate a novel sorting device based on near-field optical forces using a waveguide-based 3-dB optical splitter. In the fabricated device, 3-dB splitting of the TM mode incident light is achieved *via* careful engineering of the coupling length. After injecting DI water containing 320 nm and 2 μm polystyrene particles to the microfluidic channel, particles are pulled onto the CWG by optical gradient forces, and propelled to the splitter by optical scattering forces, where they encounter a perturbation comprising a stuck bead. The 2 μm particles continue to be propelled along the CWG after leaving the splitter, while the 320 nm particles are transferred to the SWG. Optical force calculations based on the Maxwell stress tensor are performed to understand the sorting mechanism. In the coupling region, the smaller particles experience a double-well trapping potential. A structural perturbation can switch them from the CWG to the SWG, while the larger particles, experiencing a single potential well, are not affected by the perturbation. In the bending region, the larger particles follow the CWG, as its potential well is deeper. Position tracking analysis of particles passing through the device also provides evidence for this sorting mechanism. The planar nature of this waveguide based sorting device makes it easy to implement massive parallel processing and integrate other pre- or post-sorting functionalities into the system. Given its passive nature and ability to sort sub-micron particles, we believe that the all-optical sorting mechanism we introduce could lead

to a variety of lab-on-a-chip applications in the life sciences, medical diagnosis and the environmental sciences.

# Chapter 6 Trapping-assisted particle sensing

An improved ability to sense particles and biological molecules is crucial for continued progress in applications ranging from medical diagnostics to environmental monitoring to basic research. Impressive electronic and photonic devices have been developed to this end. However, several drawbacks exist. The sensing of molecules is almost exclusively performed *via* their binding to a functionalized device surface. This means that the devices are seldom re-usable, that their functionalization needs to be decided before use, and that they face the diffusion bottleneck. The latter challenge also applies to particle detection using photonic devices. In this chapter, we develop a trapping-assisted sensing technique to solve the problems mentioned above. We demonstrate particle sensing using optical forces to trap and align them on waveguide-coupled silicon microcavities. Because there is no chemical or biological binding to the device itself, there is the possibility that it can be reused. We demonstrate this capability using a measurement system incorporating two lasers. The first laser is used to trap particles, while the second laser is used to monitor the cavity resonance, thereby enabling trapped particles to be detected.

## 6.1 Introduction to particle sensing using microcavities

The resonance shifts induced by particles that attach to the surfaces of optical microcavities have been explored for high sensitivity detection. Stand-alone high-Q cavities such as

microspheres[29] and microtoroids[27, 61, 87] have been used to detect biological objects and microparticles. Compared with traditional fluorescence-based biological sensing, the microcavity approach offers ultra-high sensitivity and a label-free nature.

While impressive results have been obtained, microcavity sensing currently faces a number of obstacles. Typical microcavity sensing experiments involve the analyte binding to [29], or being physically adsorbed by [90], the microcavity surface. These methods introduce additional processes to attach and remove the analyte such as functionalizing the surface, immobilizing antibodies, and chemical or laser cleaning, thereby reducing sensing speed and increasing cost. Meanwhile, the resonance shift depends on the position of the analyte within the cavity mode, which is especially problematic if the analyte consists of a discrete entity such as a nanoparticle. The lack of position control in current analyte loading methods makes the quantitative interpretation of experimental data therefore problematic.

To solve these problems, we integrate trapping and sensing on the same chip to provide a reusable system for real time microparticle sensing. Optical trapping provides an effective way to load and release targeted particles, and improves the reproducibility since the particles are self-aligned with the field maxima. The optical force also helps drag the particles to the surface and reduces the diffusion time and thereby improves the sensing speed.

The trapped particles introduce a resonance shift of the microrings, and the shift depends on the

properties of the trapped particles, including their number, size, position and refractive index. For the polystyrene particles employed in our experiments, trapping induces resonance redshifts due to the particles having refractive indices higher than that of the surrounding water. Similarly, with a fixed laser wavelength, the transmitted signal intensity from the output waveguide also changes as particles are trapped, a phenomenon that can be used to obtain, in real time, information about trapped particles.

## 6.2 Demonstration of microring sensing

### *6.2.1 Bulk refractive index sensing*

The microring cavity with a radius of 10 μm is used to detect the bulk refractive index of water containing ethanol at different concentrations. The ethanol is mixed with deionized water to achieve different concentration from 10% to 50% in volume. The samples are injected into the microfluidic channel, and the resonance shift of the microring cavity is measured *in situ.* Figure 6-1(a) shows the measured transmission spectra of the microring with different concentration ethanol solutions. Figure 6-1(b) plots the resonance wavelength as a function of the ethanol concentration in volume. The detection sensitivity of TE mode is calculated to be 116 nm/RIU using the reported refractive index of the ethanol-water mixture [91]. Similarly, the sensitivity for TM mode is measured to be 595 nm/RIU. The sensitivity is 5 fold larger than that of the TE mode, due to its field being less confined to the core, with a greater fraction of the mode power being in the cladding that consists of the ethanol-water solution. It is for this reason

that the TM mode is used for the particle sensing measurements.

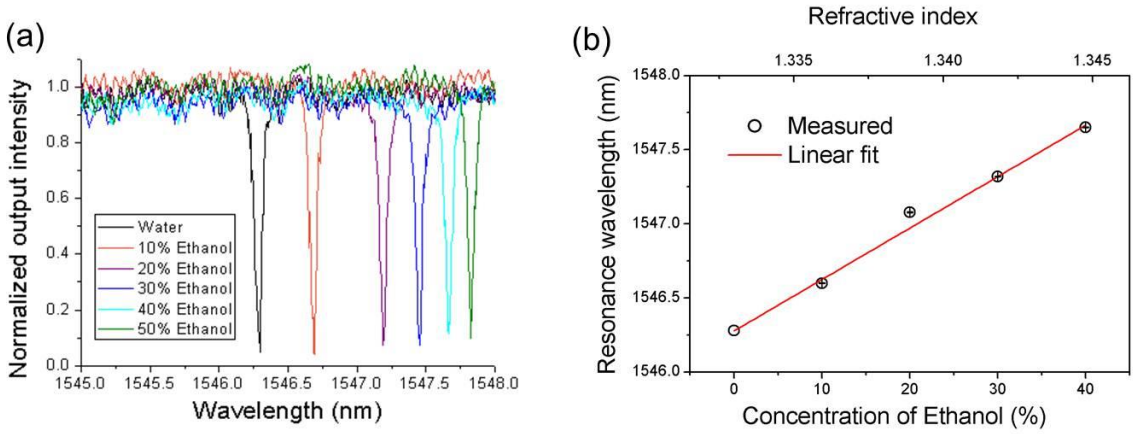


**Figure 6-1 (a) Transmission spectra of the microring measured for different concentrations of ethanol-water mixture, (b) Resonance wavelength as a function of the concentration of ethanol.**

### *6.2.2 Microring particle monitoring*

We first demonstrate the trapping and sensing of polystyrene particles with a microring resonator. The incident light is set to the resonance frequency of the cavity, and the power intensity from the output waveguide is monitored using a photodetector. In Figure 6-2(a), the output power as a function of time is shown as particles with diameter of 1.1 μm are successively trapped. The guided power in the waveguide at time *t=0* is 5 mW, with the laser wavelength being set to the microring resonance (1545.1 nm). Each of the steps in transmitted power, at *t=11s*, *20s* and *30s*, results from an additional particle being trapped, as verified by observing the CCD image. By monitoring the intensity of the output signal, particles can be counted as they are trapped, a useful function for applications in which we want to store particles on microring buffers. Figure

6-2(b) shows, in enlarged detail, the signal (transmitted power vs. time) occurring while a single particle is trapped on the ring. As we describe further below, this is due to the circulating particle motion.

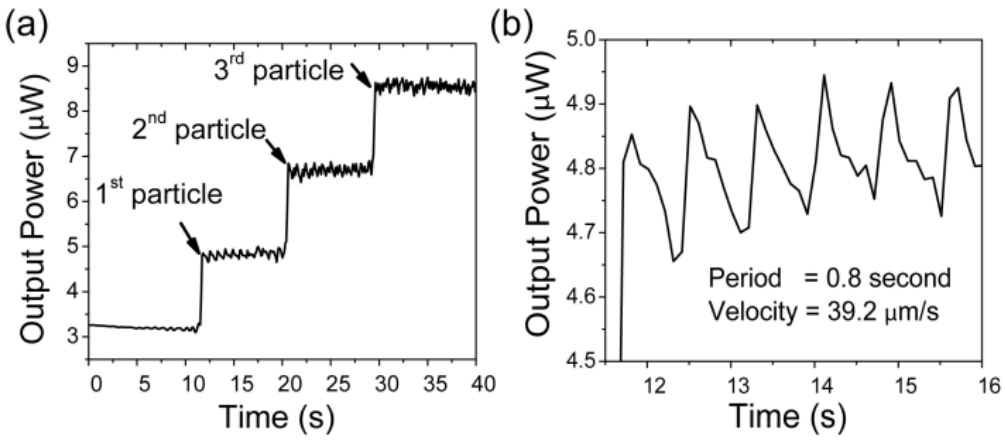


**Figure 6-2 (a) Output power as a function of time as particles are trapped; (b) Output power as a function of time, shown in enlarged detail. A single particle is trapped on the microring. A particle velocity of 39.2 μm/s is calculated from the period of the signal (0.8s).**

The circular motion of the particle on the ring gives rise to a periodic change of the output power. The intensity maxima occur when the particle is located in the coupling region near the bus waveguide. We believe that the attenuation of the field intensity along the ring is the main reason for the oscillation of the output power. Non-negligible radiation loss, which is partly responsible for the modest quality factor of the cavity, reduces the intensity of the fields as they propagate around the ring. Therefore, the optical force reduces from a maximum at the coupling region to a minimum when the particle is located at a position on the microring just before it returns back to

the coupling region. We carry out calculations of the force on the particle at different positions on the ring using the Maxwell stress tensor method based on field distributions determined from finite difference time domain (FDTD) simulations. These calculations show that the component of the force that pulls the particle to the ring is ~25% smaller when the particle is at the position on the microring just before it returns to the coupling region, compared to when it is at the coupling region. It can be expected that this reduced force should lead to a larger gap between the particles and ring surface, thereby resulting in a smaller resonance shift and a larger output power. The velocity of the trapped particle can be calculated by: $v = 2\pi r/\tau$, where $r$ is the ring radius and $\tau$ is the period of the optical power signal, equal to the particle circling period. The measured velocity is 39.2 μm/s for single particle trapping. Similarly, when two particles are trapped, a velocity of 34.8 μm/s is measured, which is smaller than that of single particle trapping. This can be understood as follows. When two particles are trapped, the larger resonance shift leads to lower field intensity in the microring.

### 6.3 Two-laser system for trapping and sensing

We demonstrate trapping and sensing using a microdonut and a 1D photonic crystal cavity. The experimental setup makes use of two tunable lasers, each operating around 1550 nm, to perform the trapping and sensing functions separately.

### *6.3.1 Two-laser measurement setup*

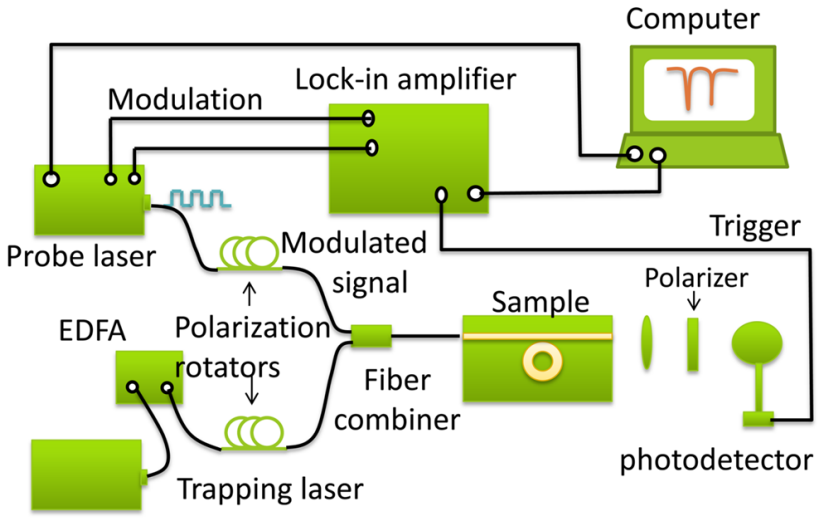


**Figure 6-3 Schematic diagram of measurement setup.**

Figure 6-3 shows a schematic diagram of the two-laser measurement setup. The trapping laser output is amplified by an erbium-doped fiber amplifier (EDFA) to achieve a high output power, passes through a polarization rotator, and is then input to a fiber combiner. The probe laser output passes through a polarization rotator, and is then also input to the fiber combiner. The fiber combiner output is focused into the photonic chip. The output of the photonic chip is focused onto a photodetector by a lens, with a polarizer used to select whether measurements are made on the TE or TM mode. The probe laser is modulated, with the modulation signal provided by a lock-in amplifier. This ensures that the probe laser component can be extracted from the photodetector signal using a lock-in amplifier. Two polarization rotators are used to control the polarization of the trapping and probe lasers independently. Therefore, it is possible to set different polarization for the trapping and probe laser to meet the need for different

measurements. A homebuilt fluorescence microscope (not shown) is used to monitor fluorescent particles in the cavity vicinity.

### *6.3.2 Device design and preparation*

The microdonut and 1D photonic crystal cavity are fabricated on a silicon-on-insulator (SOI) wafer. Figure 6-4(a) and (c) show SEM images of the fabricated devices. The fabrication process is discussed in section 4.4. For particle sensing experiments, fluorescent polystyrene particles in water are delivered to the microcavities through the microfluidic channel.

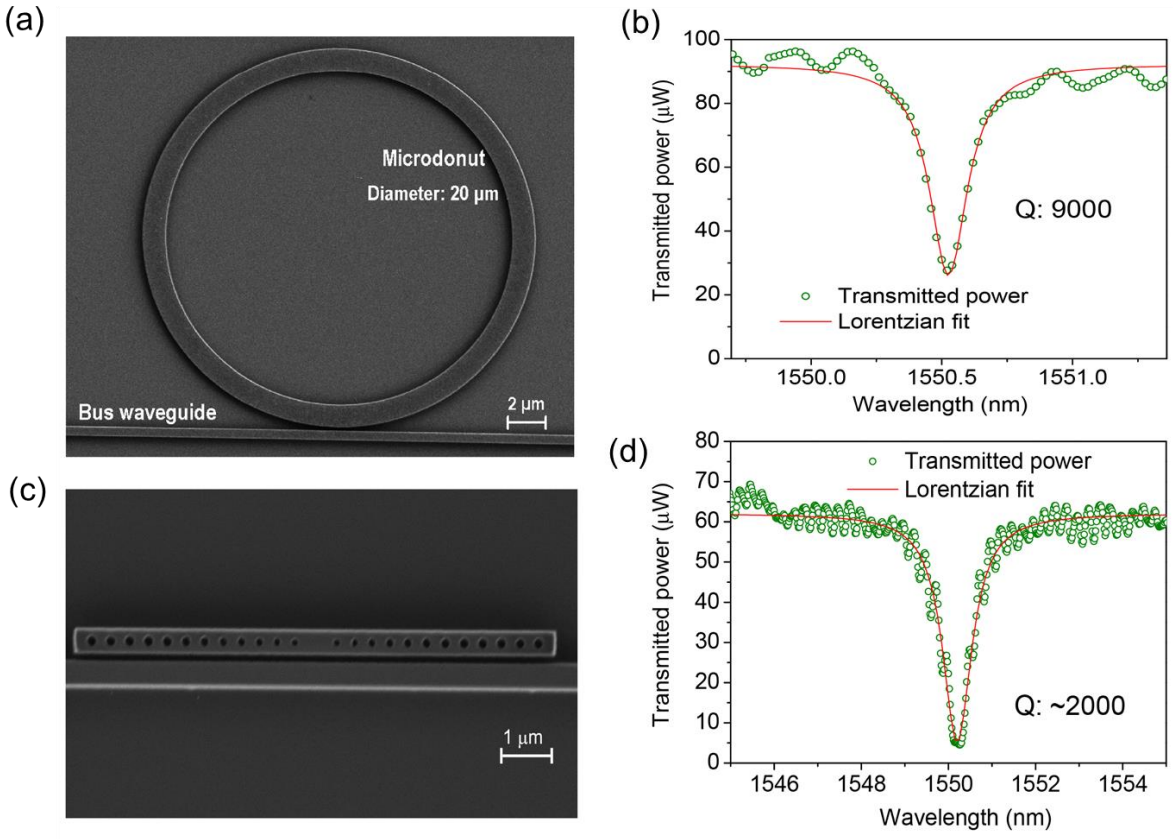


**Figure 6-4 (a) SEM image and (b) transmission spectrum of microdonut, (c) SEM image and (d) transmission spectrum of 1D photonic crystal cavity.**

The microdonut has an outer radius of 10 μm and width of 1 μm. A bus waveguide with a width of 500 nm is used to couple light into the microdonut. The gap between the microdonut and the bus waveguide is 200 nm. The microdonut has a Q of ~9000 for the transverse magnetic (TM) mode at the wavelength of 1550.5 nm as shown in Figure 6-4(b). The transmission spectrum is measured in water. The photonic crystal cavity has a similar design to the devices in Chapter 4. The device is fabricated by etching periodic holes into a Si channel waveguide. The holes are shifted outward to form a cavity in the center. The tapered regions, in which the hole sizes gradually increase from the center, are used to reduce the scattering loss of the cavity mode and improve the Q. The cavity is coupled to a bus waveguide with a gap of 200 nm between them. Both the photonic crystal cavity and the bus waveguide have a width of 450 nm. The transmission spectrum of Figure 6-4(d) shows that a Q of ~2000 is measured for the transverse electric (TE) mode of photonic crystal cavity.

### *6.3.3 Real-time monitoring of trapped particles*

Real-time monitoring of trapped particles by measuring the resonance frequency shift *in situ* is demonstrated in Supplementary Movie 6-1. This shows a typical particle trapping and sensing experiment. The measurement interface is implemented using the software LabView (http://www.ni.com/labview), enabling viewing in real-time of the fluorescence microscopy image of the particles in the resonator vicinity, the resonator transmission spectrum, and the

resonance wavelength as a function of time (measured since the start of the experiment).

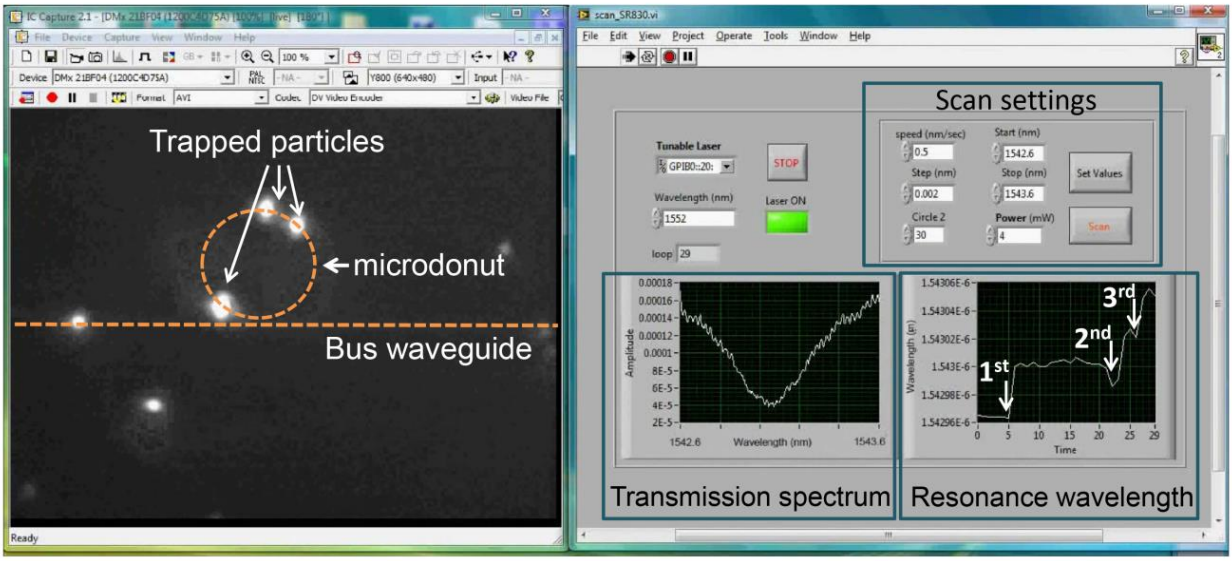


**Figure 6-5 Sensing particles in real time. Screenshot during obtained during an experiment involving the trapping of 2 μm diameter particles. Left: top view of device obtained with homebuilt fluorescence microscope; bright spots are particles emitting fluorescent light. Right: measurement interface (left chart: transmission spectrum, right chart: resonance wavelength vs time).**

During the experiment, the trapping laser is set to the resonance wavelength of the microdonut (1550.5 nm) to provide a high field enhancement in the microdonut. The probe laser is continuously scanned about this resonance wavelength in a typical bandwidth of 1 nm, at a rate of 0.5 nm/s. This enables the microdonut transmission spectrum, and from this the resonance wavelength, to be found every 2 s. The measurement interface is shown for an experiment for which several 2 μm polystyrene particles are trapped. Prominent steps in the resonance wavelength vs time plot are seen with the trapping of each additional particle. Figure 6-5 shows a screenshot of the measurement interface from the Supplementary Movie 6-1. The left side

displays the image of the cavity (here a microdonut) obtained with the homebuilt fluorescence microscope that is part of the measurement set-up. The white spots are fluorescent particles. The positions of the microdonut and the bus waveguide are indicated by the orange broken lines. The three particles trapped on the microdonut are indicated by white arrows. The right side is the measurement interface, with the upper part containing the scan settings, and the lower part containing two data charts. The transmission spectrum is shown as the left chart after each scan. The peak finding function of Labview is used to determine the resonance wavelength immediately after each transmission spectrum is measured. This allows the resonance wavelength to be found as a function of time (right chart). The three jumps of the resonance wavelength labeled in right chart with white arrows correspond to the three trapping events that capture the three trapped particles shown in the left side image. After each trapping event, the resonance wavelength assumes a larger value. This illustrates that the system permits particle trapping to be monitored in real time.

### *6.3.4 Particle counting*

In Figure 6-6, the measured shift in microdonut resonance wavelength is plotted as a function of the number of trapped particles. These have a diameter of 2 μm. The results show a linear increase of resonance shift with the number of trapped particles, with the slope corresponding to a 30 pm resonance shift per particle. The stable particle number counting together with the real-time monitoring could be used to control the on-chip particle manipulation without using external imaging system, and therefore dramatically reduce the footprint and cost of the system

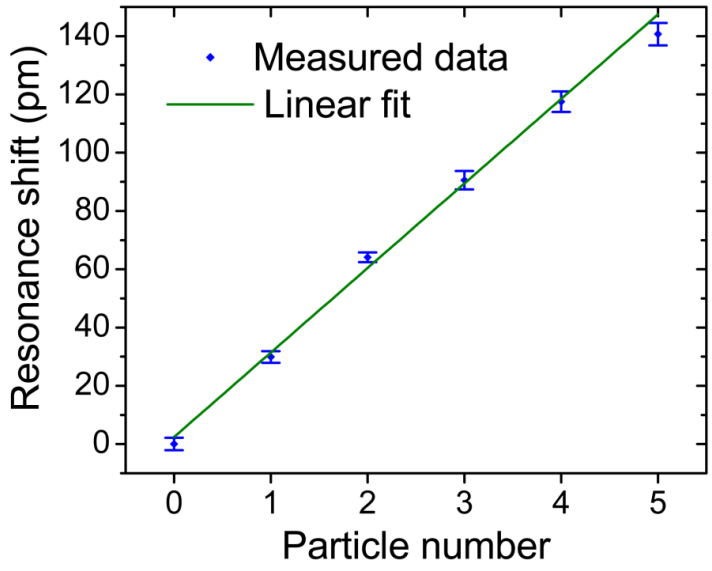


**Figure 6-6 Resonance shift as a function of the number of trapped particles with a diameter of 2 μm.**

### *6.3.5 Particle size sensing*

Our trapping-assisted sensing technique provides a reproducible signal in single particle sensing due to the self-alignment that occurs between the trapped particle and the field maximum. Figure 6-7(a) shows the measured resonance shift when a 320 nm polystyrene particle is trapped on the microdonut. The variations of the resonance wavelength before and after the trapping are both small. A clear wavelength shift can be measured for very small particles. Therefore, our system is capable of detecting the size of a single particle precisely. Figure 6-7(b) shows the peak shifts for particles with different diameters also measured using the same approach. One might expect the curve to show a superlinear behavior, being approximately proportional particle dipole

moment[62], [92], which is in turn proportional to volume. The curve shows a sublinear behavior however, but this can be explained the fact that the fraction of each particle that overlaps with the closely confined evanescent field of the microcavity decreases with particle size. Using the system and microdonut resonators, we have trapped and sensed particles as small as 200 nm diameter, which show a peak shift of 2.1 ± 0.4 pm.

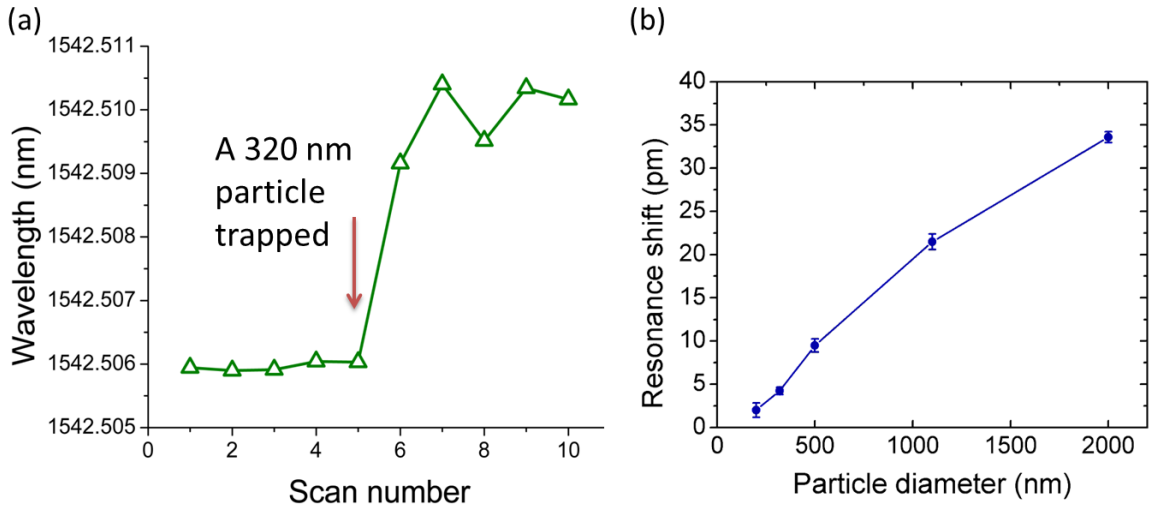


**Figure 6-7 (a) Resonance wavelength shifts when a 320 nm particle is trapped. The resonance wavelengths are determined by fitting the transmission spectra with a Lorentzian function. (b) The resonance shift as a function of the particle diameter.**

### *6.3.6 Particle sensing using photonic crystal cavity*

We next investigate the use of a nanobeam photonic crystal cavity (Figure 6-4(c)) with a Q of ~ 2000 (Figure 6-4(d)) for trapping and sensing as a means for improving the sensitivity *via* its small mode volume. The measured average resonance shifts as a function of particle diameter are

shown as the green symbols and curve in Figure 6-8. The resonance wavelengths are determined by fitting the transmission spectra with a Lorentzian function, which provides a high sensing resolution even for a low Q cavity. The mean and standard deviation for each data point are obtained by averaging multiple scans ( $\geq 6$) performed under the same conditions. The error bars represent plus and minus one standard deviation from the mean. Particles as small as 110 nm diameter are trapped and detected, and show a peak shift of $21 \pm 8$ pm. Due to its smaller mode volume, the particle-induced resonance shifts for the photonic crystal cavity are larger than those of the microdonut. The enhancement is 65-fold for the 200 nm particles (wavelength shift $\Delta\lambda$ increases from 2 pm to 130 pm), while 20-fold for the 2 μm particles ($\Delta\lambda$ from 34 pm to 680 pm). The enhancement is more profound for smaller particles, being closer to the factor of ~150 that one would expect from mode volume considerations alone. FDTD simulations show that the microdonut has a mode volume ~150 larger than that of the photonic crystal cavity. For both the photonic crystal and microdonut, the fraction of each particle that overlaps with the evanescent field decreases with increasing particle size. The increase in cavity mode perturbation is therefore smaller than one might anticipate from the particle size increase alone. The effect is more pronounced for the photonic crystal cavity than the microdonut, due to its larger in-plane confinement. It is for this reason that the resonance shift enhancement is more profound for smaller particles.

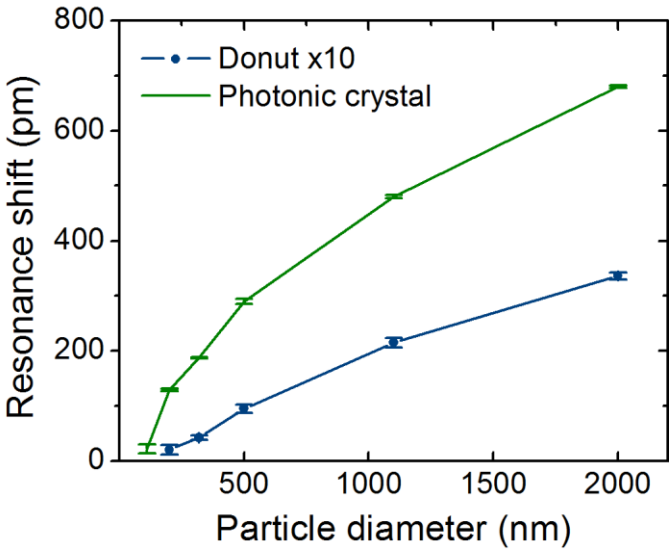


**Figure 6-8 Resonance shift as a function of particle diameter for the microdonut (blue) and photonic crystal cavity (green). The resonance shift values for microdonut have been multiplied by 10 to facilitate comparison.**

## 6.4 Summary

We demonstrate a particle sensing system based on waveguide-coupled silicon microcavities (microdonuts or 1D photonic crystal cavities). The size and number of trapped particles are determined *via* monitoring microcavity resonance shifts in real time. The optical trapping-assisted sensing technique we introduce has the advantage of reusability. Optical trapping provides an effective way to load and release the objects to be sensed without additional processes such as cleaning.

# Chapter 7 Trapping-assisted protein sensing by refractometry

The detection of protein molecules lies at the heart of many medical diagnostic applications. There has been recently much interest in integrated lab-on-a-chip microanalysis systems, due to their low reagent consumption, small footprint, and potential as low cost and portable diagnosis systems. Optical biosensors present opportunities for these systems, due to light being non-invasive to biological samples. Sensing is usually performed by having the target molecules binding to the functionalized optical biosensor surface. This has a few drawbacks, however. To bind to the surface, molecules must first diffuse to it; a process that can significantly decrease sensing speed [92, 93]. Furthermore, because the molecules bind to the sensor surface, cleaning steps are needed before the testing of each sample, and the device cannot be reused indefinitely. In this chapter, we employ our trapping-assisted platform for the sensing of protein molecules based on a binding assay. Instead of trapping and detecting the molecules directly, polystyrene particles coated with antibodies are used as carriers to interact with the target molecules. The molecule induced particle clusters are trapped and detected by our two-laser system to provide quantitative information on the sample.

## 7.1 Introduction to protein sensing

The sensing of biomolecules such as proteins is a basic operation in the life sciences. Traditional

fluorescence-based biological sensing techniques such as enzyme-linked immunoassays (ELISA) require complex chemical amplification or fluorescent labeling procedures, which increase the complexity and cost of the testing. This has motivated the development of simpler lab-on-a-chip approaches.

Biosensors based on high *Q* optical cavities permit enhanced light-matter interactions and sensitivities down to the single molecule level. Remarkable results have been recently obtained on the highly sensitive detection of analytes *via* the resonance shifts that result when they bind to the surfaces of optical microcavities[14], [29], [93]. Unlike traditional fluorescence-based biological sensing techniques, microcavity-based sensors do not require complex chemical amplification or fluorescent labeling procedures.

While impressive results have been obtained, microcavity sensing currently faces a number of obstacles. Typical microcavity sensing experiments involve the analyte binding to[29], or being physically adsorbed by, the microcavity surface[27], [63]. These methods introduce additional processes to attach and remove the analyte such as functionalizing the surface, immobilizing antibodies, and chemical or laser cleaning, thereby reducing sensing speed and increasing cost. Meanwhile, the resonance shift depends on the position of the analyte within the cavity mode[27], which is especially problematic if the analyte consists of a discrete entity such as a nanoparticle. As noted earlier in this thesis, the lack of position control in current analyte loading methods makes the quantitative interpretation of experimental data therefore problematic.

In this chapter, we demonstrate a new approach that overcomes these drawbacks by performing a binding assay with functionalized particles as carriers.

## 7.2 Experiment design

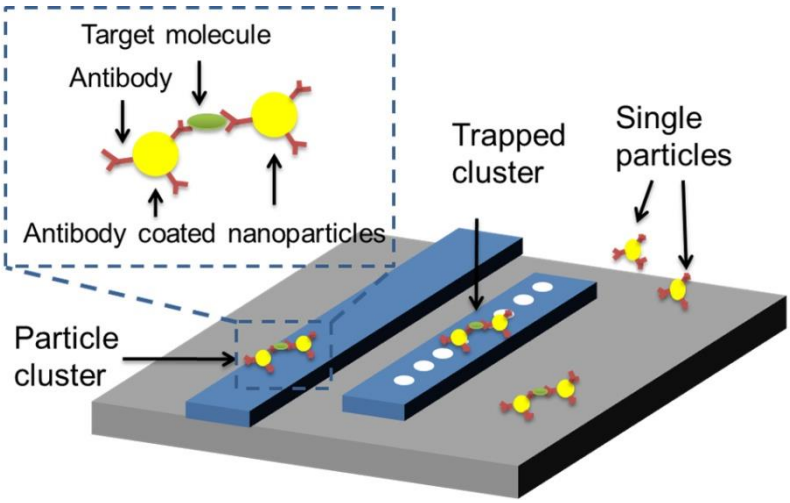


**Figure 7-1 Schematic diagram of the binding assay. Inset: particle cluster formed as a result of the presence of the target molecule in the sample.**

Figure 7-1 shows a schematic diagram of the proposed trapping-assisted sensing technique. Polystyrene particles are coated with antibodies that specifically bind with the target protein molecules. The target molecules therefore cause the particles to aggregate into clusters. The particle clusters are trapped and detected by the microcavity. By measuring the resonance shifts of trapped particles, we can therefore detect molecules in solution without having them bind directly to the resonator. Our approach enables determination of target molecule concentration

from the measured histogram of resonance shifts. High concentration samples generate a larger proportion of clusters (and a smaller proportion of single particles) than low concentration samples. In addition to reusability, our approach enables a single device to detect different types of molecules, through the use of multiple bead types with different functionalizations. Lastly, because the molecules bind to beads in solution, rather than to a sensor on the wall of a microfluidic channel, our approach could help address the diffusion bottleneck problem present with low concentration samples[94], [95].

The trapping and release of particles and particle clusters by the photonic crystal cavity is controlled *via* varying the trapping laser polarization. The trapping laser polarization is first set so that 50% of the power is in the transverse electric (TE) mode, while the remaining 50% of the power is in the transverse magnetic (TM) mode. The TM mode exhibits enhanced electric fields on the top surface of the waveguide. The TM portion of the light therefore traps the particles onto the waveguide and propels them to the cavity. The TE mode couples to the photonic crystal cavity. The TE portion of the light, which generates high field enhancement in the cavity, therefore pulls particles from the bus waveguide to the cavity. The polarization of the probe laser is set to be TE mode, to make it sensitive to resonance shifts of the photonic crystal cavity. The resonance wavelengths of the cavity before and after each trapping event are obtained by scanning the probe laser in a 5 nm bandwidth about the resonance wavelength at a rate of 5 nm/s. After each measurement, the trapped particle is returned to the waveguide by setting the trapping laser polarization to be completely TM mode.

### 7.3 Device and sample preparation

We use a 1D photonic crystal cavity to perform the protein sensing measurements. The photonic crystal cavity is fabricated on a silicon-on-insulator (SOI) wafer. The device design and fabrication process are as described in Chapter 4. A PDMS microfluidic channel with a width of 200 μm and a height of 50 μm is bonded to the chip. Before measurements, the surfactant tween 20 (0.1% *v/v*) is added to the solutions to prevent non-specific binding between the particles and photonic sensor. In addition, before the measurements, casein blocking buffer is flowed through the microfluidic channel and incubated for 30 minutes to further prevent non-specific binding.

We choose green fluorescent protein (GFP) for our demonstration, which has a molecular weight of 27 kDa. Each GFP molecule possesses multiple active sites that can bind with its antibodies. Polystyrene particles with diameters of 320 nm are used as the carrier particles, as depicted in Figure 7-1. The polystyrene particles are added to phosphate buffered saline (PBS) solution and mixed with the GFP antibody at room temperature for 2 hours. Solutions containing GFP at different concentrations are then added and mixed at 4˚C for 2 hours. The sample preparations are performed at Stanford University and then sent to Harvard University. The GFP antibodies and GFP molecules are gifts from Dr. Yuan Cheng from the laboratory of Professor Hsueh at Stanford University. During the shipping time (~48 hours), the mixed samples are kept at 4˚C.

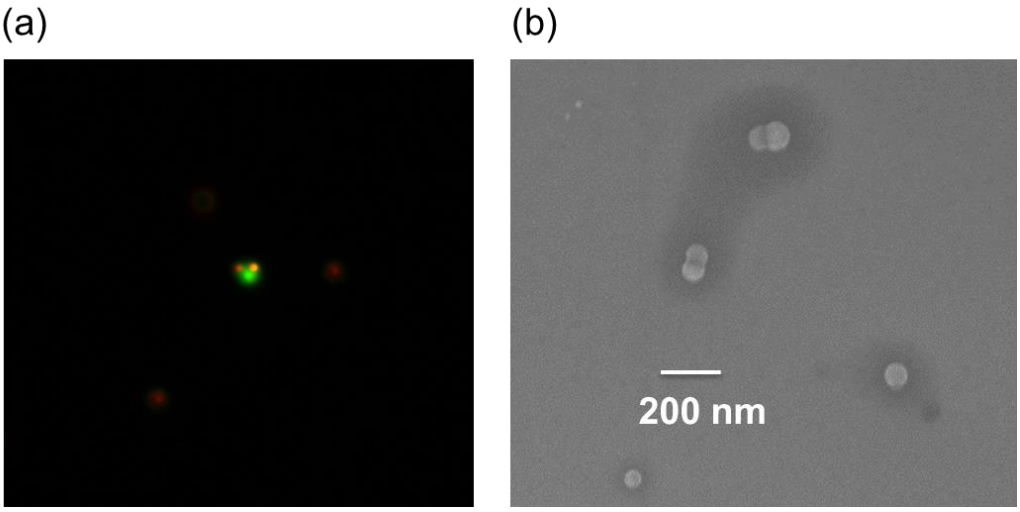


**Figure 7-2 (a) Fluorescence microscope image of the sample after the GFP molecule solution is mixed with antibody-coated particles. (b) SEM image of sample after it is dried on a coverslip.**

Figure 7-2(a) shows a fluorescence microscope image of the sample that consists of GFP molecules mixed with antibody-coated particles. It is obtained with a 50× magnification objective lens. The red dots represent the fluorescent emission from the polystyrene particles that contain the Nile red dye. The green represents the fluorescent emission from the GFP molecules. This microscope image confirms that the presence of the GFP molecules causes aggregation of the antibody-coated particles. This does not of course yield the quantitative information of our microcavity method. We also confirm that particle aggregations form by scanning electron microscopy of the sample after it is dried onto a coverslip. This is shown in Figure 7-2(b), although the surface tension may also contribute to aggregation during the drying process.

## 7.4 Experimental results

### *7.4.1 Measurement of control sample without GFP*

We first measure a control sample that contains antibody-coated polystyrene particles, but does not contain GFP molecules. The sample is introduced to the cavity through the microfluidic channel. Figure 7-3a shows the measured resonance shifts for 60 trials. It can be seen that the resonance shifts are fairly uniform. This can also be seen in Figure 7-3(b), in which the trials have been sorted into ascending order. The average resonance shift is found to be 120 ± 7 pm. The results are consistent with the sample containing only single particles, since the clusters would induce a much larger resonance shift. One might expect a two-particle cluster to produce a resonance shift roughly double that of a single particle. From the manufacturer's specifications, we estimate that particle size coefficient of variation contributes to the standard deviation by ~ 5 pm. Another factor that could contribute to the standard deviation is Brownian motion of the particles during the measurement interval.

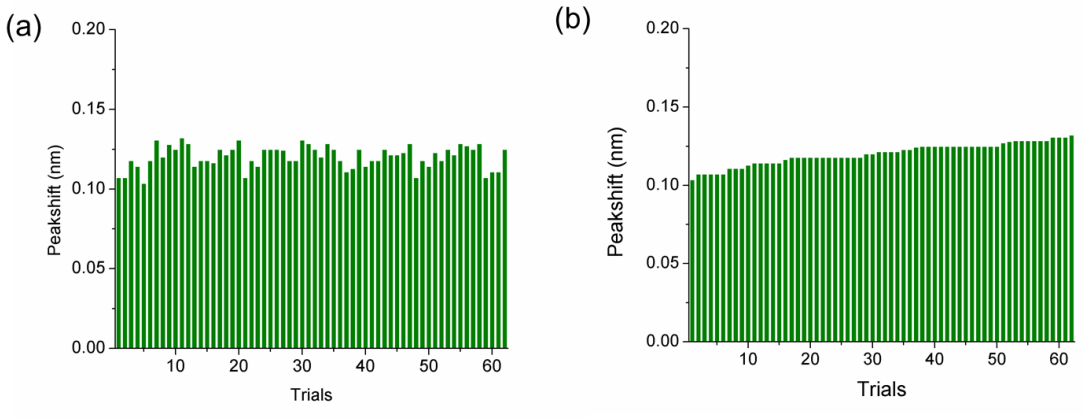


**Figure 7-3 Resonance wavelength shifts for sample without GFP molecules (a) before and (b) after sorting the peak shift in ascending order.**

### *7.4.2 Measurement of samples with different GFP concentrations*

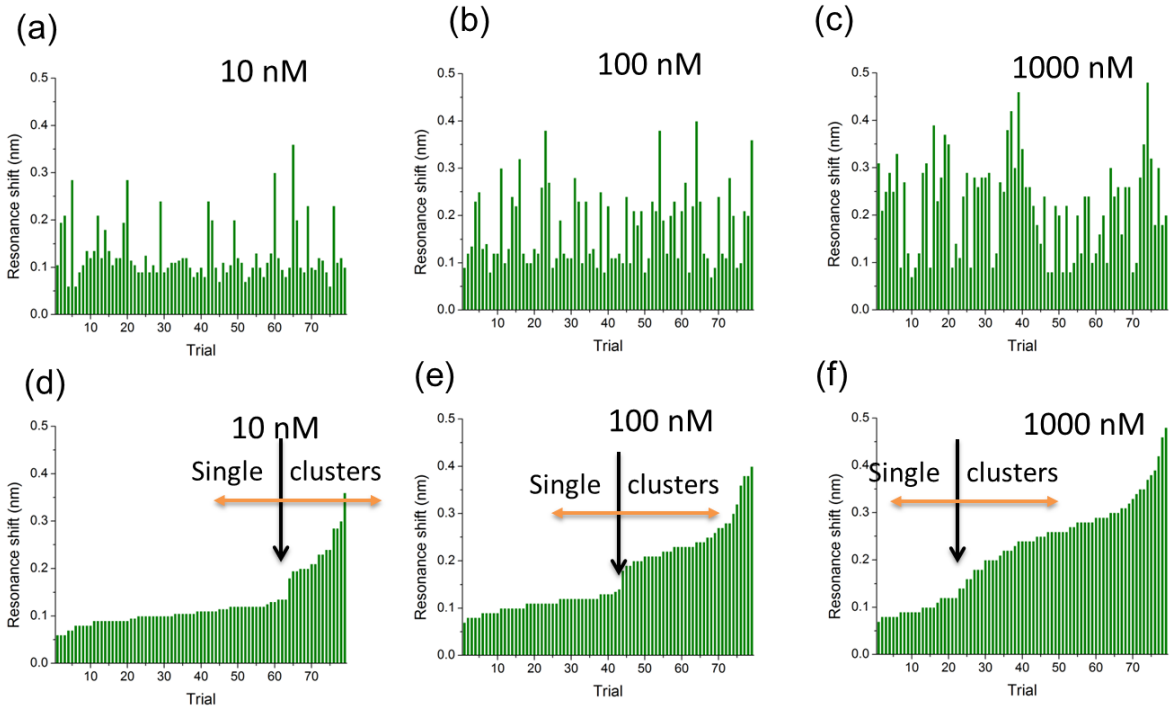


**Figure 7-4 Resonance wavelength shifts for sample with GFP at concentrations of (a) 10 nM, (b) 100 nM, and (c) 1 µM. (d-f) the resonance shifts for different GFP concentrations after being sorted in ascending order.**

We next measure samples containing GFP at different concentrations. For each sample, 80 particles or particle clusters are trapped, with the resonance shift determined for each. The results are shown in Figure 7-4(a)-(c). Figure 7-4(d)-(f) show the results with the trials sorted to place resonance shifts in ascending order. Figure 7-4(d) shows that the measured results of GFP concentration of 10 nM demonstrate a marked step at trial 64. This indicates the trapping of

particle clusters. The majority of the trapped objects (trials 1-63) are single particles with resonance shifts around 110 pm, with the remainder (trials 64-80) being clusters. In Figure 7-4(e) and (f), we present results obtained for GFP concentrations of 100 nM and 1000 nM. It can be seen that the transition between single particles and clusters occurs at lower trial numbers, indicating a smaller fraction of single particles for the higher concentration samples. This is due to the fact that the probability of a particle encountering a GFP molecule, and therefore being able to bind with another particle, increases with GFP concentration.

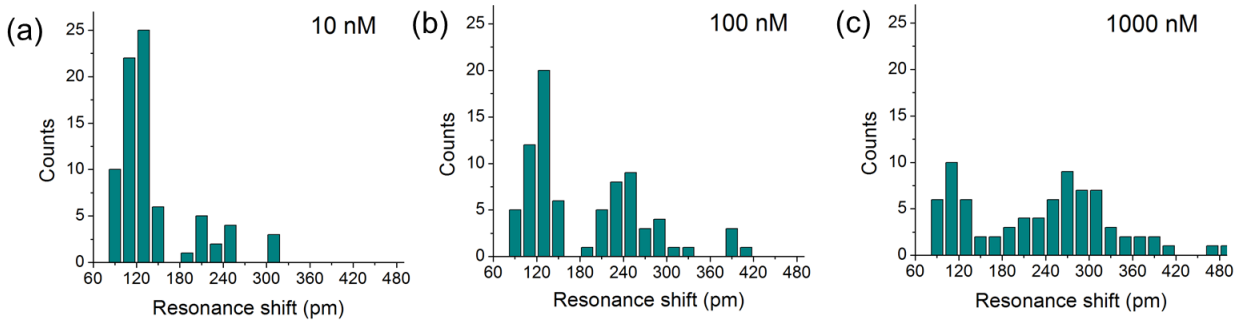


**Figure 7-5 Distribution histograms of the measured resonance shifts for GFP concentrations of (a) 10 nM, (b) 100 nM, and (c) 1000 nM.**

Resonance shift distribution histograms produced from the data of Figures 7-4(d)-(f) are shown as Figure 7-5. The measured wavelength shifts are divided into intervals of 20 pm, and the numbers of trials falling into each interval are plotted. All three concentrations show a peak at ~110 nm corresponding to single particles. Interestingly, single particle events with shifts as small as 60 nm occur. These shifts are smaller than those measured from single particles in the no-GFP case. One explanation is that the GFP molecules increase the distance between the

particles and the device surface, thereby decreasing the resonance shift. The number of single particle events decreases as the GFP concentration increases. It can be seen that few events occur with shifts of ~150 nm, with this "valley" separating the single particles from the clusters. The peak following the valley corresponds to the particle clusters. This peak is broader than that corresponding to the single particles. We attribute this to the fact that the clusters are comparable in size to the microcavity and can be trapped in different positions on it, leading to variation of the induced resonance shift. For the 1000 nM sample, there are some events occurring in the valley between single particle clusters. Nonetheless, the delineation between single particles and clusters is clear, and it can be seen that number of cluster events increases with the GFP concentration.

### *7.4.3 Quantitative analysis of GFP molecules*

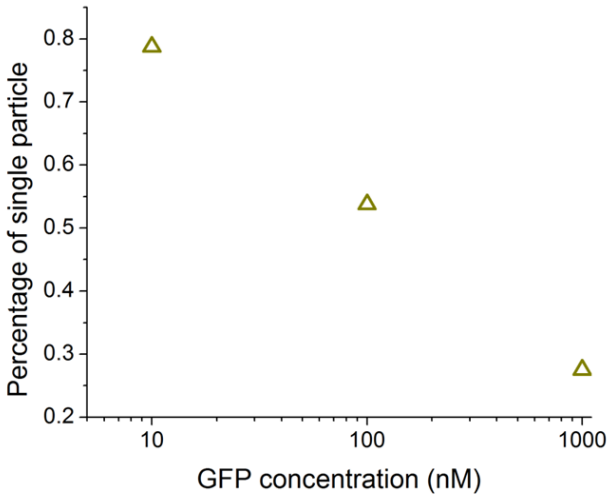


**Figure 7-6 The percentage of single particles as a function of GFP concentration.**

Figure 7-6 plots the percentage of trapping/sensing events that are single particles as a function

of GFP concentration. Here, we assume the trials with a peak shift < 141 pm (mean of the measured peak shift plus three times the standard deviation in Figure 7-3) correspond to single particles. This criterion is also consistent with the valley positions in Figure 7-5. It can be seen that this method represents a quantitative tool for detecting the concentration of target molecules. In addition to depending on the details of the optical measurement technique, the sensing limit and dynamic range also depend on the properties of the binding process. Improving the binding efficiency would present a means for improving the sensing limit. Since the binding happens before the particles are trapped, the current approach is not suitable for applications requiring the monitoring of binding kinetics.

### *7.4.4 Optimization of sensing speed*

Sensing speed is an important parameter for cavity-based sensors, especially for quantitative analysis, where the number of detection events needs to be sufficiently large for meaningful results to be obtained. Our platform has several favorable attributes in this regard. The general approach to cavity sensing, in which molecules bind to the cavity surface, sometimes faces the drawback of long response time due to the properties of mass transport in microfluidic channels. In our approach, on the other hand, binding occurs outside the microfluidic channel. One could therefore use active mixing techniques to improve the binding efficiency still further. To improve the trapping rate, we use a combination of TE & TM modes, which effectively turns the long waveguide into a particle collector. The use of the waveguide as a particle collector is facilitated by the fact that it is patterned by lithography. There is therefore considerable flexibility in its

design that is not present for cavities (*e.g.* microspheres or microtoroids) coupled to with tapered optical fibers. The fact that the trapping and release of particles is controlled *via* polarization rather than laser power is also more favorable for achieving a high sensing speed. The particles trapped on the waveguide are continuously delivered to the cavity without interruption. This would not be the case if trapping were controlled by turning the laser on and off, because this would result in all trapped particles being released, including those on the waveguide. Lastly, we note that the concentration of the particles is chosen to enable a convenient trapping rate, with sufficient time between trapping events to perform sensing. In our experiments, the particle concentration ($5.8\times10^{15}$ particle/$m^3$) enables one measurement every ~30 seconds. The 80 trial measurements we perform therefore take ~40 minutes. The trapping efficiency is low due to the microfluidic channel being tall and the limited spatial extent of the optical force. Although the sensing results won't be affected, improving the trapping efficiency by reducing the channel height could reduce the analyte consumption.

### 7.5 Summary

In summary, we apply our integrated trapping and sensing platform to detect proteins *via* antibody-antigen binding. In the presence of the target molecules, the antibody-coated particles form clusters that can be detected by our platform and quantitatively analyzed. In addition to the life sciences, this label-free, reusable and reliable on-chip sensing system could be employed for a range of applications in nanotechnology and in environmental monitoring.

# Chapter 8 Trapping-assisted SERS

Surface enhanced Raman scattering (SERS) enables molecules to be identified with very high sensitivity. SERS substrates based on colloidal metal nanoparticles are inexpensive and easy to prepare, but rely on the salt-induced formation of aggregates for high performance, a process over which there is little or no control. Plasmonic structures produced by top-down nanofabrication possess high signal enhancement and controllability, but require complex fabrication processes and are one-time use only. In this chapter, we demonstrate a reusable and reconfigurable SERS platform by optically trapping Ag nanoparticles with a photonic crystal cavity integrated with a microfluidic chip. High performance SERS is performed in a very reproducible manner, owing to the fact that Ag aggregates are generated by optical trapping in a controllable process that is monitored in real-time by the cavity resonance shift that occurs with the trapping of each additional nanoparticle. We furthermore demonstrate that the nanoparticles can be released and fresh nanoparticles trapped by the same photonic crystal cavity. We show that this enables the sensing of multiple analytes supplied sequentially to the microfluidic chip.

## 8.1 Introduction to SERS

Surface enhanced Raman scattering (SERS) enables molecules to be identified by their vibrational “fingerprints”[96], [97]. SERS applications range from the detection of biological

warfare agents such as anthrax[98], to explosives[99], to pollutants such as arsenic in drinking water[100], to contaminants in foods (*e.g.* melamine in milk[101]), to glucose levels measured in-vivo[102]. To overcome the fact that Raman cross sections are small, a variety of SERS substrates with large field enhancements have been developed, including nanoparticle colloids[103], [104], rough metallic surfaces[105] and nanoantennas[106–109]. In almost all cases, however, these substrates are only one-time-use, due to the fact that the molecules bind very strongly to them. That SERS substrates generally need to be discarded after use has two principal disadvantages. The first is that of cost. The second is that it renders them unsuitable for applications for which manual human intervention to replace the SERS substrate is infeasible, *e.g.* unattended systems for the continual monitoring of chemicals in air and water. A high performance substrate that could be refreshed at-will would be a new paradigm in SERS sensing. Here, we demonstrate such a device, by trapping Ag nanoparticles using an on-chip optical cavity[13], [110], [111]. The Raman emission from molecules on the surfaces of the nanoparticles is enhanced due to the large electromagnetic fields there. We demonstrate that the resonance shift of the cavity enables monitoring of trapped nanoparticles, which make the controllable assembly of Ag aggregations possible. We note that this functionality was not present in recent optical trapping-assisted SERS experiments with traditional optical tweezers[112], [113] and light induced optoelectrofluidics[114]. We demonstrate that turning the laser off, then on again, results in the nanoparticles being released, and fresh particles being trapped. Our device has not only the advantage of reusability, but also that of reconfigurability. Nanoparticles, of different sizes, shapes, materials and surface functionalizations, could be

supplied to the chip. The type of nanoparticles to be trapped could be chosen based on the chemical to be sensed.

### 8.2 Trapping-assisted SERS

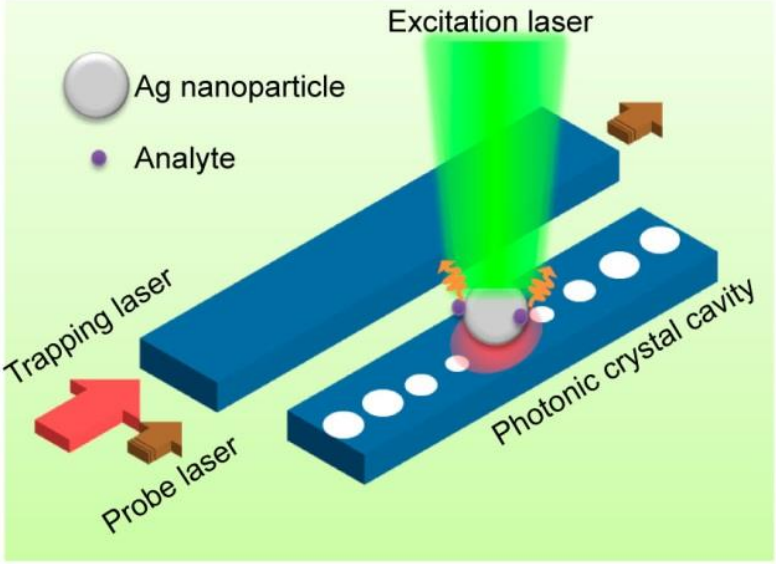


**Figure 8-1 Schematic diagram of trapping-assisted SERS platform.**

Figure 8-1 shows a schematic diagram of the trapping-assisted SERS platform we introduce. Analyte molecules (4-Aminothiophenol (pMA) or 2-naphthalenethiol (2-NT)) are first mixed with Ag nanoparticles with diameters of 80 nm. The nanoparticles, onto which the analyte molecules have bound, are then sent into a microfluidic channel and optically trapped by a photonic crystal cavity that is situated at the bottom of the channel. The beam from a trapping laser is combined with that from a second (lower-power) probe laser, and input to the device. The probe laser is continually swept in wavelength, enabling the resonance wavelength of the optical cavity to be monitored. An upright homemade microscope is used to measure Raman

scattering from molecules on the optically trapped nanoparticles, with excitation from a green laser ($\lambda$ = 532 nm).

## 8.3 Experiment design

### *8.3.1 Device and sample preparation*

We choose to use a photonic crystal cavity because its small mode volume and large field enhancement enable a large optical force enhancement for trapping Ag nanoparticles. Figure 8-2(a) shows a scanning electron microscope top-view image of the fabricated photonic crystal cavity coupled to a waveguide. Waveguides are 450 nm wide and 220 nm thick. The holes are shifted outward to form a cavity in the center. Tapered sections, with hole diameters that gradually increase from the cavity center, are incorporated to reduce the scattering loss of the cavity mode and to improve the quality factor. The photonic crystal cavity is fabricated on a silicon-on-insulator (SOI) chip. The fabrication process is described in Chapter 4. A thin PDMS film (100 μm thick) with a 1 mm wide channel cut in the center is bonded to the silicon chip. A glass coverslip (no.1.5) is then bonded to the top of the PDMS. The coverslip contains two holes that are drilled into it by a high power $CO_2$ laser. Holes are drilled in glass coverslip to let liquid into channel. A polydimethylsiloxane (PDMS) microfluidic channel with a width of 1 mm and a height of 100 μm is formed on the device, with a glass coverslip on top. The two thick PDMS chunks are for connecting the tubing, through which the analyte solution is injected. Figure 8-2(b)

shows an image of the final device and its cross section diagram. Figure 8-2(c) shows the measured transmission spectrum of the cavity. The Lorentzian fit shows a quality factor (Q) of 1500.

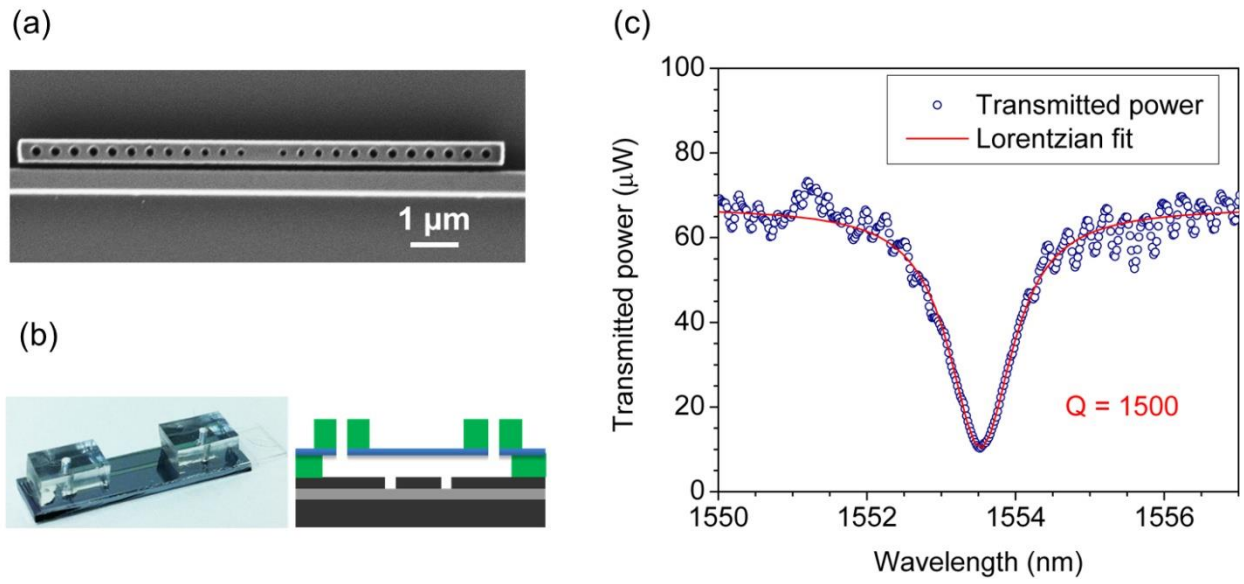


**Figure 8-2 (a) SEM image of 1D photonic crystal cavity coupled to waveguide with a gap of 200 nm. (b), Left: photograph of fabricated device that integrates microfluidic channel with silicon photonic chip. Right: schematic diagram of device cross section. (c) Measured transmission spectrum and Lorentzian curve fit, showing a Q of 1500.**

The pMA and 2-NT samples are purchased from Sigma-Aldrich Co. LLC. Each of these is dissolved in acetone and mixed with water containing Ag nanoparticles with diameters of 80 nm. The Ag nanoparticles are purchased from BBinternational and are stabilized by citrate. The mixed samples are left for 24-48 hours at room temperature before the measurements. The resultant solutions are supplied to the photonic crystal cavity through the microfluidic channel on

the chip.

### *8.3.2 Measurement setup*

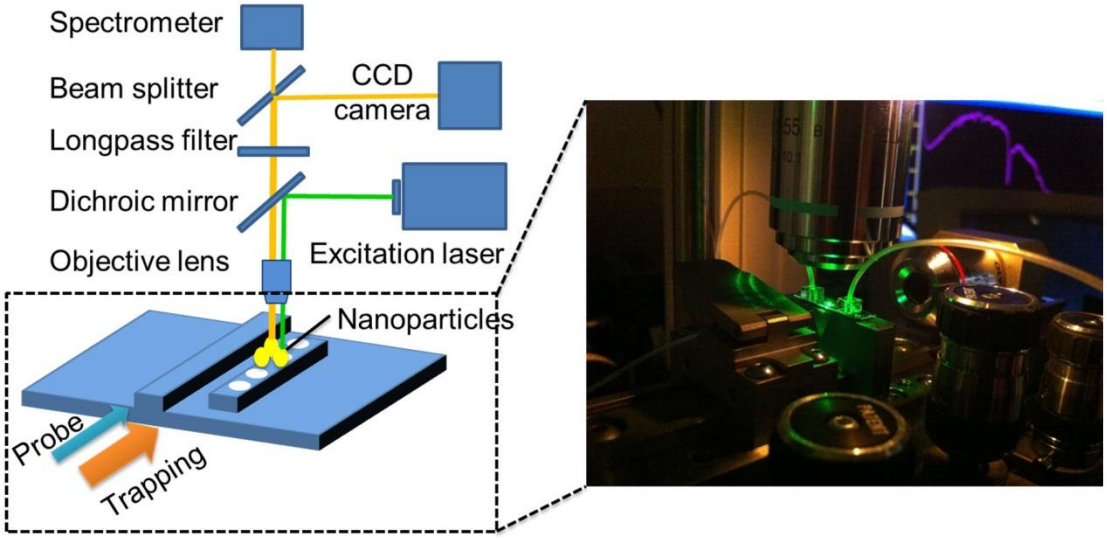


**Figure 8-3 Schematic diagram of the measurement setup. The right picture shows the close up view of the sample with tubing connected to the chip.**

Figure 8-3 shows the schematic diagram of the measurement setup. We use the two-laser system discussed in Chapter 6 to perform and monitor the optical trapping process. The trapping laser is amplified by an erbium-doped fiber amplifier (EDFA) and the probe laser is modulated at a frequency of 100 kHz. Both lasers operate around a wavelength of 1550 nm. The lasers beams are combined and input to the waveguide through a mode converter composed of a 2×2 μm SU8 waveguide on top of an inverse silicon taper [88].

An upright homebuilt microscope is used to perform the SERS measurements. A green laser operating at a wavelength of 532 nm is merged into the main optical path using a dichroic mirror and focused onto the photonic crystal cavity using a microscope objective lens (magnification: 50x, numerical aperture (NA): 0.45, working distance: 10.6 mm). The SERS signal is collected by the same objective lens and directed to a spectrometer with a liquid nitrogen cooled CCD. A long-pass filter, placed after the dichroic mirror, is employed to cut the excitation light. A 50/50 beam splitter is placed between the long-pass filter and the spectrometer to redirect half of the light into a visible CCD camera for imaging and alignment. The right picture in Figure 8-3 shows a close up view of the system.

## 8.4 SERS measurement results

### *8.4.1 Ag nanoparticles trapping and monitoring*

We first demonstrate the trapping of 80 nm Ag nanoparticles on the bus waveguide and the photonic crystal cavity. The trapping laser is set so that both a transverse electric (TE) mode (50% power) and a transverse magnetic (TM) mode (50% power) are excited. The TM mode traps nanoparticles on the waveguide more effectively than the TE mode since it has a stronger evanescent field and thus exerts a larger optical force. The wavelength is set to the resonance wavelength of the photonic crystal cavity, meaning that the TE mode can couple to it. The field enhancement, a consequence of the high Q factor and small mode volume of the cavity, enables nanoparticles to be readily trapped on it. The Supplementary Movie 8-1 shows an Ag

nanoparticle that is trapped on the waveguide by the gradient force and propelled along it by the scattering force. When it reaches the photonic crystal cavity, it is pulled onto it and trapped.

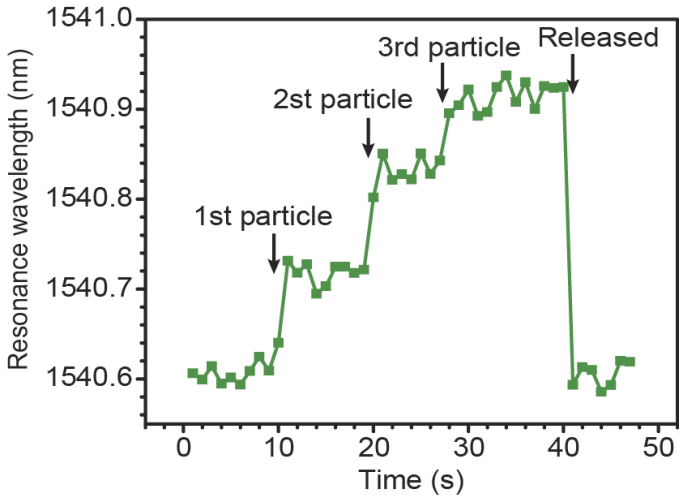


**Figure 8-4 Resonance wavelength shift as particles are trapped, as measured by probe laser.**

In addition to trapping nanoparticles, the waveguide-coupled cavity enables the monitoring of the trapped nanoparticles by measuring the cavity resonance shift using the probe laser. Figure 8-4 shows the resonance shift as a function of time after the trapping laser is turned on. The probe laser is continually swept in wavelength at 5 nm/s over a range of 5 nm. The resonance wavelength is found from each scan by fitting the transmission spectrum with a Lorentzian function. Trapping laser is turned on at t = 0 s. Three resonance wavelength jumps correspond to trapping three Ag nanoparticles on cavity. It can be seen that resonance wavelength jumps of ~0.1 nm occur with each additional nanoparticle being trapped. After turning off the trapping laser at ~40 seconds, the resonance wavelength returns to its value before the first particle was

trapped. That the particles can be released by turning off the trapping laser confirms that the trapping process is indeed optical in nature.

### *8.4.2 SERS measurements of pMA molecules*

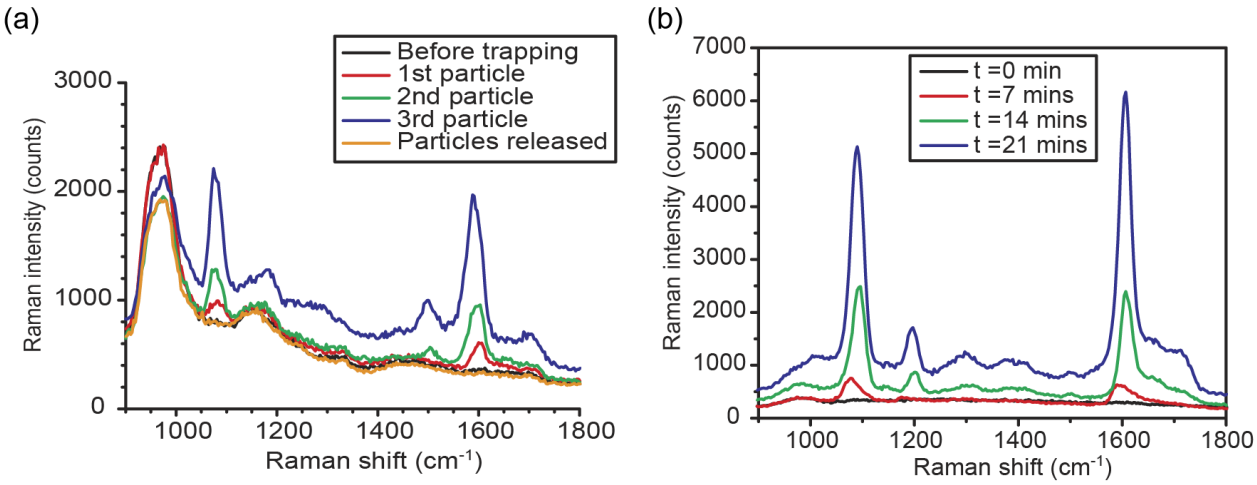


**Figure 8-5 (a), SERS spectra measured with different numbers of particles trapped. Laser power for SERS excitation is 3 mW and spectrometer integration time is 10 s. (b) SERS spectra measured with Ag nanoparticle aggregations of different sizes formed at different times. Laser power used for SERS excitation is 1 mW and spectrometer integration time is 5 s.**

SERS spectra measured during the trapping process, recorded at each resonance wavelength step (Figure 8-4), are shown in Figure 8-5(a). The solution contain pMA (250 μM concentration), Ag nanoparticles (1.72 pM), de-ionized water, and acetone. The Raman spectrum measured after releasing trapped nanoparticles is also shown. Within the measured Raman shift range (900-1800 $cm^{-1}$), there are two peaks originating from the pMA molecules (1077 $cm^{-1}$ and 1590 $cm^{-1}$) [115]. The SERS peak around 960 $cm^{-1}$ comes from the Si substrate. No pMA Raman peaks are

observed before trapping the nanoparticles. The Raman counts at the wavenumbers corresponding to the pMA peaks increase with the number of trapped particles. In Figure 8-5(b), we demonstrate that the SERS signal can be enhanced further by keeping the trapping laser on to form larger nanoparticle clusters. SERS spectra are measured at different times after turning on the trapping laser. At 21 minutes, the measured signal, divided by the laser power and spectrometer integration time, is 140 times larger than that of the single particle case in Figure 8-5(a). The drawback of trapping these large clusters is that they become irreversibly stuck to the cavity surface much more readily due to the large gradient force and long trapping time.

### *8.4.3 Calculation of the average enhancement factor*

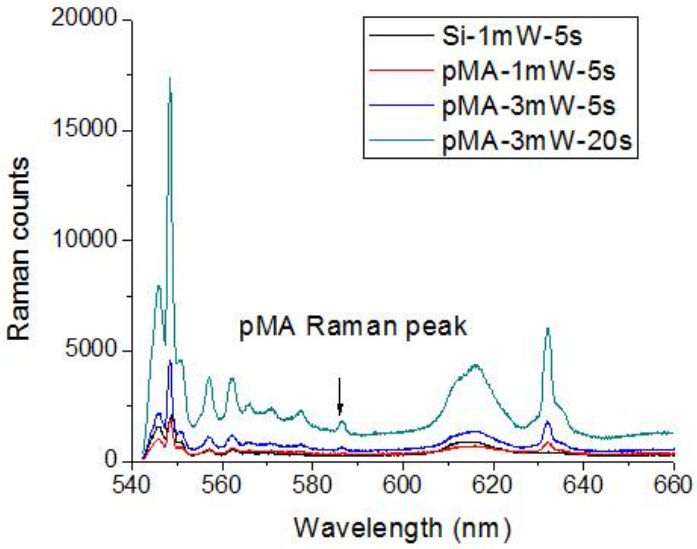


**Figure 8-6 Raman spectra of reference sample with pMA molecule concentration of 2.5 mM. The reference samples does not contain silver nanoparticles. Different excitation powers and integration times have been used. The black arrow shows the position of the pMA Raman shift peak**

To calculate the average enhancement factor, we measure a reference pMA sample with a concentration of 2.5 mM. No Ag nanoparticle are present in that sample. To increase the signal, we use a laser excitation power of 3 mW and a spectrometer integration time of 20 seconds. This yields the results shown as Figure 8-6.

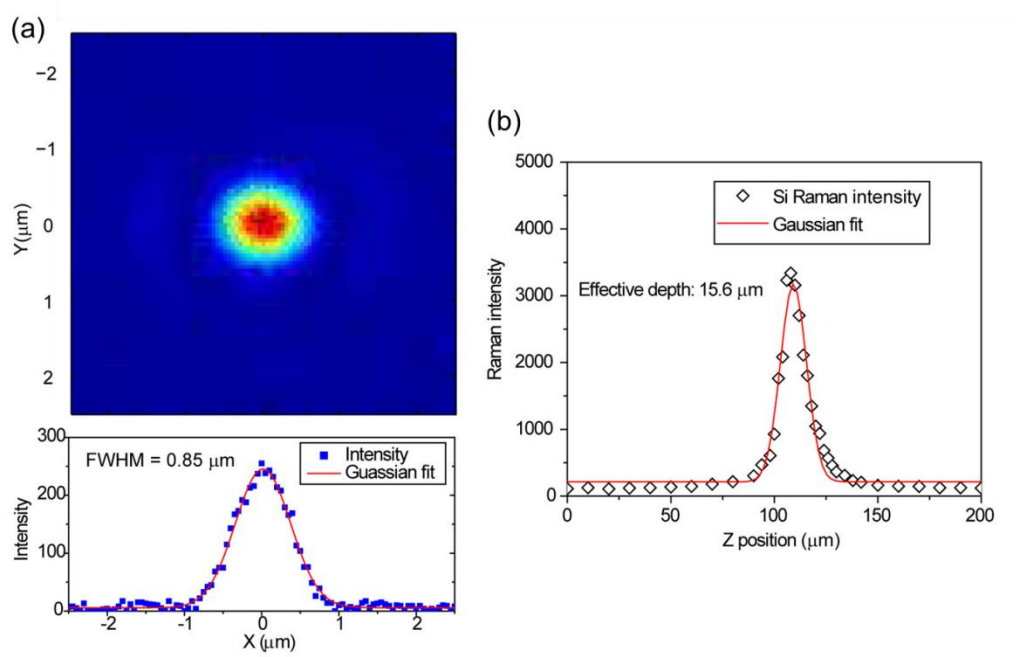


**Figure 8-7 (a), Top: measured excitation focal spot, as imaged by CCD camera. Bottom: intensity distribution on cross section along *x*-direction. (b), Raman intensity as function of vertical position (*z*, *i.e.* along optical axis) of a silicon chip**

The effective volume of the laser focal spot is measured by recording the Raman signal for different positions of the silicon chip along the optical axis (Figure 8-7)[116], [117]. The effective depth ($l_{eff}$) is calculated to be 15.6 μm. This is found by dividing the area below the curve by its peak value. By imaging the excitation spot onto a CCD camera (Figure 8-7(a)) and

fitting it with a Gaussian function, we find that it has a beam width ($w$) of 0.72 μm. The effective spot size ($A_{eff}$) is calculated to be 0.82 μm$^2$ by

$$A_{eff} = \int_0^{2\pi}\int_0^{\infty} \exp(-2\cdot\left(\frac{r}{w}\right)^2)\cdot r\, dr\cdot d\theta = \frac{\pi\cdot w^2}{2} \tag{8.1}$$

The effective volume is calculated by

$$V = A_{eff}\cdot l_{eff} \tag{8.2}$$

The total number of molecules in the focus spot for the reference sample is then calculated by:

$$N_r = V\cdot c \tag{8.3}$$

where $c$ is the concentration of the molecule.

The number of molecules on the surface of each Ag nanoparticle is calculated by assuming a monolayer of pMA molecules formed on the surface, with each molecule occupying an area of $A$ ($A$ = 0.3 nm$^2$)[118]. Therefore, the number of molecules on each nanoparticle is calculated by:

$$N_p = \frac{4\pi\cdot {r_p}^2}{A} \tag{8.4}$$

here, $r_p$ is the radius of each Ag nanoparticle.

The average enhancement factor (EF) is then calculated using the following equation:

$$\eta = \frac{I_p/(N_p\cdot n)}{I_r/N_r} \tag{8.5}$$

where $I_p$ and $I_r$ are the Raman intensities measured for the sample with nanoparticles and the reference sample, respectively. $n$ is the number of Ag nanoparticles within the focal spot.

Taking the measured data in Figure 8-5(a) and Figure 8-6, the average enhancement factors are calculated to be $2.3\times10^3$, $2.8\times10^3$, and $4.1\times10^3$ for one-, two- and three-particle cases,

respectively. It should be noted that these refer to the average factor by which the Raman scattering from a PMA molecule on the Ag nanoparticle is enhanced, compared to the Raman scattering from a PMA molecule in a nanoparticle-free PMA solution, with differences in laser power and spectrum integration time accounted for. The average enhancement factor increases as the number of particles increases due to the field enhancement in the gaps between nanoparticles. These represent the average values by which Raman scattering for all molecules on the nanoparticle surfaces are increased, compared to the reference case of the molecules being in pMA solution (without the nanoparticles). It should be stressed that these are average values; the EF for molecules in the hotspot regions is inevitably much higher. After turning off the trapping laser, the Raman spectrum also returns to its original state before the first particle was trapped, as shown in the orange curve of Figure 8-4(a). This demonstrates that our approach enables a surface-enhanced hotspot (*i.e.* the optically trapped nanoparticles) to be formed and released in a controllable manner.

### *8.4.4 Numerical simulation of the electromagnetic enhancement factors*

The field distributions around the Ag nanoparticles in different configurations are simulated by the finite-difference time-domain (FDTD) method. A plane wave (free space wavelength: 532 nm) is launched from the top. A 3D field monitor is used to record the field intensity distribution surrounding the nanoparticles. Figure 8-8 shows the field intensity distributions for one particle (case 1, Figure 8-8(a)), for two particles separated by 20 nm (case 2, Figure 8-8(b)) and for two

connected particles (case 3, Figure 8-8(c)). These represent the square of the electric field, normalized to that of the illuminating plane wave. To find the average SERS enhancement factor we perform the following[119]. We integrate the field intensity squared (electric field to fourth power) over the nanoparticle surface, and divide it nanoparticle surface area. We then divide this by the square of the incident field intensity. This then gives the average value by which SERS from a molecule on the nanoparticle surface is enhanced, compared to a molecule in free space, assuming a Raman shift of zero. The enhancement factors for case 1 and 2 are found in this way to be $3.6\times10^{3}$ and $1.1\times10^{4}$, respectively. On the other hand, the enhancement factor for case 3 ($1.1\times10^{6}$) is two orders of magnitude larger than case 1 and 2. As shown in Figure 8-5, the increase in signal with the trapping of the second particle is not dramatic. We therefore conclude that the two particles are in a configuration more similar to Case 2 rather than Case 3, *i.e.* there is a gap. We conclude that the negative charges on the surfaces of the nanoparticles, which arise from the citrate treatment, provide a repulsive force that prevents the particles from collapsing into a cluster of the type of Case 3.

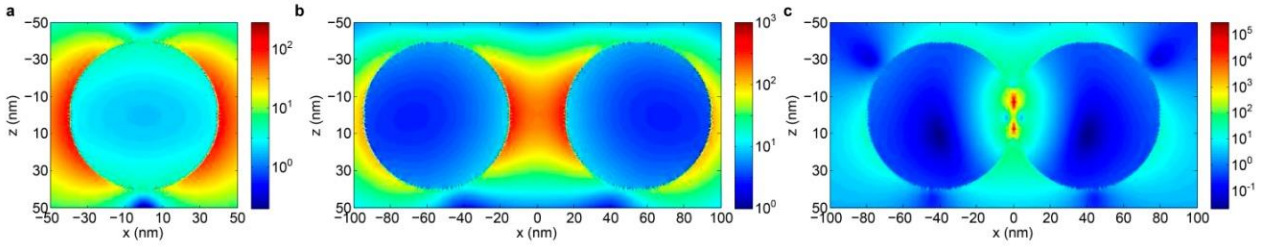


**Figure 8-8 Simulated field intensity distribution ($|E|^2$) on the cross section across the centers of the nanoparticles for (a) one particle, (b) two nanoparticles with a gap of 20 nm, and (c) two nanoparticles connected.**

### *8.4.5 SERS measurements at different concentrations*

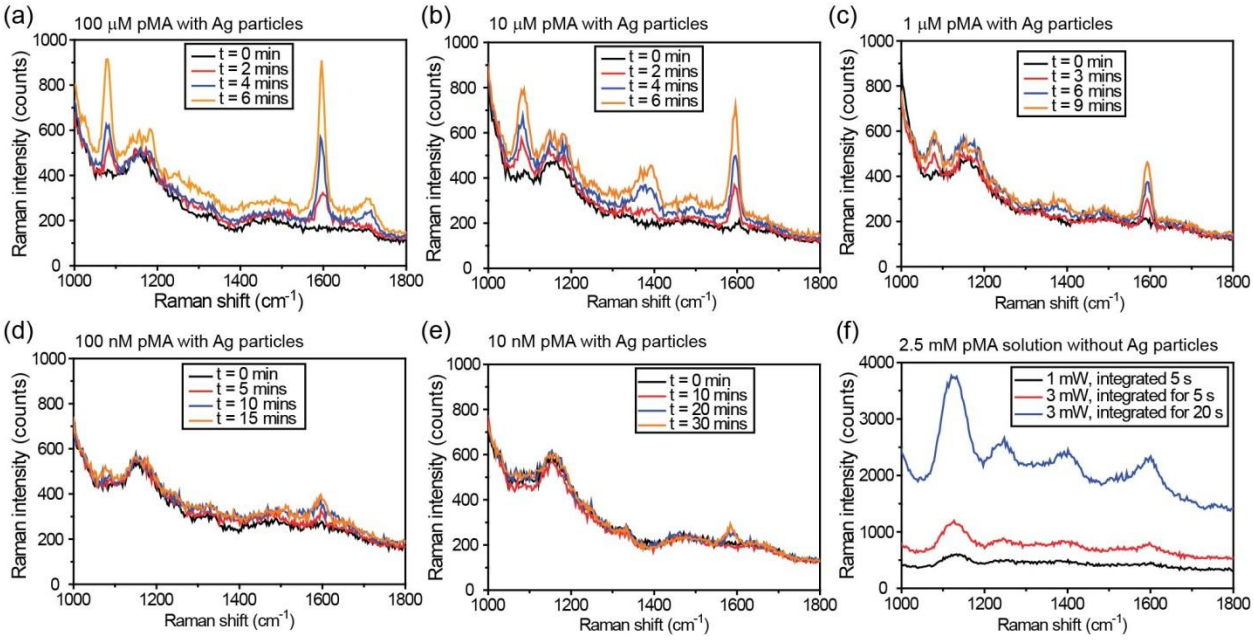


**Figure 8-9 Raman spectra measured by the trapping-assisted approach for samples with different pMA concentrations: (a) 100 μM, (b) 10 μM, (c) 1 μM, (d) 100 nM and (e) 10 nM. Laser power for SERS excitation is 1 mW, and spectrometer integration time is 5 s for all measurements. The pMA solutions are first mixed with Ag nanoparticles at room temperature and left for 48 hours before measurement. (f), Raman spectra measured for reference sample without Ag nanoparticles. The concentration of pMA is 2.5 mM. A large excitation power (3 mW) and long integration time (20 s) are used in order to obtain observable Raman signal.**

The demonstrated high SERS enhancement could be advantageous in applications that require sensing analytes at low concentrations. To quantify the performance of our controllable platform, the SERS spectra of pMA solutions with concentrations ranging from 100 μM to 10 nM are

measured (Figure 8-9(a)-(e)). Similar to Figure 8-5(b), Raman intensity increases with trapping time due to the formation of large Ag nanoparticle aggregations. The Raman intensities for the pMA samples with lower concentrations are smaller, even with the larger Ag aggregations that result from the longer trapping times employed. In the higher concentration samples, the pMA molecules cover a large fraction of the surface area of the trapped Ag nanoparticles, leading to a larger Raman signal. We successfully detect pMA molecules with concentrations down to 10 nM. We also measure a reference sample with 2.5 mM pMA molecule that does not contain any Ag nanoparticles (Figure 8-9(f)). Using these results, we calculate the analytical enhancement factor (AEF) using[117]:

$$AEF = \frac{I_{SERS}/c_{SERS}}{I_R/c_R} \tag{8.6}$$

where $I_{SERS}$ and $C_{SERS}$ are the measured Raman intensity and concentration, respectively, for the SERS sample. Similarly, $I_R$ and $C_R$ are the intensity and concentration, respectively, for the reference sample. Using the data for the 10 nM and reference samples (Figure 8-9(e)-(f)), the AEF is found to be $5 \times 10^5$, a value comparable to that achieved by SERS substrates consisting of aggregates of colloidal Ag nanoparticles[117], [120].

### *8.4.6 SERS measurements on different analytes*

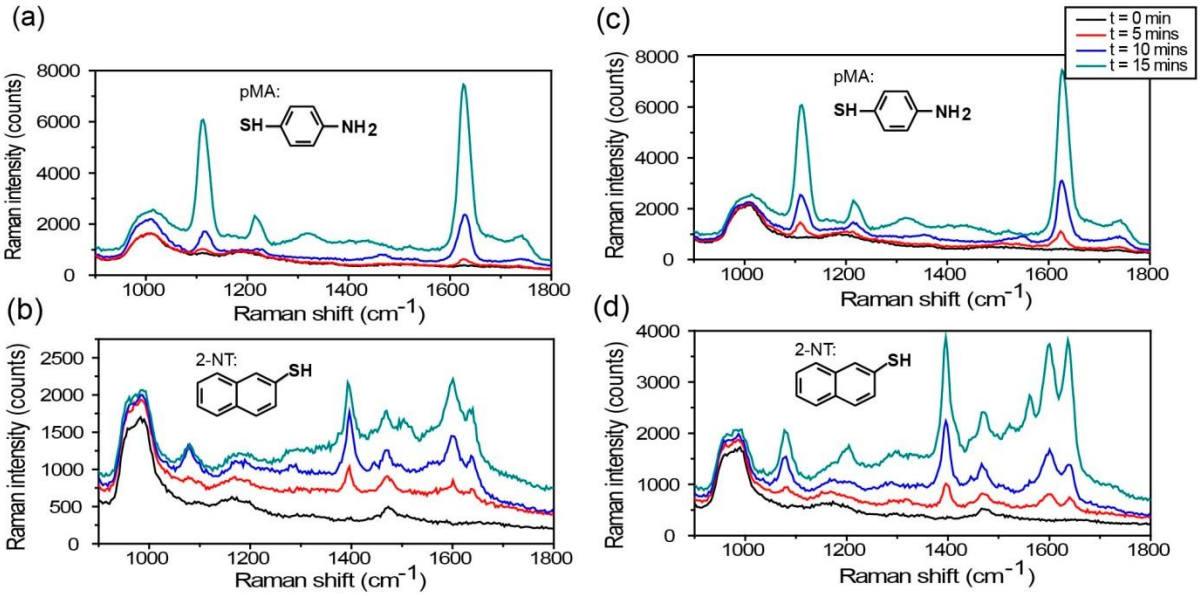


**Figure 8-10 Raman spectra measured when alternately injecting pMA and 2-NT samples into the chip. Insets show chemical structure of corresponding molecule. (a) and (c) Raman spectra measured for pMA molecule samples. (b) and (d) Raman spectra measured for 2-NT molecule samples.**

The ability of our approach to generate SERS hotspots on demand in a highly controllable manner presents the exciting opportunity for the detection of multiple analytes. To demonstrate this, we perform an experiment where we inject pMA and 2-NT solutions to the chip in an alternating fashion. Figure 8-10 shows that when each type of analyte is injected, only its corresponding SERS peaks are observed. Both pMA and 2-NT molecules are mixed with Ag nanoparticles and incubated for 24 hours before measurement. The pMA sample is first injected into channel and SERS spectra are measured after turning on trapping laser for 0, 5, 10 and 15

minutes. The results are then shown as Figure 8-10a. The chip is then cleaned by flushing it with de-ionized (DI) water. Following this cleaning step, 2-NT is injected and SERS measurements are performed under same conditions, with the results shown as Figure 8-10b. This process is repeated, with results shown as Figures 8-10(c) and (d). The concentrations for both pMA and 2-NT are 1 mM. The laser power for SERS excitation is 3 mW and spectrometer integration time is 5 s. The results confirm the ability of the device to produce a SERS hotspot that can be continually replenished by trapping new nanoparticles. Indeed, we confirm that, by keeping the trapping power low enough to prevent nanoparticles from sticking to the surface irreversibly, the device can be used for days.

In our approach, the field distributions produced by a photonic crystal cavity generates an optical trapping potential. For a given number of nanoparticles, there will be a configuration that minimizes the potential energy. The nanoparticles will ideally be trapped into this configuration. The presence of Brownian motion and fluctuations due to other factors, such as unintentional fluid flow due to instabilities in the microfluidic channel, in practice means that there is some uncertainty in the precise configuration into which the nanoparticles are trapped. Our method, nonetheless, presents an opportunity for nanoparticle clusters for SERS to be formed in a highly reproducible manner since their formation is guided by optical forces, rather than occurring in a random fashion *via* salt-induced aggregation. We furthermore note that the cluster formation is monitored in real-time. We anticipate that the engineering of photonic crystal cavities to produce trapping potentials that trap nanoparticles into pre-defined favorable configurations in a very precise manner would be an exciting direction for future research.

## 8.5 Summary

In conclusion, we demonstrate a controllable and reusable SERS platform using Ag nanoparticles optically trapped by an on-chip photonic crystal cavity. The nanoparticle aggregations are assembled in a highly reproducible fashion that can be monitored by measuring the resonance shift of the cavity. The nanoparticles can be released after a SERS measurement is made by turning off the trapping laser. We demonstrate SERS performance (analytical enhancement factor) that is on par with current approaches based on the salt-induced aggregation of Ag colloids, but that has the advantage of the aggregates being assembled controllably. We anticipate that this work could open a new paradigm for reusable SERS sensors, particularly for the sensing of multiple species in applications for which intervention to replace the SERS substrate is impractical. More generally, however, it presents a means for assembling nanomaterials produced in solution (*e.g.* quantum dots or plasmon nanoparticles) on a chip in a highly controllable manner.

# Chapter 9 Compact polarization splitter

In this chapter, we demonstrate an ultra-compact polarization splitter design that leverages the giant birefringence of silicon-on-insulator slot waveguides. A structure similar to the particle sorter of Chapter 5 is used. The fabricated splitter device has a coupling length of only 13.6 μm, and shows average polarization extinction ratios of 21 dB and 17 dB for the TE and TM polarizations respectively over the entire C-band.

## 9.1 Introduction

As the footprint of integrated photonic devices continues to shrink towards the sub-wavelength scale, polarization dependent dispersion and loss become increasingly significant due to geometric birefringence. The dependence of device characteristics on polarization presents a major challenge to photonic circuit design and operation, since light input to the chip from optical fibers is usually randomly polarized. A promising solution to this issue involves splitting the input light into TE/TM components for separate processing or subsequent polarization conversion [121]. Therefore, on-chip optical polarization splitting is a key function for realizing polarization-transparent operation in integrated photonic circuits.

Several methods have been demonstrated for on-chip polarization splitting to date. Efficient polarization splitting has been realized by mode evolution, although the near-adiabatic design

requires a long optical path length and hence large device footprint (~ 200 μm)[122]. Polarization splitting based on waveguide birefringence properties has also been demonstrated in III-V and silicon-on-insulator (SOI) waveguides[123–125]. The typical lengths of these structures are between 20 to 600 μm. The polarization splitting ratio of such devices critically depends on the waveguide birefringence, *i.e.* the effective index difference between the TE and TM polarizations. Since most semiconductor waveguide materials have little material birefringence, the waveguide birefringence almost entirely originates from structural asymmetry between the in-plane and out-of-plane transverse directions. In conventional rib or channel waveguide configurations, however, the attainable waveguide birefringence is limited by the waveguide cross-sectional aspect ratio, which is often otherwise determined by practical processing and application requirements. To circumvent this challenge, we introduce an additional design degree of freedom by etching a vertical nano-slot in the waveguides[74]. Strong optical confinement of the in-plane electric field component in the low refractive index nano-slot gives rise to a quasi-TE mode (the major electric field component is in the in-plane direction, *i.e.* parallel to the substrate) and leads to dramatically reduced effective index and hence large waveguide birefringence. The nano-slot also slightly modifies the field distribution of the TM mode. For simplicity, TE and TM modes in the following refer the quasi-TE and quasi-TM mode, respectively. Indeed, it has been shown that giant birefringence (polarization-dependent group index difference $n_g > 1.5$) can be achieved in slot waveguides[126] and that this can be used for polarization-independent directional coupling[127], [128].

## 9.2 Design

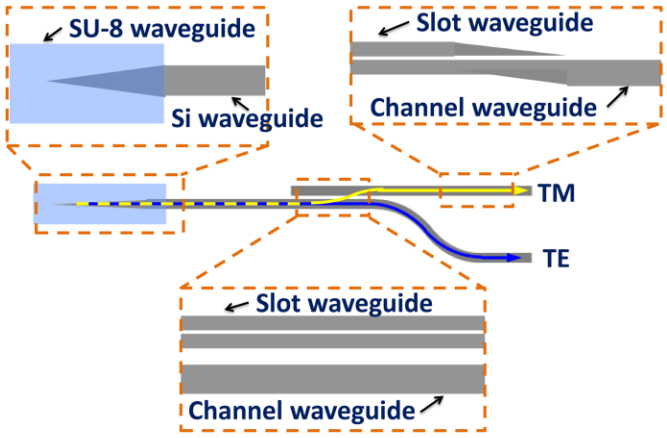


**Figure 9-1. Top view schematic diagram of slot waveguide polarization splitter (not to scale). Insets: fiber-waveguide coupler, slot-to-channel directional coupler and slot-channel mode converter.**

Figure 9-1 shows a top view schematic of the polarization splitter device. It consists of a fiber-waveguide coupler for efficient channeling of the mixed-polarization light from an optical fiber to a single mode silicon channel waveguide, a directional coupler section where a slot waveguide and a channel waveguide are placed in close proximity to allow selectively coupling of only TM polarization into the slot waveguide port, and a low-loss slot-to-channel mode converter[129] at the output section of the slot waveguide port. Therefore, only a short slot waveguide section is incorporated in the design, which minimizes the use of the very high resolution lithography necessary for slot fabrication. Since the slot concentrates optical power density through the electric field component discontinuity at the interface, this effect is highly polarization-selective. In Figure 9-2(a-d), plots are given of the optical mode profile (power

density) for TE and TM modes in channel and slot waveguides. The TE polarization experiences strong field enhancement in the slot as can be seen by comparing Figure 9-2a and 2c. By contrast, comparison of Figure 9-2b and 2d reveals that the TM mode remains almost unmodified after the introduction of the slot. The slot field concentration results in significant reduction of TE mode effective index as compared to that of the channel waveguide mode (Figure 9-2e). As a consequence, the effective index difference creates large phase mismatch that prevents power transfer of the TE mode from the channel waveguide input port to the slot waveguide output port. On the other hand, the TM mode can evanescently couple into the slot waveguide. In this way, efficient polarization splitting is realized.

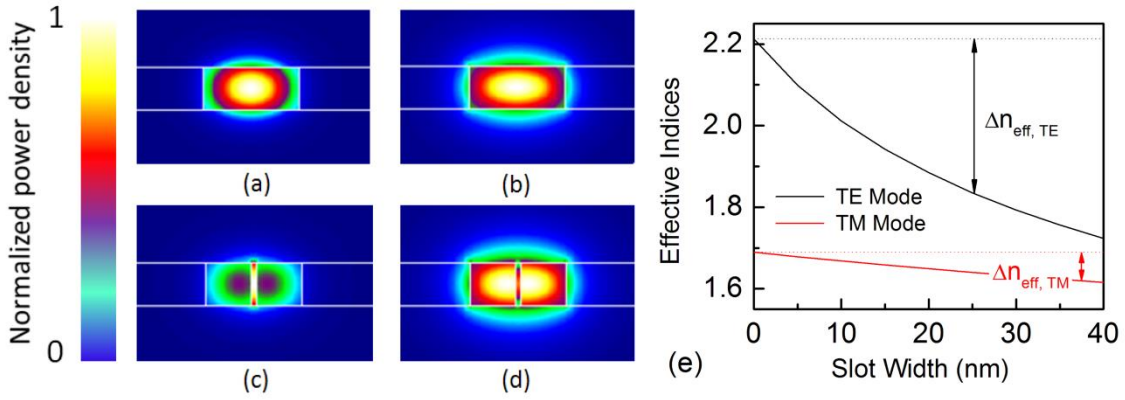


**Figure 9-2. Optical mode profile (power density) at a wavelength of 1550 nm in oxide-cladding channel/slot SOI waveguides with a width of 400 nm and a height of 220 nm (simulated using a finite-difference mode solver): (a) channel waveguide TE mode; (b) channel waveguide TM mode; (c) slot waveguide TE mode (20 nm slot width); (d) slot waveguide TM mode (20 nm slot width); (e) effective indices of slot waveguide modes plotted as functions of the slot width, showing the much stronger impact of slot addition on the TE mode ($\Delta n_{eff,\,TE} >> \Delta n_{eff,\,TM}$).**

Here, we present the design and experimental demonstration of a compact polarization splitter. The slot waveguide has a width of 450 nm. A slot width of 50 nm is chosen since even narrower slots, though favorable to increase TM mode extinction ratio of our device, would be difficult to fabricate with high yield. Consequently, the channel waveguide width is decreased slightly (420 nm) to compensate for the TM mode effective index mismatch due to the large slot width. The channel and slot waveguides are separated by a gap of 400 nm in the coupling region. A short coupling length of only 13.6 μm is used in the design, which qualifies our device as one of the most compact polarization splitters ever demonstrated. Decreasing the gap between channel and slot waveguide could further reduce the coupling length, and the footprint of the proposed polarization splitter.

## 9.3 Experimental demonstration

### *9.3.1 Fabrication*

As a proof-of-concept, a splitter device based on the previous design is fabricated on a silicon-on-insulator wafer with a 220 nm thick Si layer and 3 μm thick buried oxide. This is performed using electron beam lithography and reactive ion etching. Hydrogen silsesquioxane (HSQ) is used as the e-beam resist because of its high resolution and negative tone. Smooth and vertical sidewalls are achieved using hydrogen bromide (HBr) gas as the Si etchant. Figure 9-3(a) shows a scanning electron microscope top-view image of the fabricated coupler section. Fiber

couplers are incorporated at both ends of the waveguides[130]. These comprise SU-8 waveguides, each having a cross-section of 2 × 2 μm, that are designed to overlap with the inverse tapers of the Si channel waveguides to guarantee similar coupling coefficients for both TE and TM polarized light.

### *9.3.2 Measurement*

Optical transmission characteristics of the device are tested using a fiber end-fire technique. Transmission spectra of the device are measured using a C-band tunable laser and are plotted in Figure 9-3(b). The average ER across the C-band of TM and TE polarizations are 7 dB and 20 dB, respectively. The measured ER for the TM polarization is lower than that for TE. This is due to fabrication error associated with waveguide width control, as variations in waveguide width translate to effective index deviation and phase mismatch which results in incomplete power transfer to the TM output port. To compensate for the fabrication error, devices are fabricated with a bend (2.2 μm radius of curvature) in the TE port right after the coupling region, which helps remove the residual TM polarized light as it experiences larger bending loss. Measured transmission spectra in Figure 9-3(c) show the improved average ERs of 17 dB and 21 dB for TM and TE modes, respectively. Further improvement in the device performance approaching the theoretical predictions is anticipated with optimized fabrication and characterization.

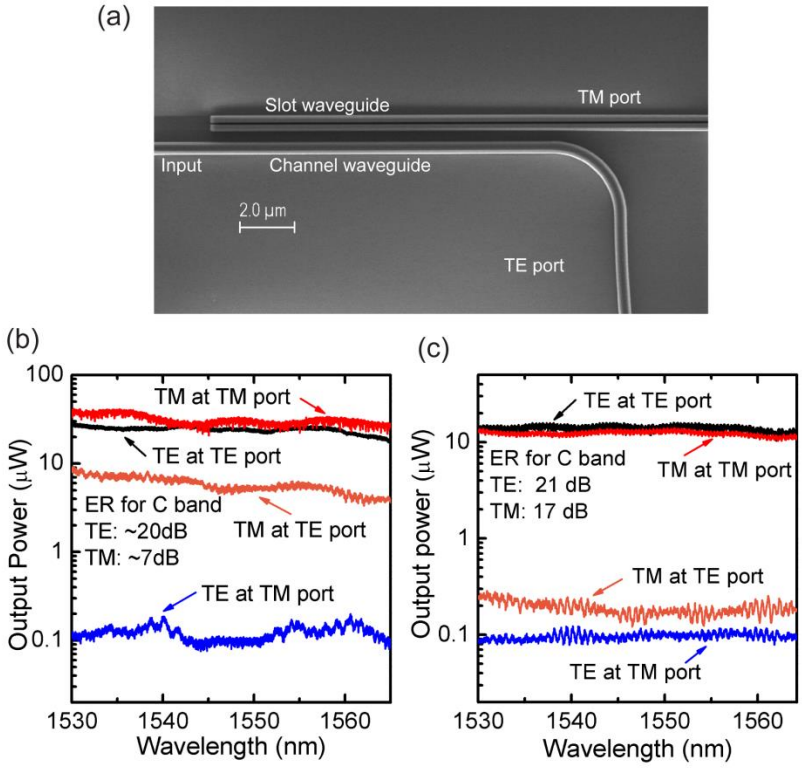


**Figure 9-3. (a)Top-view image of the fabricated splitter device showing the coupler section, (b,c) Transmission spectra of the splitter device from both TE and TM ports measured with a single input polarization of TM and TE for the structure (b) without sharp bend; (c) with a 2.2 μm bend in the TE port.**

## 9.4 Summary

In conclusion, we design, fabricate and characterize an ultra-compact polarization splitter utilizing the birefringence of a slot waveguide. Since the birefringence properties in slot waveguides are dictated by the electric field boundary conditions and are thus almost independent of wavelength, the theory predicts that low insertion loss (< 0.8 dB) and high

extinction ratios (25 dB and 60 dB for TM and TE polarizations, respectively) can be achieved over the 1520 – 1570 nm wavelength range. The fabricated splitter device has a coupling length of only 13.6 μm, and shows polarization extinction ratios of 21 dB and 17 dB for the TE and TM polarizations respectively over the entire C-band. The slot waveguide polarization splitter device could be applied for constructing polarization-transparent circuits and, as demonstrated in Chapter 5, could also constitute a basic building block for high-throughput opto-mechanical particle sorting systems based on optical forces.

# Chapter 10 Summary and future work

## 10.1 Summary

In this dissertation, we summarize our work on the developments of on-chip optical manipulation and sensing devices using silicon photonic structures. Waveguide-coupled planar structures are fabricated on a SOI chip by a microfabrication process that employs e-beam lithography and dry etching. Microcavities including microrings and photonic crystal cavities are used to trap both polystyrene and metallic particles with enhanced optical forces and precise position control due to the highly confined optical field in the cavities. The waveguide-based nature of our approach enables the integration of multiple devices to form a multifunctional micromanipulation system. Functionalities including trapping, delivery, buffering, and sorting have been demonstrated in our work. Microcavities are also a promising candidate for high sensitivity on-chip sensing. We have demonstrated trapping-assisted sensing techniques. The optical forces help trap the target analytes, and the resonance shifts are used to monitor the trapped objects. The controllable loading and release of samples is achieved *via* the trapping laser, which makes our sensors highly reusable. The self-alignment of the trapped objects with the optical field also improves the reproducibility of the sensing signal.

### *10.1.1 Optical manipulation using microcavities*

In Chapter 2-5, we demonstrate optical trapping, buffering and sorting using silicon photonic

devices. The waveguide-coupled devices make it possible to integrate multiple devices on a chip to achieve a multifunctional micromanipulation system.

In Chapter 2, we first demonstrate optical tapping using microring resonators. Once trapped on a micro-ring, a particle can be confined in an optical potential with a depth of 25 $k_BT$ over the entire microring's circumference. The particles are propelled around the microring at hundreds of micrometers per second, producing periodic revolutions at a few Hertz. A 5-8 times enhancement of the optical force is measured for the microring compared to the straight waveguide. An accurate position confinement of 50 nm has been measured for the trapped particles.

In Chapter 3, we then demonstrate two particle buffer chains with which it is possible to store, switch and deliver single particles. The buffer chains consist of two Si microrings of the type that are used to trap and release sub-micrometer particles in Chapter 2. By changing the wavelength of the laser input to the chip, particles can be switched from one ring to the other, traveling between them on the waveguide.

In Chapter 4, we design a 1D photonic crystal cavity for optical trapping, and demonstrate that it

works. We first numerically simulate a novel 1D photonic crystal cavity that combines a photonic crystal waveguide cavity with a nanoslot structure. These simulations indicate a~1300 times enhancement of the optical gradient trapping force of this device, compared to a conventional waveguide trapping device. Using a photonic crystal cavity, we experimentally demonstrate the trapping of polystyrene particle with diameters from 110 nm to 2 μm, and silver nanoparticle with diameter of 80 nm.

In Chapter 5, we demonstrate a novel approach to particle sorting that makes use of a 3-dB optical splitter whose outputs comprise a CWG and a SWG. We experimentally prove that this device enables the sorting of particles with diameters of 2 μm and 320 nm. Because the laser power used in this device is 1-2 orders of magnitude smaller than used in previous optical force-based particle sorting methods. This is mainly due to the fact that the device geometry is such that the particles need to be displaced by a small distance to be switched between output ports. The passive nature of this device and its low power operation, present interesting opportunities for various lab-on-a-chip applications.

### *10.1.2 Trapping-assisted optical sensing techniques*

In Chapter 6-8, we apply our on-chip micromanipulation system for optical sensing. The resonance shift of the microcavities is used to detect and monitor the trapped particles. By

integrating the trapping and sensing using a two-laser measurement setup, we demonstrate several reusable trapping-assisted sensors with improved reproducibility.

In Chapter 6, we demonstrate nanoparticle sensing using both a microdonut and a 1D photonic crystal cavity. Our system is capable of monitoring the trapping of particles *in situ* by continuously scanning the probe laser around the resonance frequency. Particles with diameters from 110 nm to 2 μm are trapped and detected using our trapping-assisted sensing technique. Optical trapping reduces the transportation time and provides an effective way to load and release the targeted objects without involving additional cleaning processes.

In Chapter 7, we apply our trapping and sensing system for protein sensing based on a binding assay. Instead of directly trapping and detecting the molecules, we use polystyrene particles with diameter of 320 nm as carriers, which are coated with antibodies of the target molecules (GFP molecules). Our system can quantitatively analyze the GFP samples by detecting the particle clusters induced by the molecules. Unlike other cavity-based biosensors, which use biological interactions to selectively bind the target molecules to the surface, our devices uses optical forces to load the samples and therefore can be reused without complex cleaning processes.

In Chapter 8, we demonstrate a controllable and reusable SERS platform in which Ag nanoparticles are optically trapped by an on-chip photonic crystal cavity. The formation of nanoparticle aggregates is observed by monitoring the resonance shift of the cavity. Enhanced

Raman signal from molecules on the surface of the Ag nanoparticles is been detected. Our optical trapping based SERS platform provides the flexibility to form surface-enhanced hotspots in a controllable manner. We anticipate that this work could open a new paradigm for reusable SERS sensors, particularly for the sensing of multiple species in applications for which intervention to replace the SERS substrate is impractical. We furthermore believe that the implications of this work extend much more generally beyond SERS, presenting an opportunity for the controlled assembly (and release) of fluid-borne nanomaterials (*e.g.* quantum dots or possibly biological materials such as virus particles) on a chip.

### *10.1.3 Polarization splitter for optical communication*

In Chapter 9, we design, fabricate and characterize an ultra-compact polarization splitter utilizing the birefringence of a slot waveguide. The highly confined electric field in the slot that arises from boundary conditions gives rise to a large birefringence. Low insertion loss, small footprint and high extinction ratio can be therefore achieved in a broadband manner. Our fabricated splitter device has a coupling length of only 13.6 μm, and shows polarization extinction ratios of 21 dB and 17 dB for the TE and TM polarizations respectively over the entire C-band. The compact on-chip slot waveguide polarization splitter device can be easily integrated with other photonic devices and applied for constructing polarization-transparent circuits.

## 10.2 Future work

### *10.2.1 Optimization of cavities for high performance optical trapping*

Although we have been able to trap and detect polystyrene particles down to 110 nm, the devices could be further optimized to trap and detect even smaller particles by designing high-Q, small mode volume cavities. In our current measurement setup, the absorption of water at 1550 nm prevents us from achieving higher *Q*s, the heat generated from the absorption of water also introduces additional noise to the sensing results. Changing to an operation wavelength that is not absorbed by the water could eliminate these problems and provide a larger optical force and higher sensitivity.

### *10.2.2 Sensitivity improvement for trapping-assisted sensing*

Further sensitivity enhancement could be achieved by using plasmonic structures[131]. Plasmonic structures such gold nanoparticles are promising candidates for biosensing due to the large peak shift that results from changes to the refractive index of the surrounding medium[132]. Sub-100 nm metallic particle can provide an extremely high field enhancements[119], [133]. However, the quality factor of the plasmonic resonance is usually below ~100 because of absorption losses, which limits the sensitivity of plasmonic biosensors. Photonic-plasmonic hybrid structures are a promising solution that combines the advantages of both plasmonic and photonic devices. Several groups have reported enhanced sensing using different geometrics[134], [135]. The target objects located in the vicinity of the plasmonic structures could introduce an enhanced resonance shift to the photonic cavity. Our experience in high

performance plasmonic nano-antenna could assist us with the design of next generation photonic-plasmonic hybrid trapping and sensing system.

### *10.2.3 Integration for a multifunctional micromanipulation and sensing system*

Integrating multiple devices on one chip could lead to a more sophisticated optical manipulation and sensing system. We demonstrate different functionalities including trapping, delivery, buffering, sorting and sensing. Future work could involve increased levels of integration and the realization of a multifunctional system.

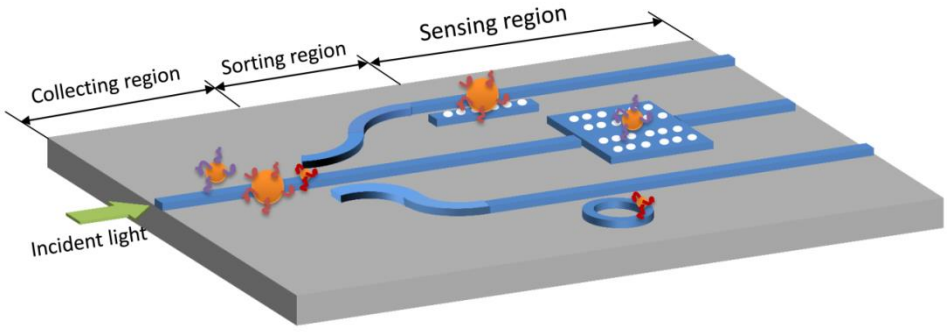


**Figure 10-1 Schematic diagram of the trapping and sensing system**

Figure 10-1 shows the schematic diagram of a possible system based on silicon nitride devices. The sample to be characterized would be mixed with nanoparticles coated with antibodies. The particles could be dielectric or metallic particles, depending on the sensing mechanism employed. The target molecules from the sample would bind to their corresponding antibodies on the nanoparticles. Each type of antibody would be attached to a nanoparticle of a certain size. The

nanoparticles functioning as molecule carriers would be trapped onto the waveguide in the collecting region when they come close to the vicinity of the device. The particles would then be sorted into different channels based on their size, using our recently demonstrated waveguide-based passive sorter. Different particles would then be delivered to the biosensors in each channel. The molecule coated nanoparticles would introduce a resonance shift that is different from what introduced by the nanoparticles without molecules on the surface. Measuring the transmission spectra would tell us whether targeted molecules exist in the sample. High sensitivity biosensors as discussed in section 10.2.2 could be used.

## References


[1] M. Paniccia and N. Photonics, “Integrating silicon photonics,” *Nature Photon.*, vol. 4, no. 8, pp. 498–499, Aug. 2010.

[2] R. Soref, “The Past, Present, and Future of Silicon Photonics,” *IEEE J. Sel. Topics in Quantum Electron.*, vol. 12, no. 6, pp. 1678–1687, Nov. 2006.

[3] J. E. Cunningham, I. Shubin, X. Zheng, T. Pinguet, A. Mekis, Y. Luo, H. Thacker, G. Li, J. Yao, K. Raj, and A. V Krishnamoorthy, “Highly-efficient thermally-tuned resonant optical filters.,” *Opt. Express*, vol. 18, no. 18, pp. 19055–63, Aug. 2010.

[4] G. T. Reed, G. Mashanovich, F. Y. Gardes, and D. J. Thomson, “Silicon optical modulators,” *Nature Photon.*, vol. 4, no. 8, pp. 518–526, Jul. 2010.

[5] L. Chen, K. Preston, S. Manipatruni, and M. Lipson, “Integrated GHz silicon photonic interconnect with micrometer-scale modulators and detectors.,” *Opt. Express*, vol. 17, no. 17, pp. 15248–56, Aug. 2009.

[6] N.-N. Feng, S. Liao, D. Feng, P. Dong, D. Zheng, H. Liang, R. Shafiiha, G. Li, J. E. Cunningham, A. V Krishnamoorthy, and M. Asghari, “High speed carrier-depletion modulators with 1.4V-cm V(pi)L integrated on 0.25microm silicon-on-insulator waveguides.,” *Opt. Express*, vol. 18, no. 8, pp. 7994–9, Apr. 2010.

[7] L. Chen and M. Lipson, “Ultra-low capacitance and high speed germanium photodetectors on silicon.,” *Opt. Express*, vol. 17, no. 10, pp. 7901–6, May 2009.

[8] J. Michel, J. Liu, and L. C. Kimerling, “High-performance Ge-on-Si photodetectors,” *Nature Photon.*, vol. 4, no. 8, pp. 527–534, Jul. 2010.

[9] H. Rong, S. Xu, O. Cohen, O. Raday, M. Lee, V. Sih, and M. Paniccia, “A cascaded silicon Raman laser,” *Nature photonics*, vol. 2, no. 3, pp. 170–174, 2008.

[10] D. Liang and J. E. Bowers, “Recent progress in lasers on silicon,” *Nature Photon.*, vol. 4, no. 8, pp. 511–517, Jul. 2010.

[11] H. Rong, S. Xu, Y.-H. Kuo, V. Sih, O. Cohen, O. Raday, and M. Paniccia, “Low-threshold continuous-wave Raman silicon laser,” *Nature Photon.*, vol. 1, no. 4, pp. 232–237, 2007.

[12] J. Leuthold, C. Koos, and W. Freude, “Nonlinear silicon photonics,” *Nature Photon.*, vol. 4, no. 8, pp. 535–544, Jul. 2010.

[13] S. Lin, E. Schonbrun, and K. Crozier, “Optical manipulation with planar silicon microring resonators.,” *Nano Lett.*, vol. 10, no. 7, pp. 2408–2411, Jul. 2010.

[14] T. Yoshie, L. Tang, and S.-Y. Su, “Optical Microcavity: Sensing down to Single Molecules and Atoms,” *Sensors*, vol. 11, no. 2, pp. 1972–1991, Feb. 2011.

[15] Y. Sun and X. Fan, “Optical ring resonators for biochemical and chemical sensing.,” *Anal. Bioanal. Chem.*, vol. 399, no. 1, pp. 205–211, Jan. 2011.

[16] S. Arnold, D. Keng, S. I. Shopova, S. Holler, W. Zurawsky, and F. Vollmer, “Whispering Gallery Mode Carousel--a photonic mechanism for enhanced nanoparticle detection in biosensing.,” *Opt. Express*, vol. 17, no. 8, pp. 6230–6238, Apr. 2009.

[17] S. Mandal and D. Erickson, “Nanoscale optofluidic sensor arrays.,” *Opt. Express*, vol. 16, no. 3, pp. 1623–1631, Feb. 2008.

[18] L. M. Bellan, D. Wu, and R. S. Langer, “Current trends in nanobiosensor technology.,” *Wiley interdisciplinary reviews. Nanomedicine and nanobiotechnology*, vol. 3, no. 3, pp. 229–46, 2011.

[19] A. Ashkin, J. Dziedzic, J. Bjorkholm, and S. Chu, “Observation of a single-beam gradient force optical trap for dielectric particles,” *Opt. Lett.*, vol. 11, no. 5, p. 288, 1986.

[20] S. Kawata and T. Tani, “Optically driven Mie particles in an evanescent field along a channeled waveguide,” *Opt. Lett.*, vol. 21, pp. 1768–1770, 1996.

[21] S. Gaugiran, S. Gétin, J. M. Fedeli, G. Colas, A. Fuchs, F. Chatelain, and J. Dérouard, “Optical manipulation of microparticles and cells on silicon nitride waveguides,” *Opt. Express*, vol. 13, no. 18, p. 6956, 2005.

[22] J. Hole, J. Wilkinson, K. Grujic, and O. Hellesø, “Velocity distribution of Gold nanoparticles trapped on an optical waveguide.,” *Opt. Express*, vol. 13, no. 10, pp. 3896–901, May 2005.

[23] K. Wang, E. Schonbrun, P. Steinvurzel, and K. B. Crozier, “Scannable plasmonic trapping using a gold stripe.,” *Nano Lett.*, vol. 10, no. 9, pp. 3506–11, Sep. 2010.

[24] A. Rahmani and P. C. Chaumet, “Optical trapping near a photonic crystal.,” *Opt. Express*, vol. 14, no. 13, pp. 6353–8, Jun. 2006.

[25] M. L. Juan, R. Gordon, Y. Pang, F. Eftekhari, and R. Quidant, “Self-induced back-action optical trapping of dielectric nanoparticles,” *Nature Phys.*, vol. 5, no. 12, pp. 915–919, 2009.

[26] P. M. Hansen, V. K. Bhatia, N. Harrit, and L. Oddershede, “Expanding the optical trapping range of gold nanoparticles.,” *Nano Lett.*, vol. 5, no. 10, pp. 1937–42, Oct. 2005.

[27] T. Lu, H. Lee, T. Chen, S. Herchak, J.-H. Kim, S. E. Fraser, R. C. Flagan, and K. Vahala, “High sensitivity nanoparticle detection using optical microcavities.,” *Proc. Natl. Acad. Sci. U. S. A.*, vol. 108, no. 15, pp. 5976–5979, Apr. 2011.

[28] K. De Vos, J. Girones, S. Popelka, E. Schacht, R. Baets, and P. Bienstman, “SOI optical microring resonator with poly(ethylene glycol) polymer brush for label-free biosensor applications.,” *Biosensors & bioelectronics*, vol. 24, no. 8, pp. 2528–33, Apr. 2009.

[29] F. Vollmer and S. Arnold, “Whispering-gallery-mode biosensing: label-free detection down to single molecules,” *Nature Methods*, vol. 5, no. 7, pp. 591–596, Jul. 2008.

[30] A. Yariv, “Universal relations for coupling of optical power between microresonators and dielectric waveguides,” *Electronics Letters*, vol. 36, no. 4, pp. 321–322, 2000.

[31] D. G. Grier, “A revolution in optical manipulation.,” *Nature*, vol. 424, no. 6950, pp. 810–6, Aug. 2003.

[32] A. B. Stilgoe, T. A. Nieminen, G. Knöener, N. R. Heckenberg, and H. Rubinsztein-Dunlop, “The effect of Mie resonances on trapping in optical tweezers,” *Opt. Express*, vol. 16, no. 19, pp. 15039–15051, 2008.

[33] H. Felgner, O. Muller, and M. Schliwa, “Calibration of light forces in optical tweezers,” *Applied Optics*, vol. 34, no. 6, pp. 977–982, 1995.

[34] H. Zhang and K.-K. Liu, “Optical tweezers for single cells.,” *Journal of the Royal Society, Interface / the Royal Society*, vol. 5, no. 24, pp. 671–90, 2008.

[35] J. Curtis and D. Grier, “Structure of Optical Vortices,” *Phys. Rev. Lett.*, vol. 90, no. 13, pp. 13–16, Apr. 2003.

[36] V. Garcés-Chávez, D. McGloin, M. Padgett, W. Dultz, H. Schmitzer, and K. Dholakia, “Observation of the Transfer of the Local Angular Momentum Density of a Multiringed Light Beam to an Optically Trapped Particle,” *Phys. Rev. Lett.*, vol. 91, no. 9, pp. 1–4, Aug. 2003.

[37] M. P. MacDonald, G. C. G. Spalding, and K. Dholakia, “Microfluidic sorting in an optical lattice.,” *Nature*, vol. 426, no. 6965, pp. 421–4, Nov. 2003.

[38] E. Schonbrun, R. Piestun, P. Jordan, J. Cooper, K. Wulff, J. Courtial, and M. Padgett, “3D interferometric optical tweezers using a single spatial light modulator.,” *Optics express*, vol. 13, no. 10, pp. 3777–86, May 2005.

[39] E. F. Nichols and G. F. Hull, “The Pressure Due to Radiation,” *Proceedings of the American Academy of Arts and Sciences*, vol. 38, no. 20, pp. 559–599, 1903.

[40] P. News, C. Hermann, and H. D. Waveplates, “40 Years of optical manipulation,” *Optics & Photonics News*, vol. 21, no. 3, 2010.

[41] K. Wang and K. B. Crozier, “Plasmonic trapping with a gold nanopillar.,” *Chemphyschem : a European journal of chemical physics and physical chemistry*, vol. 13, no. 11, pp. 2639–48, Aug. 2012.

[42] B. Kemp, T. Grzegorczyk, and J. Kong, “Optical Momentum Transfer to Absorbing Mie Particles,” *Phys. Rev. Lett.*, vol. 97, no. 13, pp. 1–4, 2006.

[43] B. A. Kemp, T. M. Grzegorczyk, and J. A. Kong, “Ab initio study of the radiation pressure on dielectric and magnetic media,” *Opt. Express*, vol. 13, no. 23, p. 9280, Nov. 2005.

[44] B. S. Schmidt, A. H. Yang, D. Erickson, and M. Lipson, “Optofluidic trapping and transport on solid core waveguides within a microfluidic device.,” *Opt. Express*, vol. 15, no. 22, pp. 14322–34, Oct. 2007.

[45] B. S. Ahluwalia, P. McCourt, T. Huser, and O. G. Hellesø, “Optical trapping and propulsion of red blood cells on waveguide surfaces.,” *Opt. Express*, vol. 18, no. 20, pp. 21053–61, Sep. 2010.

[46] K. Grujic and O. G. Hellesø, “Dielectric microsphere manipulation and chain assembly by counter-propagating waves in a channel waveguide.,” *Optics express*, vol. 15, no. 10, pp. 6470–7, May 2007.

[47] K. Grujic, O. Hellesø, J. Hole, and J. Wilkinson, “Sorting of polystyrene microspheres using a Y-branched optical waveguide,” *Opt. Express*, vol. 13, pp. 1–7, 2005.

[48] A. H. J. Yang, T. Lerdsuchatawanich, and D. Erickson, “Forces and transport velocities for a particle in a slot waveguide.,” *Nano Lett.*, vol. 9, no. 3, pp. 1182–8, Mar. 2009.

[49] N. Suwanpayak, M. A. Jalil, C. Teeka, J. Ali, and P. P. Yupapin, “Optical vortices generated by a PANDA ring resonator for drug trapping and delivery applications,” *Biomedical Optics Express*, vol. 2, no. 1, pp. 159–168, 2011.

[50] S. Mandal, X. Serey, and D. Erickson, “Nanomanipulation using silicon photonic crystal resonators.,” *Nano Lett.*, vol. 10, no. 1, pp. 99–104, 2010.

[51] S. Lin and K. B. Crozier, “Design of nanoslotted photonic crystal waveguide cavities for single nanoparticle trapping and detection,” *Opt. Lett.*, vol. 34, no. 21, pp. 3451–3453, 2009.

[52] X. Serey, S. Mandal, and D. Erickson, “Comparison of silicon photonic crystal resonator designs for optical trapping of nanomaterials.,” *Nanotechnology*, vol. 21, no. 30, p. 305202, Jul. 2010.

[53] M. Barth and O. Benson, “Manipulation of dielectric particles using photonic crystal cavities,” *Appl. Phys. Lett.*, vol. 89, no. 25, p. 253114, 2006.

[54] A. A. H. J. Yang and D. Erickson, “Optofluidic ring resonator switch for optical particle transport.,” *Lab Chip*, vol. 10, no. 6, pp. 769–74, Mar. 2010.

[55] M. R. Lee and P. M. Fauchet, “Nanoscale microcavity sensor for single particle detection.,” *Opt. Lett.*, vol. 32, no. 22, pp. 3284–3286, Nov. 2007.

[56] A. H. J. Yang, S. D. Moore, B. S. Schmidt, M. Klug, M. Lipson, and D. Erickson, “Optical manipulation of nanoparticles and biomolecules in sub-wavelength slot waveguides.,” *Nature*, vol. 457, no. 7225, pp. 71–5, Jan. 2009.

[57] W. N. Burnette, “‘Western Blotting’: Electrophoretic transfer of proteins from sodium dodecyl sulfate-polyacrylamide gels to unmodified nitrocellulose and radiographic detection with antibody and radioiodinated protein A,” *Anal. Biochem.*, vol. 112, no. 2, pp. 195–203, Apr. 1981.

[58] S. S. Varghese, Y. Zhu, T. J. Davis, and S. C. Trowell, “FRET for lab-on-a-chip devices - current trends and future prospects.,” *Lab Chip*, vol. 10, no. 11, pp. 1355–64, Jun. 2010.

[59] E. P. Y. Chiou, A. T. Ohta, Z. Li, and S. T. Wereley, “Optofluidics for Lab-on-a-Chip,” *Advances in OptoElectronics*, vol. 2012, pp. 1–2, 2012.

[60] H. Li and X. Fan, “Characterization of sensing capability of optofluidic ring resonator biosensors,” *Appl. Phys. Lett.*, vol. 97, no. 1, p. 011105, 2010.

[61] A. M. Armani, R. P. Kulkarni, S. E. Fraser, R. C. Flagan, and K. J. Vahala, “Label-free, single-molecule detection with optical microcavities.,” *Science (New York, N.Y.)*, vol. 317, no. 5839, pp. 783–7, Aug. 2007.

[62] S. Arnold, M. Khoshsima, I. Teraoka, S. Holler, and F. Vollmer, “Shift of whispering-gallery modes in microspheres by protein adsorption.,” *Opt. Lett.*, vol. 28, no. 4, pp. 272–274, Feb. 2003.

[63] J. Zhu, S. K. Ozdemir, Y.-F. Xiao, L. Li, L. He, D.-R. Chen, and L. Yang, “On-chip single nanoparticle detection and sizing by mode splitting in an ultrahigh-Q microresonator,” *Nature Photonics*, vol. 4, no. 1. Nature Publishing Group, pp. 46–49, Dec-2009.

[64] T. Chung, S.-Y. Lee, E. Y. Song, H. Chun, and B. Lee, “Plasmonic Nanostructures for Nano-Scale Bio-Sensing,” *Sensors*, vol. 11, no. 11, pp. 10907–10929, Nov. 2011.

[65] Q. Xu, B. Schmidt, S. Pradhan, and M. Lipson, “Micrometre-scale silicon electro-optic modulator,” *Nature*, vol. 435, no. 7040, pp. 325–327, 2005.

[66] L.-W. Luo, G. S. Wiederhecker, J. Cardenas, C. Poitras, and M. Lipson, “High quality factor etchless silicon photonic ring resonators,” *Opt. Express*, vol. 19, no. 7, p. 6284, Mar. 2011.

[67] A. Gondarenko, J. S. Levy, and M. Lipson, “High confinement micron-scale silicon nitride high Q ring resonator.,” *Optics express*, vol. 17, no. 14, pp. 11366–70, Jul. 2009.

[68] G. Stokes and D. Law, “Derivation of the stokes drag formula,” pp. 2–4, 1851.

[69] M. M. Wang, E. Tu, D. E. Raymond, J. M. Yang, H. Zhang, N. Hagen, B. Dees, E. M. Mercer, A. H. Forster, I. Kariv, P. J. Marchand, and W. F. Butler, “Microfluidic sorting of mammalian cells by optical force switching.,” *Nature Biotech.*, vol. 23, no. 1, pp. 83–7, Jan. 2005.

[70] G. Sinclair, P. Jordan, J. Courtial, M. Padgett, J. Cooper, and Z. Laczik, “Assembly of 3-dimensional structures using programmable holographic optical tweezers.,” *Opt. Express*, vol. 12, no. 22, pp. 5475–80, Nov. 2004.

[71] P. Y. Chiou, A. T. Ohta, and M. C. Wu, “Massively parallel manipulation of single cells and microparticles using optical images.,” *Nature*, vol. 436, no. 7049, pp. 370–2, Jul. 2005.

[72] H. Lee, Y. Liu, D. Ham, and R. M. Westervelt, “Integrated cell manipulation system--CMOS/microfluidic hybrid.,” *Lab Chip*, vol. 7, no. 3, pp. 331–7, Mar. 2007.

[73] A. Di Falco, C. Conti, and G. Assanto, “Quadratic phase matching in slot waveguides.,” *Opt. Lett.*, vol. 31, no. 21, pp. 3146–8, Nov. 2006.

[74] V. R. Almeida, Q. Xu, C. A. Barrios, and M. Lipson, “Guiding and confining light in void nanostructure,” *Opt. Lett.*, vol. 29, no. 11, pp. 1209–1211, 2004.

[75] Y. Akahane, T. Asano, B. S. Song, and S. Noda, “High-Q photonic nanocavity in a two-dimensional photonic crystal,” *Nature*, vol. 425, pp. 944–947, 2003.

[76] S. K. Mohanty, a Rapp, S. Monajembashi, P. K. Gupta, and K. O. Greulich, “Comet assay measurements of DNA damage in cells by laser microbeams and trapping beams with wavelengths spanning a range of 308 nm to 1064 nm.,” *Radiation research*, vol. 157, no. 4, pp. 378–85, Apr. 2002.

[77] M. Nieto-Vesperinas, P. C. Chaumet, and a Rahmani, “Near-field photonic forces.,” *Philosophical transactions. Series A, Mathematical, physical, and engineering sciences*, vol. 362, no. 1817, pp. 719–37, Apr. 2004.

[78] W. A. Bonner, “Fluorescence Activated Cell Sorting,” *Rev. Sci. Instrum.*, vol. 43, no. 3, p. 404, Dec. 1972.

[79] a Y. Fu, C. Spence, A. Scherer, F. H. Arnold, and S. R. Quake, “A microfabricated fluorescence-activated cell sorter.,” *Nature Biotech.*, vol. 17, no. 11, pp. 1109–11, Nov. 1999.

[80] S. Fiedler, S. G. Shirley, T. Schnelle, and G. Fuhr, “Dielectrophoretic Sorting of Particles and Cells in a Microsystem,” *Anal. Chem.*, vol. 70, no. 9, pp. 1909–1915, May 1998.

[81] A. Wolff, I. Perch-Nielsen, U. Larsen, and P. Friis, “Integrating advanced functionality in a microfabricated high-throughput fluorescent-activated cell sorter,” *Lab Chip*, 2003.

[82] E. Schonbrun and K. B. Crozier, “Spring constant modulation in a zone plate tweezer using linear polarization.,” *Opt. Lett.*, vol. 33, no. 17, pp. 2017–9, Sep. 2008.

[83] K. Wang, E. Schonbrun, and K. B. Crozier, “Propulsion of gold nanoparticles with surface plasmon polaritons: evidence of enhanced optical force from near-field coupling between gold particle and gold film.,” *Nano Lett.*, vol. 9, no. 7, pp. 2623–9, Jul. 2009.

[84] R. F. Marchington, M. Mazilu, S. Kuriakose, V. Garcés-Chávez, P. J. Reece, T. F. Krauss, M. Gu, and K. Dholakia, “Optical deflection and sorting of microparticles in a near-field optical geometry.,” *Opt. Express*, vol. 16, no. 6, pp. 3712–26, Mar. 2008.

[85] S.-K. Hoi, C. Udalagama, C.-H. Sow, F. Watt, and a. a. Bettiol, “Microfluidic sorting system based on optical force switching,” *Applied Physics B*, vol. 97, no. 4, pp. 859–865, Aug. 2009.

[86] R. W. Applegate, J. Squier, T. Vestad, J. Oakey, D. W. M. Marr, P. Bado, M. a Dugan, and A. a Said, “Microfluidic sorting system based on optical waveguide integration and diode laser bar trapping.,” *Lab Chip*, vol. 6, no. 3, pp. 422–6, Mar. 2006.

[87] S. Lin and K. B. Crozier, “An integrated microparticle sorting system based on near-field optical forces and a structural perturbation,” *Opt. Express*, vol. 20, no. 4, pp. 3367–3374, Jan. 2012.

[88] V. R. V. R. Almeida, R. R. R. Panepucci, and M. Lipson, “Nanotaper for compact mode conversion,” *Opt. Lett.*, vol. 28, no. 15, pp. 1302–1304, Aug. 2003.

[89] T. J. Kippenberg, “Microresonators: Particle sizing by mode splitting,” *Nature Photon.*, vol. 4, no. 1, pp. 9–10, Jan. 2010.

[90] L. He, S. K. Ozdemir, J. Zhu, W. Kim, and L. Yang, “Detecting single viruses and nanoparticles using whispering gallery microlasers.,” *Nature Nanotech.*, vol. 6, no. 7, pp. 428–432, Jul. 2011.

[91] R. Belda, J. V. Herraez, and O. Diez, “A study of the refractive index and surface tension synergy of the binary water/ethanol: influence of concentration,” *Phys. Chem. Liq.*, vol. 43, no. 1, pp. 91–101, Feb. 2005.

[92] J. Hu, S. Lin, L. Kimerling, and K. Crozier, “Optical trapping of dielectric nanoparticles in resonant cavities,” *Phys. Rev. A*, vol. 82, no. 5, pp. 1–8, Nov. 2010.

[93] S. Blair and Y. Chen, “Resonant-Enhanced Evanescent-Wave Fluorescence Biosensing with Cylindrical Optical Cavities,” *Applied Optics*, vol. 40, no. 4, p. 570, 2001.

[94] P. E. Sheehan and L. J. Whitman, “Detection limits for nanoscale biosensors.,” *Nano Lett.*, vol. 5, no. 4, pp. 803–807, Apr. 2005.

[95] T. M. Squires, R. J. Messinger, and S. R. Manalis, “Making it stick: convection, reaction and diffusion in surface-based biosensors.,” *Nature Biotech.*, vol. 26, no. 4, pp. 417–426, Apr. 2008.

[96] C. L. Haynes, A. D. McFarland, and R. P. Van Duyne, “Surface-Enhanced Raman Spectroscopy,” *Anal. Chem.*, vol. 77, no. 17, p. 338 A–346 A, Sep. 2005.

[97] I. Choi and Y. Choi, “Plasmonic Nanosensors: Review and Prospect,” *IEEE J. Sel. Topics in Quantum Electron.*, vol. 18, no. 3, pp. 1110–1121, May 2012.

[98] X. Zhang, M. a Young, O. Lyandres, and R. P. Van Duyne, “Rapid detection of an anthrax biomarker by surface-enhanced Raman spectroscopy.,” *J. Am. Chem. Soc.*, vol. 127, no. 12, pp. 4484–9, Mar. 2005.

[99] S. S. R. Dasary, A. K. Singh, D. Senapati, H. Yu, and P. C. Ray, “Gold nanoparticle based label-free SERS probe for ultrasensitive and selective detection of trinitrotoluene.,” *J. Am. Chem. Soc.*, vol. 131, no. 38, pp. 13806–12, Sep. 2009.

[100] M. Mulvihill, A. Tao, K. Benjauthrit, J. Arnold, and P. Yang, “Surface-Enhanced Raman Spectroscopy for Trace Arsenic Detection in Contaminated Water,” *Angewandte Chemie*, vol. 120, no. 34, pp. 6556–6560, Aug. 2008.

[101] M. Lin, L. He, J. Awika, L. Yang, D. R. Ledoux, H. Li, and a Mustapha, “Detection of melamine in gluten, chicken feed, and processed foods using surface enhanced Raman spectroscopy and HPLC.,” *Journal of food science*, vol. 73, no. 8, pp. T129–34, Oct. 2008.

[102] O. Lyandres, N. C. Shah, C. R. Yonzon, J. T. Walsh, M. R. Glucksberg, and R. P. Van Duyne, “Real-time glucose sensing by surface-enhanced Raman spectroscopy in bovine plasma facilitated by a mixed decanethiol/mercaptohexanol partition layer.,” *Analytical chemistry*, vol. 77, no. 19, pp. 6134–9, Oct. 2005.

[103] N. Leopold and B. Lendl, “A New Method for Fast Preparation of Highly Surface-Enhanced Raman Scattering (SERS) Active Silver Colloids at Room Temperature by Reduction of Silver Nitrate with Hydroxylamine Hydrochloride,” *The Journal of Physical Chemistry B*, vol. 107, no. 24, pp. 5723–5727, Jun. 2003.

[104] L. Rivas, S. Sanchez-Cortes, and J. Garcia-Ramos, “Growth of silver colloidal particles obtained by citrate reduction to increase the Raman enhancement factor,” *Langmuir*, no. 11, pp. 574–577, 2001.

[105] E. D. Diebold, N. H. Mack, S. K. Doorn, and E. Mazur, “Femtosecond laser-nanostructured substrates for surface-enhanced Raman scattering.,” *Langmuir : the ACS journal of surfaces and colloids*, vol. 25, no. 3, pp. 1790–4, Feb. 2009.

[106] N. W. Bigelow, A. Vaschillo, V. Iberi, J. P. Camden, and D. J. Masiello, “Characterization of the electron- and photon-driven plasmonic excitations of metal nanorods.,” *ACS Nano*, vol. 6, no. 8, pp. 7497–504, Aug. 2012.

[107] D. Wang, W. Zhu, Y. Chu, and K. B. Crozier, “High Directivity Optical Antenna Substrates for Surface Enhanced Raman Scattering.,” *Advanced Materials*, vol. 24, no. 32, pp. 4376–80, Jul. 2012.

[108] M. G. Banaee and K. B. Crozier, “Gold nanorings as substrates for surface-enhanced Raman scattering.,” *Opt. Lett.*, vol. 35, no. 5, pp. 760–2, Mar. 2010.

[109] Y. Chu, W. Zhu, D. Wang, and K. B. Crozier, “Beamed Raman: directional excitation and emission enhancement in a plasmonic crystal double resonance SERS substrate.,” *Optics express*, vol. 19, no. 21, pp. 20054–68, Oct. 2011.

[110] H. Cai and A. W. Poon, “Optical manipulation of microparticles using whispering-gallery modes in a silicon nitride microdisk resonator.,” *Opt. Lett.*, vol. 36, no. 21, pp. 4257–4259, Nov. 2011.

[111] C. a. Mejia, N. Huang, and M. L. Povinelli, “Optical trapping of metal-dielectric nanoparticle clusters near photonic crystal microcavities,” *Opt. Lett.*, vol. 37, no. 17, p. 3690, Aug. 2012.

[112] F. Svedberg, Z. Li, H. Xu, and M. Käll, “Creating hot nanoparticle pairs for surface-enhanced Raman spectroscopy through optical manipulation.,” *Nano Lett.*, vol. 6, no. 12, pp. 2639–41, Dec. 2006.

[113] L. Tong, M. Righini, M. U. Gonzalez, R. Quidant, and M. Käll, “Optical aggregation of metal nanoparticles in a microfluidic channel for surface-enhanced Raman scattering analysis.,” *Lab Chip*, vol. 9, no. 2, pp. 193–5, Jan. 2009.

[114] H. Hwang, D. Han, Y.-J. Oh, Y.-K. Cho, K.-H. Jeong, and J.-K. Park, “In situ dynamic measurements of the enhanced SERS signal using an optoelectrofluidic SERS platform.,” *Lab Chip*, vol. 11, no. 15, pp. 2518–25, Aug. 2011.

[115] J. B. Jackson and N. J. Halas, “Surface-enhanced Raman scattering on tunable plasmonic nanoparticle substrates.,” *Proc. Natl. Acad. Sci. U. S. A.*, vol. 101, no. 52, pp. 17930–5, Dec. 2004.

[116] Y. Chu, M. G. Banaee, and K. B. Crozier, “Double-resonance plasmon substrates for surface-enhanced Raman scattering with enhancement at excitation and stokes frequencies.,” *ACS nano*, vol. 4, no. 5, pp. 2804–10, May 2010.

[117] E. C. Le Ru, E. Blackie, M. Meyer, and P. G. G. Etchegoin, “Surface Enhanced Raman Scattering Enhancement Factors: A Comprehensive Study,” *Journal of Physical Chemistry C*, vol. 111, no. 37, pp. 13794–13803, Sep. 2007.

[118] C. S. Levin, S. W. Bishnoi, N. K. Grady, and N. J. Halas, “Determining the conformation of thiolated poly(ethylene glycol) on Au nanoshells by surface-enhanced Raman scattering spectroscopic assay.,” *Analytical chemistry*, vol. 78, no. 10, pp. 3277–81, May 2006.

[119] W. Zhu, M. G. Banaee, D. Wang, Y. Chu, and K. B. Crozier, “Lithographically fabricated optical antennas with sub-10nm gaps and application in surface-enhanced Raman scattering,” *Small*, vol. 7, no. 13, pp. 1761–6, Jul. 2011.

[120] S. Ciou, Y. Cao, H.-C. Huang, D. Su, and C. Huang, “SERS Enhancement Factors Studies of Silver Nanoprism and Spherical Nanoparticle Colloids in The Presence of Bromide Ions,” *The Journal of Physical Chemistry C*, vol. 113, no. 22, pp. 9520–9525, Jun. 2009.

[121] T. Barwicz, M. R. Watts, M. a. Popović, P. T. Rakich, L. Socci, F. X. Kärtner, E. P. Ippen, and H. I. Smith, “Polarization-transparent microphotonic devices in the strong confinement limit,” *Nature Photon.*, vol. 1, no. 1, pp. 57–60, Jan. 2007.

[122] M. R. Watts, H. a Haus, and E. P. Ippen, “Integrated mode-evolution-based polarization splitter.,” *Opt. Lett.*, vol. 30, no. 9, pp. 967–9, May 2005.

[123] J. J. G. M. Van der Tol, J. W. Pedersen, E. G. Metaal, J. J.-W. Van Gaalen, Y. S. Oei, and F. H. Groen, “A short polarization splitter without metal overlays on InGaAsP-InP,” *IEEE Photonic. Tech. L.*, vol. 9, no. 2, pp. 209–211, Feb. 1997.

[124] I. Kiyat, A. Aydinli, and N. Dagli, “A compact silicon-on-insulator polarization splitter,” *IEEE Photonic. Tech. L.*, vol. 17, no. 1, pp. 100–102, Jan. 2005.

[125] H. Fukuda, K. Yamada, T. Tsuchizawa, T. Watanabe, H. Shinojima, and S. Itabashi, “Ultrasmall polarization splitter based on silicon wire waveguides,” *Opt. Express*, vol. 14, no. 25, p. 12401, 2006.

[126] S. Yang, M. Cooper, and P. Bandaru, “Giant birefringence in multi-slotted silicon nanophotonic waveguides,” *Opt. Express*, vol. 16, no. 11, pp. 463–466, 2008.

[127] T. Fujisawa and M. Koshiba, “Polarization-independent optical directional coupler based on slot waveguides,” *Opt. Lett.*, vol. 31, no. 1, p. 56, 2006.

[128] Y. Yue, L. Zhang, J.-Y. Yang, R. G. Beausoleil, and A. E. Willner, “Silicon-on-insulator polarization splitter using two horizontally slotted waveguides.,” *Opt. Lett.*, vol. 35, no. 9, pp. 1364–6, May 2010.

[129] N.-N. Feng, R. Sun, L. C. Kimerling, and J. Michel, “Lossless strip-to-slot waveguide transformer,” *Opt. Lett.*, vol. 32, no. 10, p. 1250, 2007.

[130] S. McNab, N. Moll, and Y. Vlasov, “Ultra-low loss photonic integrated circuit with membrane-type photonic crystal waveguides.,” *Opt. Express*, vol. 11, no. 22, pp. 2927–39, Nov. 2003.

[131] V. R. Dantham, S. Holler, V. Kolchenko, Z. Wan, and S. Arnold, “Taking whispering gallery-mode single virus detection and sizing to the limit,” *Appl. Phys. Lett.*, vol. 101, no. 4, p. 043704, 2012.

[132] J. N. Anker, W. P. Hall, O. Lyandres, N. C. Shah, J. Zhao, and R. P. Van Duyne, “Biosensing with plasmonic nanosensors.,” *Nature materials*, vol. 7, no. 6, pp. 442–53, Jun. 2008.

[133] D. Wang, W. Zhu, Y. Chu, and K. B. Crozier, “High Directivity Optical Antenna Substrates for Surface Enhanced Raman Scattering.,” *Advanced Materials*, pp. 4376–4380, Jul. 2012.

[134] M. Barth, S. Schietinger, S. Fischer, J. Becker, N. Nüsse, T. Aichele, B. Löchel, C. Sönnichsen, and O. Benson, “Nanoassembled plasmonic-photonic hybrid cavity for tailored light-matter coupling.,” *Nano Lett.*, vol. 10, no. 3, pp. 891–5, Mar. 2010.

[135] F. De Angelis, M. Patrini, G. Das, I. Maksymov, M. Galli, L. Businaro, L. C. Andreani, and E. Di Fabrizio, “A hybrid plasmonic-photonic nanodevice for label-free detection of a few molecules.,” *Nano Lett.*, vol. 8, no. 8, pp. 2321–7, Aug. 2008.